Universita' degli Studi di Napoli Federico II, Italy
Dipartimento di Fisica "Ettore Pancini"
Research Doctorate (PhD) in Fundamental and Applied Physics
XXVIII Cycle

Transport Properties of 2DEGs at Oxide Interfaces under the Effect of Light and Electric Field

Advisors:
Prof. Umberto Scotti di Uccio
Dr. Emiliano Di Gennaro
PhD Coordinator:
Prof. Raffaele Velotta

PhD Candidate:
Mian Akif Safeen

Academic Year 2015/16

Acknowledgements

Foremost, I would like to thank my advisor Prof. Umberto Scotti di Uccio for providing me the opportunity to work with him as a PhD student. He has been actively interested in my work and has always been available to advise me. His guidance helped me in all the time of research and writing of this thesis. I am very grateful for his patience, motivation and enthusiasm. I am very thankful to Fabio Miletto Granozio, a CNR scientist, for his scientific advice, many insightful discussions and suggestions. His guidance and support helped me in completing my dissertation successfully. I am also very grateful to Emiliano Di Gennaro for all kind of help; for samples fabrication, training on transport measurement and for suggestions to improve the manuscript. I am thankful to Alessia Sambri for promptly providing me the samples and to Musa Mutlu Can and Amit Khare for assisting in some experiments. I am indebted to Ubaldo Coscia for cooperation in photoconductivity measurements and to Nadhira Laidani for providing me the opportunity to perform Hall measurements at FBK lab in Trento.

I am greatly indebted to Prof. Raffaele Velotta, the coordinator of the PhD program, for his support, care and for regularly monitoring my activity during these three years. I gratefully acknowledge the graduate school for funding my PhD study. I also praise the PhD school and MP COST action for supporting my scientific missions to Rome, Trento (Italy), Cargèse (France), Warsaw (Poland) and Boston (USA).

I am grateful to departmental staff for always being supportive both in research and official matters. Very special thanks to Guido Celentano, the secretary of the PhD program, for helping me and always being AVAIBLE in any fight against administrative problems. Especially, I am thankful to Stefano Marrazzo in mechanical work for helping in building up of photoconductivity setup.

Let me thank my friends Ihsan Afridi, Tahmina, Asad, Alan Ruggeri, Atanu Nath and Nivya Roy. They always remain a source of inspiration and strength for me. They supported me in writing, and encouraged me to strive towards my goal.

Most importantly, I wish to thank my Abbu and Ammi, they raised me, supported me, taught to me, and loved me. I am extremely grateful for their prayers, caring and sacrifices for educating and preparing me for my future. They always motivated me to work harder. They are the very prime institution in my life. ***To them I dedicate this thesis.***

I am greatly indebted to the efforts and prayers of my brothers Manzoor Ahamd, Kashif Safeen, Wasif Safeen and Anis Safeen who all constantly remained in touch with me during the entire period. Especially thanks to Kashif, who at the same time was preparing for his PhD defense, but also helped me a lot in formatting the thesis. I am deeply obliged to my sister for her love and support throughout my studies. Last but not least, I highly rank the prayers, support and encouragement of my uncles.

"Peace Begins with a Smile" Mother Teresa,
Keep Smiling and Stay Happy

Mian Akif SAFEEN
Naples, Italy
March 30, 2016

List of abbreviations

2DEG	Two-Dimensional Electron Gas
FPP	First Positive Polarization
MODA	Modular facility for the Oxides Deposition and Analysis
LIGS	Localized In-Gap States
RRR	Residual Resistive Ratio ($R_{290\ K}$ /$R_{10\ K}$)

List of Symbols

R_{sheet}	Sheet Resistance
n_o	Intrinsic sheet carrier density
Δn	Variation in sheet carrier density (by light or by electric field)
n	$n_o + \Delta n$ (total sheet carrier density)
ε_r	Relative permittivity/Dielectric constant
μ	Electron Mobility
σ	Sheet conductivity
$\Delta\sigma$	Change in sheet conductivity
V_G	Gate voltage
e	Charge of electron
Φ	Photons flux (measured in $s^{-1}\ cm^{-2}$)

Table of Contents

Introduction and Outline

Two-dimensional electron systems are the essential element of today's semiconductor technologies. The physical laws of ordinary matter are prone to be radically modified by reducing the dimensionality, and completely new phenomena can manifest themselves. Many Nobel Prizes have been awarded for research related to 2D systems in solids, starting from the prize in 1985 to von Klitzing for the discovery of Quantum Hall Effect, to the 2010 prize to Geim and Novoselov for the breakthrough of graphene. In between, Kroemer and Alferov won the Nobel Prize in Physics for the invention of semiconductor heterostructures, which revolutionized semiconductor technology and make up the basis of many modern electronic devices.

Conventional electronics is based on silicon and on several III-V groups elements. In the last decades, another class of materials came into the spotlight of physicists, and remains nowadays in the main stream of the research in the field of material science for electronics: the transition metal (TM) oxides. TM oxides lie within the group of "correlated materials". The research on these oxides is boosted in the last 25 years by a number of successive discoveries, including high temperature superconductivity, colossal magnetoresistance, record-high dielectric/ferroelectric/piezoelectric performances, resistive switching behavior, giant thermoelectric effect etc. Such discoveries have attracted a large number of scientists from different disciplines to this field.

In recent years, a vast realm of unexplored and ill-understood phenomena taking place at the interface between different oxides has been disclosed to solid-state scientists. Interfaces are under many aspects artificial systems that can be engineered in order to combine, in a single device, the functionalities of their individual layers, or even to exploit a wide range of emergent novel properties that can be surprisingly different from those of the single building blocks. Most striking examples include the formation of a high-mobility two-dimensional electron gas (2DEG) at the interface between two band insulator oxides ($LaAlO_3$ and $SrTiO_3$) [1]. This interface exhibits unanticipated properties such as high electron mobility, interface magnetism and

superconductivity. Soon after the discovery of 2DEG at the $LaAlO_3/SrTiO_3$ interface, it was demonstrated that many other oxide heterostructures such as $LaGaO_3/SrTiO_3$, $NdGaO_3/SrTiO_3$ and γ-$Al_2O_3/SrTiO_3$ exhibit similar properties. An increasing number of experiments have shown that 2DEGs in oxides are extremely sensitive to two kinds of perturbation: light and electric field. In both cases the response is non-trivial. The interfaces show giant photoconductivity that is persistent in nature [2]. Furthermore, the electric field effect in the three terminal devices based on $LaAlO_3/SrTiO_3$ also shows anomalous behavior [3], which goes beyond the simple capacitor charge/discharge model that approximately explains the operation of field effect transistors based on silicon.

Basically, the 2DEG at oxide interfaces is confined in a quantum well. Shining light or applying a gate voltage enables to control the filling of the well and thus to modulate the 2DEG electronic properties. By this tool it is possible to determine a metal to insulator transition [4], or to span the phase diagram by changing the density of electric carriers. This exciting feature opens new avenues for studying the electronic orders as well as for developing a next generation of oxide-based electronics.

The present thesis investigates the electrical transport of $LaAlO_3/SrTiO_3$ heterostructures and of the related systems such as $LaGaO_3/SrTiO_3$, $NdGaO_3/SrTiO_3$ and γ-$Al_2O_3/SrTiO_3$ under the combined effect of light and electric field. To this aim, the first part of the work was devoted to the study of the photoresponse of amorphous and crystalline oxides interfaces under irradiation of variable-wavelengths and intensities, with the aim of clarifying some details of the electronic structure and of the distribution of defects. Comparing amorphous and crystalline structure is interesting, because the crucial difference between the two systems consists in the amount of oxygen vacancies that, acting as point defects, may play a key role in the photoresponse. In a second moment the study was focused on the transport properties of three terminal devices fabricated by adding a back-gate to the $LaAlO_3/SrTiO_3$ interface. Finally, the interplay between the action of light and gate voltage was considered.

Experimental findings include the observation and modeling of several effects, with particular reference to persistent effects and to hysteretical behaviors. The experimental results provide some insight in the fundamental properties of the oxide interfaces that host a 2DEG, and in particular in the nature and role of defects in the optoelectronic response. Furthermore, they

allow to envisage the application of oxide interfaces as non-volatile memories with electro-optical control.

The experiment result described in this thesis was carried out at the laboratories of Department of Physics and CNR-SPIN, University of Naples "Federico II" Naples, Italy.

This manuscript is organized as follow. The first part (Chapter 1) provides an overview of the state-of-the-art of perovskite oxide heterostructures physics. The second part (Chapter 2-5), covers the experimental work carried out during my PhD work. Chapter 2 deals with the photoconductivity of oxide heterostructures. Chapter 3 discusses the transport properties of oxide heterointerfaces under the modulation of a gate voltage and under the combined effect of light and electric field. Chapter 4 reports the non-trivial behavior of the interfaces under the effect of electric field at low temperature. Furthermore, the operation of interfaces as bi-stable system is presented. Chapter 5 examines the origin and nature of the defects state, and evaluates their effect on electron mobility. Finally, a summary and the conclusion are presented.

Chapter 1

Introduction to the Physics of Oxide Interfaces

1.1 Semiconductor Heterostructures

In the last decades semiconductor heterostructures have become a cornerstone in fundamental and applicative researches on condensed matter. The advancement in semiconductor processing revolutionized the low-dimensional semiconductor systems resulting in sophisticated devices. The interfacial phenomena exploited by these devices enable data processing, memory, and electronic communications. Most of them rely on the technology of heterostructures.

Heterostructures are thin film structures that are made by at least two or more materials. The motion of electrons and holes in the heterostructures can be controlled and modified by the variation in composition of the constituent materials. Electrons and holes may also be constrained by engineering the coupling of materials with specific alignments of the conduction and valence bands.

By this tool it is also possible to limit the motion of the charge carriers in two or less dimension. Electrons that are confined in a thin slab form a two-dimensional electron gas (2DEG) [5, 6].
To realize a 2DEG system in an experimental device, two conditions need to be met:

- There has to be a quantum well
- There have to be charge carriers (electrons and holes) within the quantum well

Quantum well is the most elementary segment of many heterostructures based devices. Most popular example can be embedding a layer of GaAs in AlGaAs sandwich, where the quantum well is built by the energy band bending as show in Figure 1.1. If the quantum well is thin

enough, discrete energy levels (subbands) can be observed for electron occupancy in the well. The free carriers can be brought into the quantum well by standard semiconductor doping. In case of *n-type* doping, 'excess' electrons are added to the conduction band and freely move throughout the quantum well. The donor atoms, however, also form scattering centers which limit the electron mobility, and for practical application this must be avoided. The GaAs-AlGaAs system were born to overcome this problem by the so-called *modulation doping*, where the carriers introduced by the dopants and the ionized impurities are spatially separated. Principally, this is achieved by coupling a doped donor layer to an undoped channel layer, with a band structure engineered in such a way to induce charge transfer through the interface and creating a space charge region. Hence by the *modulation doping* of the engineered heterostructures, carriers are spatially separated from the ionized impurities and their mobility is greatly enhanced. Both the confinement and the electron density can be tuned in such a way that free carriers mostly occupy one energy level of the quantum well. In this case a quasi-2DEG is obtained [7].

2DEG provided opportunities for research, such as integer and fractional quantum Hall effect [8], and also led to the development of new applications such as quantum cascade laser [9], optical devices and the high electron mobility transistor that used in cell phones and satellite electronics.

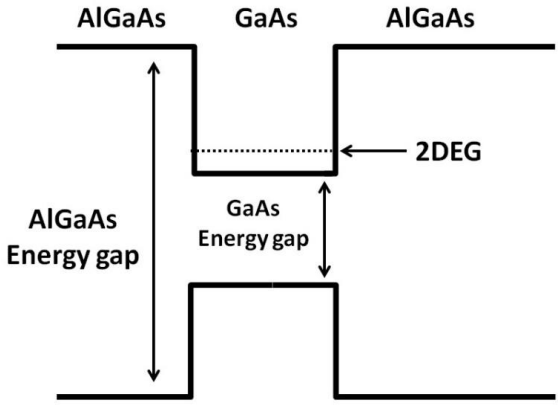

Figure 1.1 Schematic diagram of a GaAs/AlGaAs quantum well

1.2 Strongly Correlated Materials

Many of the materials that shape today's technologies have properties that are comparatively insensitive to the repulsive interactions between electrons. The electrical, mechanical, and thermal properties of silicon, aluminum, diamond, may all be reasonably understood well by dealing electrons as non-interacting entities. The electronic states in these materials are primarily built from *s* and *p* orbitals. Because of the Pauli Exclusion Principle and the delocalized character of their electronic states, the kinetic energy of the electrons dominates over the electron-electron interaction [10]. It means that the electrons behave as a Landau liquid, i.e. behave as a gas of fermions in a periodic potential.

On the other hand, there are materials in which electron-electron interactions play a central role in determining the electronic, magnetic and optical properties. These are the materials with open *d* and *f* electron shells, where electrons occupy narrow orbitals, with properties that are harder to explain in terms of simple band picture. In transition metals, such as vanadium, iron, titanium and their oxides, for example, electrons experience strong Columbic repulsion because of their spatial confinement in those orbitals. Such strongly 'correlated' electrons cannot be described by single band models. Instead, a quite complex quantum mechanical treatment is needed [11].

In general, the complex interplay between electron-electron interactions, lattice structure, kinetic energy and magnetic degrees of freedom results in a very rich phase diagram of the material. These phase can have surprising and useful properties, such as high temperature superconductivity, ferromagnetism etc. Likewise, the transitions between such phases can have technologically relevant features, such as orders-of-magnitude changes in electrical conductivity (metal-insulator transitions), also tuned by magnetic field (colossal magnetoresistance). Owing to these rich behaviors, strong correlations can act as a tool, through which small changes in controllable parameters, such as temperature, pressure, or doping, can have dramatic consequences on material properties [10].

1.3 Transition Metal Oxides

MOSFETs (Metal-Oxide-Semiconductor Field-Effect Transistors) have been for a long time the key elements of modern electronics industry. But nowadays, due to the intrinsic restrictions, the further scaling of MOSFET devices either encounters fundamental limits or demands for

increasingly sophisticated and expensive engineering solutions. Alternative approaches and device concepts are being currently designed both for purpose of a permanent integration enhancement, and to improve the functionality and performance of electronic devices. Electronics based on transition metal oxides (TMOs) is one such promising approach which could enable and accelerate the development of information and computing technology [12].

TMOs are an exciting class of materials owning diverse range of physical properties such as electrical, magnetic, structural or optical. The reason for these properties is that the oxides contain transition metals cations which have a large number of electron states provided by the open *d* shell. Therefore, it provides a large number of possible valence states, i.e. (most) TMOs have more than one oxidation state. Many of the properties of TMOs strongly depend on materials defects like vacancies and dislocations. Specifically, the electronic properties are characterized by the nature of the oxygen-cation bonding, which usually involves multiple orbitals, resulting in interplay between localized and migrant character for the electrons. The defects affect local oxygen bonding and thereby the properties [13].

More conclusively, the rich behavior of transition metal oxides arises from the complex interactions between their charges, orbital, spin, and lattice degrees of freedom. These interactions can be modified at interfaces between different oxides through the effects of local symmetry breaking, charge transfer, electrostatic coupling, strain, and frustration, leading to fascinating new phenomena [14] as shown in Figure 1.2. Due to these functionalities oxides exhibit the full spectrum of electronic, optical, and magnetic behavior: insulating, semiconducting, metallic, superconducting, ferro/piezoelectric, ferromagnetic, and multiferroic effects are all possessed by structurally compatible oxides.

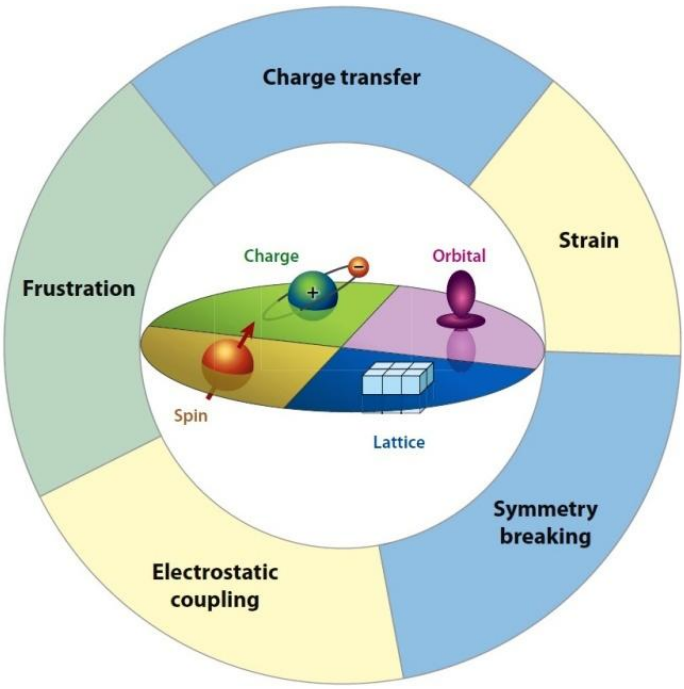

Figure 1.2 Spectacular properties of many oxides arise from the complex interactions between their charge, orbital, spin, and lattice degrees of freedom, (re-printed with permission from [14]).

Some specific examples of electronic properties are mentioned here. Al_2O_3 and $SrTiO_3$ are closed shell compounds with strong ionic character of the bonds and therefore they are insulators with large band gaps. In the TMOs having closed outermost shell but with relatively high electro-negativity, the more covalent nature of bonding yields semiconductors with relatively high carrier mobilities. ZnO and SnO_2 represent the example of semiconductors oxides. Oxides containing metal cations with a tendency to form mixed valence compounds can yield Mott insulators ($LaMnO_3$), metals like $SrRuO_3$, or high-temperature superconductors $YBa_2Cu_3O_7$.

The matchless variety of physical properties of oxides holds remarkable promise for electronic applications. Some of these applications are already commercially grown-up, like transparent electronics for flat panel displays (using $(In,Sn)O_3$ or ZnO) or in a very advanced research stage, like ZnO laser optics or bolometers for gas sensors application using manganese oxides. Analogous to today's semiconductor device structures, many device concepts utilizing oxides will likely use alternately layered structures where dimensions are minute enough to observe

quantum size effects (nanometer scale thicknesses). With advancement in the fabrication techniques it is now possible to epitaxially grow oxides thin films with atomic level precision and structural control similar to what is achieved in today's most advanced semiconductor structures [15].

The discovery of 2DEGs at well-defined interfaces between complex oxides provides an opportunity for a new generation of oxide electronics. Particularly, the 2DEG at the interface between two perovskite insulators, represented by the formula ABO_3, has attracted significant attention. The high-mobility 2DEGs at complex oxide interfaces are expected to provide a wealth of opportunities to study condensed matter physics with strongly correlated electrons confined in nanostructures. Moreover, they also show promise for oxide devices with functionalities much richer than those found in the conventional semiconductor devices.

This thesis deals with the transport properties of interfacial conductivity that arises between the thin films of $LaAlO_3$, $LaGaO_3$, $NdGaO_3$, spinel/perovskite γ-Al_2O_3 and $SrTiO_3$ substrate.

1.4 Strontium Titanate

1.4.1 Introduction

Strontium titanate ($SrTiO_3$) belongs to the class of perovskite oxides of significant importance for a variety of scientific and technological applications. One reason for this interest is the wide use of $SrTiO_3$ as a standard substrate for oxides thin film deposition. It includes the growth of high-T_c superconductors [16], colossal magnetoresistance oxides or ferroelectrics due to the similarities in crystal structure and good lattice constant matching. Moreover, $SrTiO_3$ is chemically inert and in many cases it does not react with the deposited materials. The scope of $SrTiO_3$ has been further enhanced by the capability to chemically process its (001) surface to obtain a 100 % TiO_2 termination $SrTiO_3$. This is done by the chemical etching in NH_4F–HF buffer solution in combination with thermal treatment [17, 18]

1.4.2 Crystal Structure

At room temperature, $SrTiO_3$ has the simplest and highest symmetry in form of ABO_3 perovskite cubic structure with lattice parameter of 3.905 Å and Pm3m as crystallographic space group. The crystal structure of $SrTiO_3$ is sketched in Figure 1.3 (a). The Ti^{4+} ions are six fold coordinated by

O^{2-} ions, while each of the Sr^{2+} ions is surrounded by four TiO_6 octahedra with perfect 90° angles. Around 105 K, neighboring TiO_6 octahedra are slightly rotated in opposite directions and $SrTiO_3$ undergoes a structural transition from cubic to tetragonal (space group I4/mcm) [19] at lower temperatures as depicted in Figure 1.3 (b).

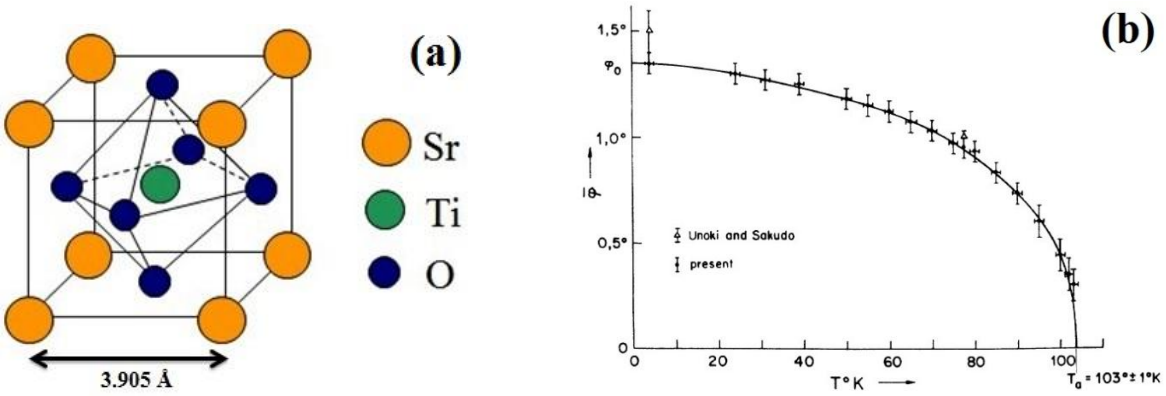

Figure 1.3 (a) Atomic structure of $SrTiO_3$ at room temperature (b) Tetragonal rotation angle in $SrTiO_3$ as a function of temperature indicating a structural transition around 105 K, Figure adopted from [19]

1.4.3 Electronic Structure

As discussed in the last section, $SrTiO_3$ in its chemical form consists of A-site cations, Sr^{2+}, B-site cation, Ti^{4+}, and oxygen anions (O^{2-}). In a Ti^{4+} cation the energies of the *d* orbitals are affected by an octahedral arrangement of six oxygen anions. An isolated ion has no energy splitting and therefore the *d* orbitals are initially degenerate. If we distribute oxygen anions uniformly over the surface of a sphere, the *d* orbitals remain degenerate, but their energy will be higher due to columbic repulsion between the spherical shell of negative charge and the electrons in the *d* orbitals. Instead, the oxygen anions at the vertices of an octahedron will lift the degeneracy: the *d* orbitals split into two groups, namely t_{2g} and e_g, separated by an energy difference Δ_o, known as crystal field splitting, as shown in Figure 1.4 (a). The energies of the orbitals depend on their orientations. The orbitals $3d_{x^2-y^2}$ and $3d_{z^2}$ that point directly toward the

six O^{2-} ions (Figure 1.4 (b-c) have higher energy. The other three orbitals ($3d_{xy}$, $3d_{xz}$, and $3d_{yz}$) laying between the O^{2-} ions (Figure 1.4 (d-f) have lower energy [20].

In a perfectly symmetric Ti^{4+} system like cubic $SrTiO_3$ both the 3 different t_{2g} states and the 2 different e_g states are degenerate. However, a deviation from the cubic symmetry, for example, by a tetragonal distortion, causes an energy splitting of the t_{2g} and e_g states due to the interface symmetry breaking as depicted in Figure 1.4 (a) [21].

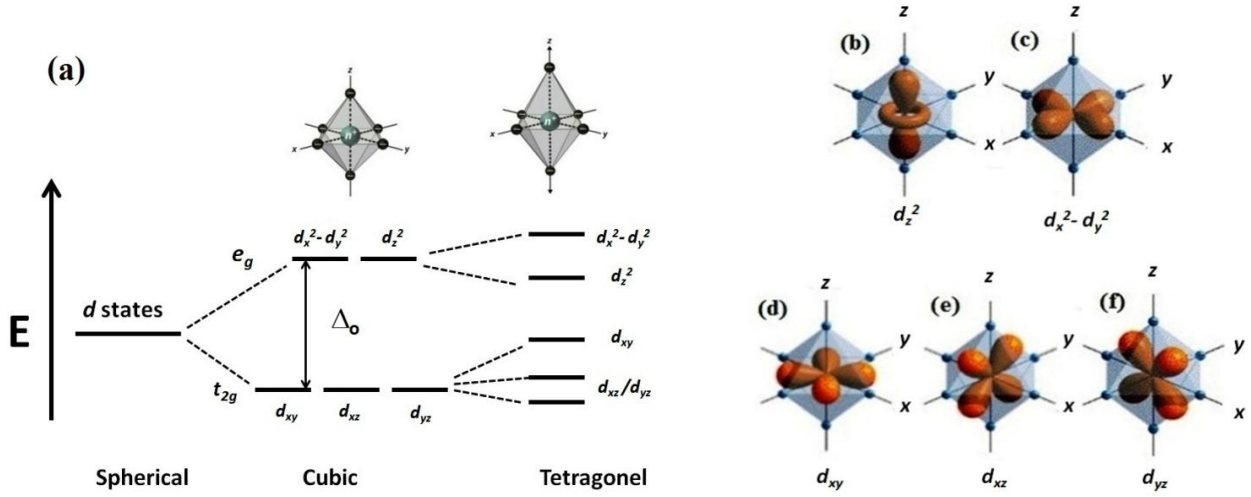

Figure 1.4 (a) Crystal field splitting in the oxygen octahedral of $SrTiO_3$ (b-f) Graphical representation of different orientation of 3d orbitals.

In terms of band diagram, $SrTiO_3$ is constituted by completely filled O *2p* and empty Ti *3d* band, hence under the fundamental band gap concept yielding a band insulator. The density of states (DOS) profile in of Figure 1.5 (b) shows the shape of valance and conduction bands with Fermi level below the conduction band. Ti *3d*-states might have some character overlap in valance band. The band structure of $SrTiO_3$ shows that the *3d* band has two degenerated minima at Γ and X, while the *2p* valence band has three maxima at *R*, *M* and Γ (Figure 1.5 a), yielding an indirect band gap which has been experimentally reported to be 3.2-3.3 eV and a direct band gap about 3.6-3.8 eV [22, 23].

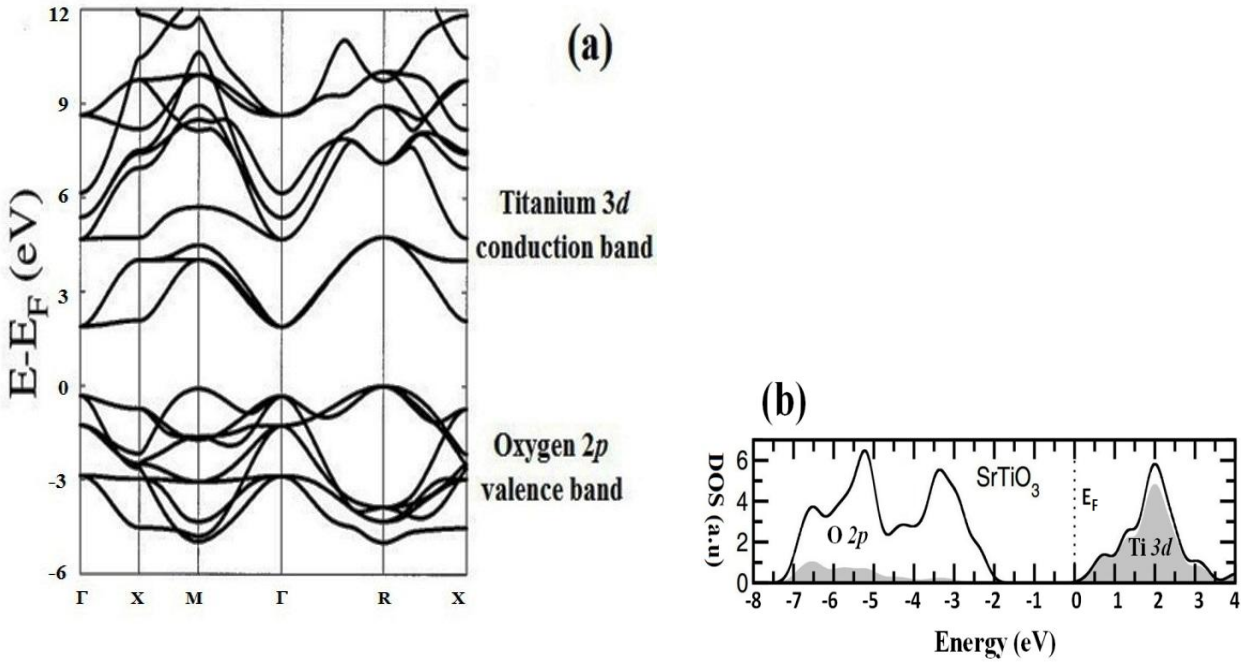

Figure 1.5 (a) representation of band structure calculated *ab initio* in the local density approximation, direct and indirect gaps respectively corresponds to $\Gamma \rightarrow \Gamma$ and $R \rightarrow \Gamma$ (re-printed with permission from [23]) (b) DOS profile of valance and conduction band of $SrTiO_3$, shaded areas represent the projected DOS for Ti *3d*-states (re-printed with permission [24]). Note that the absolute value of the gap is hardly captured by this computational technique.

1.4.4 Dielectric Properties

The dielectric properties of $SrTiO_3$ are qualitatively similar to those of the paraelectric phase of typical perovskite ferroelectrics like $BaTiO_3$. In these materials there is a soft transverse optical mode whose frequency approaches zero when the material is cooled [25, 26]. This mechanism leads to an increase in the dielectric constant of $SrTiO_3$ with decreasing temperature [27] (see Figure 1.6 a). Along with temperature, the dielectric constant (ε_r) of $SrTiO_3$ also strongly depends on electric field. This dependence has been numerically represented by the following mathematical expression [28]

$$\varepsilon_r(E,T) = \frac{b(T)}{\sqrt{a(T) - E^2}}$$

Here, *a(T)* and *b(T)* are temperature-dependent parameters. The simulated $\varepsilon_r(E)$ based on above equation is shown in Figure 1.6 (b).

The temperature dependence of the dielectric constant obeys the Curie-Weiss law with a Curie temperature near 40 K [29]. However, $SrTiO_3$ does not undergo a ferroelectric transition, because quantum fluctuations in $SrTiO_3$ at low temperature suppress the ferroelectric transition. Therefore $SrTiO_3$ is sometimes called a quantum paraelectric [27]. However this state is very sensitive to perturbations of the lattice [30]. In fact, while in its pure and unstressed form $SrTiO_3$ is an incipient ferroelectric [27], a ferroelectric transition can take place under the effect of strain [31]. The Ferroelectric transition can also be induced in $SrTiO_3$ by doping it with other cations such as Ca or Bi [30]. Furthermore, Fuchs *et.al.* showed ferroelectricity below 90 K in an epitaxially grown $SrTiO_3$ thin films [32].

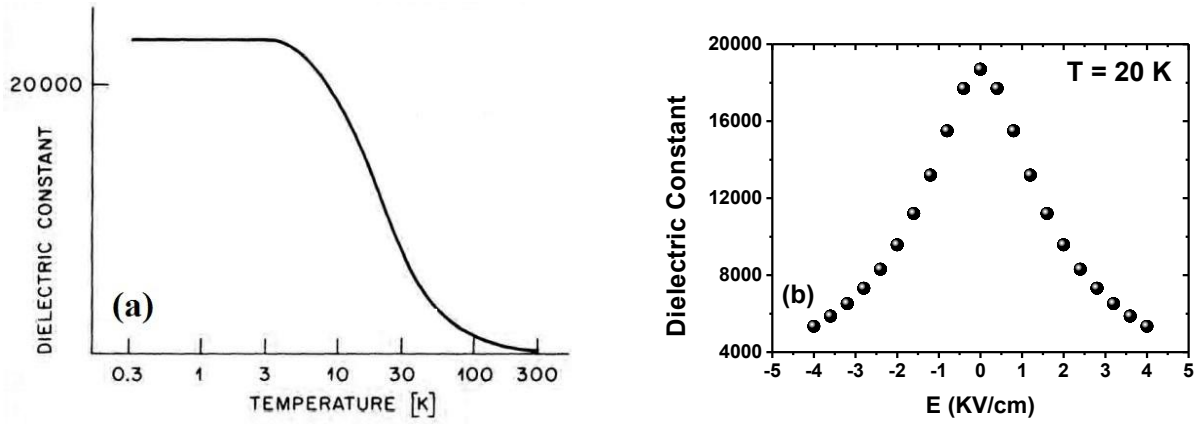

Figure 1.6 (a) Experimental dielectric constant of $SrTiO_3$ as a function of temperature (re-printed with permission from [27]); (b) simulated [28] dielectric constant of $SrTiO_3$ as a function of electric field at 20 K.

The high dielectric constant of $SrTiO_3$ (~300) at room temperature, its strong temperature and electric field dependence together with the good dielectric breakdown properties of single crystals, make it very useful as gate insulator for electric field effect experiments with perovskite thin films. The high dielectric constant of $SrTiO_3$, as gate insulator, anticipates large charging and discharging capacity. In this work $SrTiO_3$ has been utilized as gate insulator in the field effect experiments (chapter 3 and 4).

1.4.5 Defects-induced Transport Properties

In its pure form, $SrTiO_3$ is an insulator with very low leakage. However, it shows a semiconducting or metallic behavior when doped. It is even a conventional superconductor with critical temperature ~350 mK [33] if doped with carrier densities above 10^{19} cm^{-2}. Metallic conduction and superconductivity can also be induced, without chemical doping, by electric field-effect alone [34].

Both *p* and *n-type* doping is possible in $SrTiO_3$. The *p-type* doping [35] has been achieved by substituting trivalent metal ions (e.g., In^{3+}, Al^{3+}, Fe^{3+}, and Sc^{3+}) for Ti^{4+}, while on the other hand *n-type* conduction [36] has been achieved by substitution of La^{3+} for Sr^{2+} (i.e., $Sr_{1-x}La_xTiO_3$), Nb^{5+} for Ti^{4+} (i.e., $SrTi_{1-y}Nb_yO_3$), etc., or by reduction to $SrTiO_{3-\delta}$. In the latter case, each oxygen vacancy generates two doped electrons [37]. The conductivity induced by oxygen vacancies can be enhanced by annealing in vacuum, while annealing under oxygen-rich conditions leads a decrease in conductivity [38, 39]. Many studies [40] reveal that the oxygen vacancy in $SrTiO_3$ possesses a double donor nature. One electron (out of one of oxygen vacancy) is easily ionized to the conduction band, showing the shallow donor nature. The other electron is self trapped near the vacancy in the form of a small polaron; it is this electron state that gives rise to the deep-level behavior and the below-gap blue luminescence [40].

There are many studies dealing with the transport properties of doped $SrTiO_3$ [41]. As an example, Ubate and Chapman [42] showed that niobium-doped and reduced (oxygen deficient) $SrTiO_3$ samples exhibit metallic behavior down to 2 K as shown in Figure 1.7 (a,b). For all the samples, regardless of the doping type and level, the electron mobility in the temperature range 150-300 K approximately follows a power law of the form $\mu_H \propto T^{-\alpha}$ $cm^2 V^{-1}s^{-1}$, with $\alpha \sim 2.7$, in agreement with data from [41]. The mobility shows a strong dependence on the electron

concentration for T < 150 K, and it becomes nearly independent of temperature at low temperature. Qualitatively the transport properties of doped $SrTiO_3$ are similar to $LaAlO_3/SrTiO_3$ interfaces that are introduced in section 1.5.

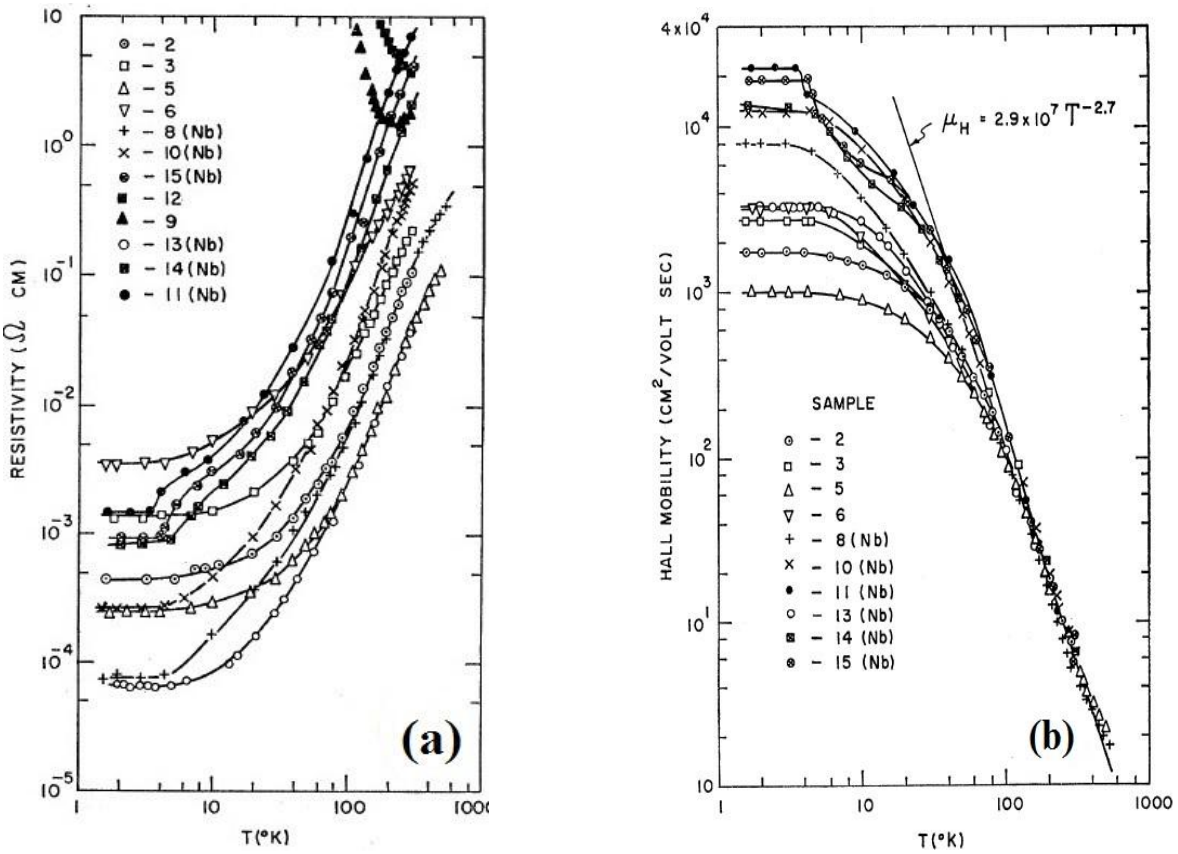

Figure 1.7 Temperature dependence of (a) resistivity (b) Hall mobility in doped $SrTiO_3$ (re-printed with permission from [42])

1.4.6 2DEG at $SrTiO_3$ Surface

Recent works demonstrated the formation of a two-dimensional electron gas (2DEG) on the surface of *in situ* cleaved $SrTiO_3$ [43]. Oxygen vacancies, created in the crystal fracturing or triggered by exposure to ultraviolet light, were indicated as the origin of the formation and confinement of the 2DEG. The work by Santander-Syro *et al.* [43] demonstrated this property by

careful angle resolved photoemission spectroscopy (ARPES) on vacuum cleaved $SrTiO_3$ single crystals. The measurements reveal that the surface states possess several subbands that cross the Fermi energy, originated from the Ti *3d* orbitals in the system. In the bulk $SrTiO_3$, the bottoms of the bands are at the same energy and therefore are degenerate (Figure 1.8 a). At the surface the degeneracy is lifted due to the strong electric field and the band splits into multiple subbands (Figure 1.8 b,c) .

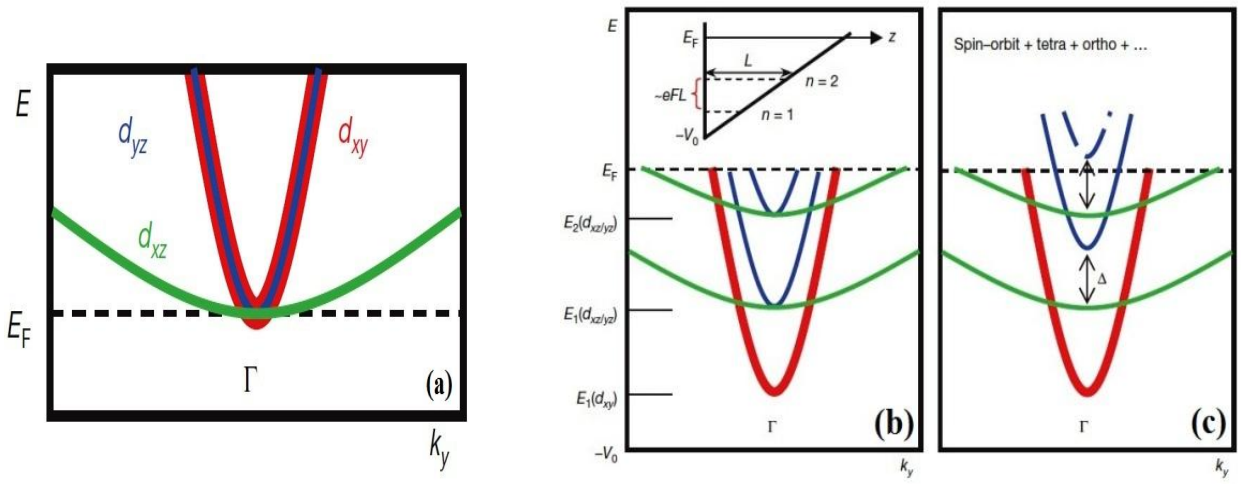

Figure 1.8 Electronic structure of $SrTiO_3$ and effects of electron confinement proposed by Santander-Syro *et al.* (a) bulk band structure of $SrTiO_3$ with degenerate Ti $3d_{xy}$, $3d_{xz}$ and $3d_{yz}$ bands (b) subbands resulting from the confinement of electrons near the surface of $SrTiO_3$. The inset shows a wedge-like potential created by an electric field of strength F at the surface (c) additional subband splitting due to spin-orbit interactions and structural distortions in the material, (re-printed with permission from [43]).

Figure 1.9 shows the density of electrons for the un-doped sample as obtained by ARPES, displayed as a function of the electron binding energy and momentum (E, k). It has been observed that even for the non-doped sample, for which no bulk bands at E_F are expected, the cleaved surface yields intense, strongly dispersive bands across the Fermi level. These data show free-electron-like parabolas ($E \sim k^2$) quantized in two levels by the 2D confinement. As the bands are occupied up to the Fermi level (E_F), the 2DEG is metallic. The 2DEG arises because a quantum well is formed at the interface between the surface $SrTiO_3$ and vacuum. The metallic

surface indicates that the quantum well is filled with electrons that are presumably coming from inner donor states that are present in the $SrTiO_3$ bulk.

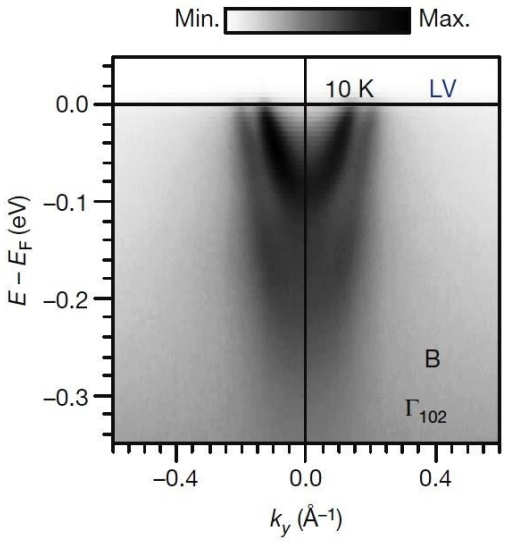

Figure 1.9 Universal electronic structure at the surface of $SrTiO_3$ studied using ARPES. Corresponding energy–momentum intensity maps close to the Γ point. The strongly dispersive bands across the Fermi level correspond to a large density of mobile carriers (re-printed with permission from [43]).

Di Capua *et al.* [44] also showed that the $SrTiO_3$ surface can exhibit 2D conductivity after a suitable annealing procedure in vacuum. In this worked the electronic properties of samples were probed by scanning tunneling microscope (STM) and scanning tunneling spectroscopy (STS) joined to x-ray photoemission spectroscopy (XPS). Signature of the 2DEG is the non-zero conductance at zero bias (Figure 1.10 a) and the presence of Ti^{3+} states at the sample surface (Figure 1.10 b).

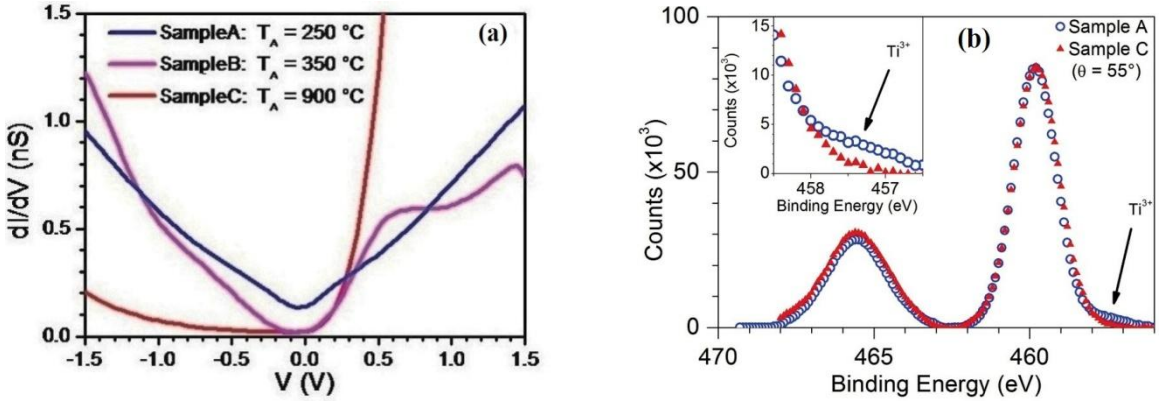

Figure 1.10 (a) differential conductance (*dI/dV*) plot on various samples obtained by STS (b) XPS spectra on different samples around the binding energy range of the Ti 2*p* doublet states (re-printed with permission from [44]).

1.5 $LaAlO_3/SrTiO_3$ and other similar Hetero-interfaces

1.5.1 Overview

$LaAlO_3$ and $SrTiO_3$ are band insulators with large band gaps of 5.6 and 3.2 eV respectively. Surprisingly, in 2004, Ohtomo and Hwang [1] discovered a conducting interface between these two insulators when $LaAlO_3$ is epitaxially grown on (001) oriented $SrTiO_3$. Typically, such samples show resistance vs. temperature plots with metallic behavior. The Hall measurements show that the electrical transport is due to electronic conductivity [1]. However, a small p-type contribution has also been observed [45]. Recently, it was demonstrated that the interfacial conductivity also arises at the $LaAlO_3/SrTiO_3$ (110) and (111) interfaces. The transport properties of these interfaces are anisotropic [46]. Finally, Chen, Y. *et al.* [47] showed conductivity in the amorphous $LaAlO_3$ grown on epitaxial $SrTiO_3$.

Recently, other materials than $LaAlO_3$ were considered as overlayers in conducting interfaces. The small lattice mismatches (< 3 %) (Table 1.1) of other perovskites such as $DyScO_3$, $LaGaO_3$ and $NdGaO_3$ with $SrTiO_3$ allow the possibility for the growth of both crystalline and amorphous

structures [48]. It is also possible to grow spinel/perovskite γ-Al_2O_3 on $SrTiO_3$ [49], in spite of the difference at crystal structures. The spinel structure is shown in Figure 1.11.

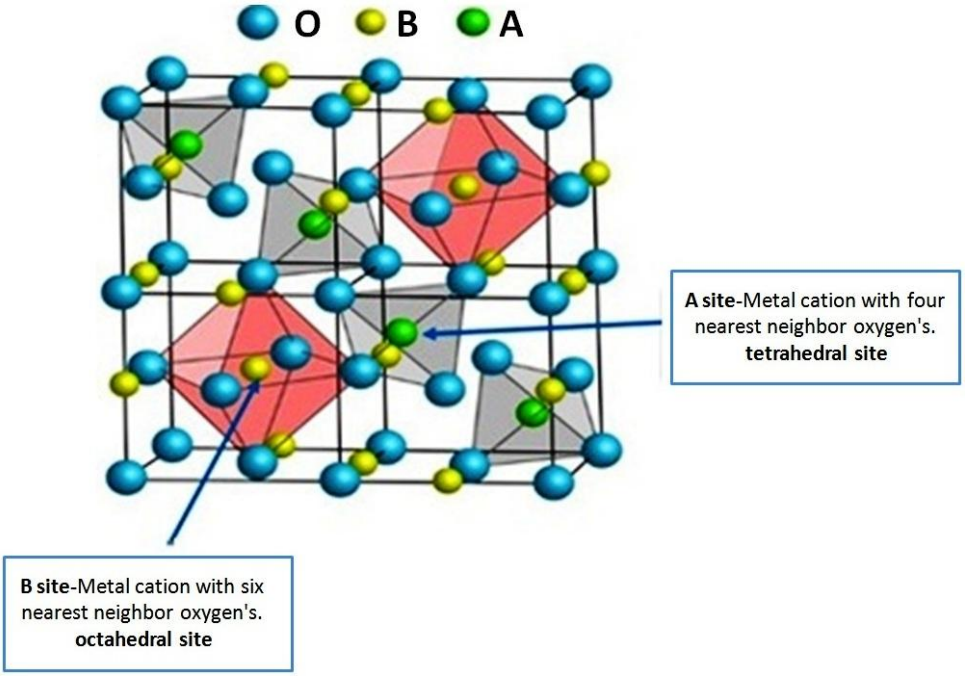

Figure 1.11 Crystallographic representation of spinel structure. The spinel structure has the generic formula AB_2O_4, where A is a cation with +2 charge and B is a cation with +3 [50]. The cubic spinel unit cell with stoichiometry AB_2O_4 is made up of 32 oxygen anions in a cubic close-packed arrangement and 24 cations, of which the 16 B cations are placed in octahedral and the 8 A cations in tetrahedral interstices. To satisfy the γ-Al_2O_3 stoichiometry, deviating from the chemical formula of a spinel, Al ions adopt the A and B cation sites of the spinel structure, the Al atomic are missing from the structure and vacancies are distributed over both the tetrahedral and octahedral sites 8 A and 16 B.

The question whether the broad range of exotic properties of $LaAlO_3/SrTiO_3$ can also be demonstrated in these similar oxide structures was properly addressed [48, 49]. It is found that several interface between oxides on $SrTiO_3$ share the same properties as $LaAlO_3/SrTiO_3$, such as, threshold critical thickness (> 3 uc) of the overlayer for conductivity [4, 48], superconductivity [51], photoconductivity [2, 48], sensitivity to oxygen environment [52].

Table 1.1: Comparison of some properties of the oxides that are used in this study [1, 48, 49]. Values are taken at room temperature.

Material	***Crystal structure***	***Lattice constant (Å)***	***Bandgap (eV)***	***Dielectric constant***
$LaAlO_3$	perovskite	3.790	5.6	25
$LaGaO_3$		3.874	4.4	27
$NdGaO_3$		3.860	3.8	20
$SrTiO_3$		3.905	3.2	300
γ-Al_2O_3	spinel	7.911	8	11

1.5.2 Basic Properties

After having introduced other interfaces in the previous section 1.5.1, here the focus is on the basic properties of $LaAlO_3/SrTiO_3$ interfaces. Conducting interfaces are obtained for the growth of $LaAlO_3$ on TiO_2-terminated $SrTiO_3$ substrates denoted as *n-type* interface, while when $LaAlO_3$ is grown on SrO-terminated $SrTiO_3$ substrates the interface show insulating behavior (*p-type*) [1, 53]. Figure 1.12 (a,b) shows the two possible configurations of the $LaAlO_3/SrTiO_3$ heterostructures with respect to surface termination of $SrTiO_3$ and Figure 1.12 (c) shows the corresponding dramatic difference in the transport properties. The $LaAlO_3/SrTiO_3$ interface shows an immediate transition from insulating to metallic behavior when the $LaAlO_3$ layer thickness exceeds a critical value of three unit cells [4, 48]. Abrupt electronic rearrangements at the $LaAlO_3/SrTiO_3$ interface with increasing $LaAlO_3$ layer thickness have been observed also by second harmonic generation spectroscopy [54]. The $LaAlO_3/SrTiO_3$ interface triggered further scientific interest by the observation of a transition into a superconducting state below 200 mK

[51] and a proposed ferromagnetic ordering [55]. The spectroscopic signature of Ti^{3+} by various X-ray spectroscopy methods [56] and by high resolution electron microscopy/spectroscopy [57] in the vicinity of the $LaAlO_3/SrTiO_3$ interface confirms the n-type character of the conduction. The conducting sheet is considered to be located in the $SrTiO_3$ matrix close to the $LaAlO_3/SrTiO_3$ interface.

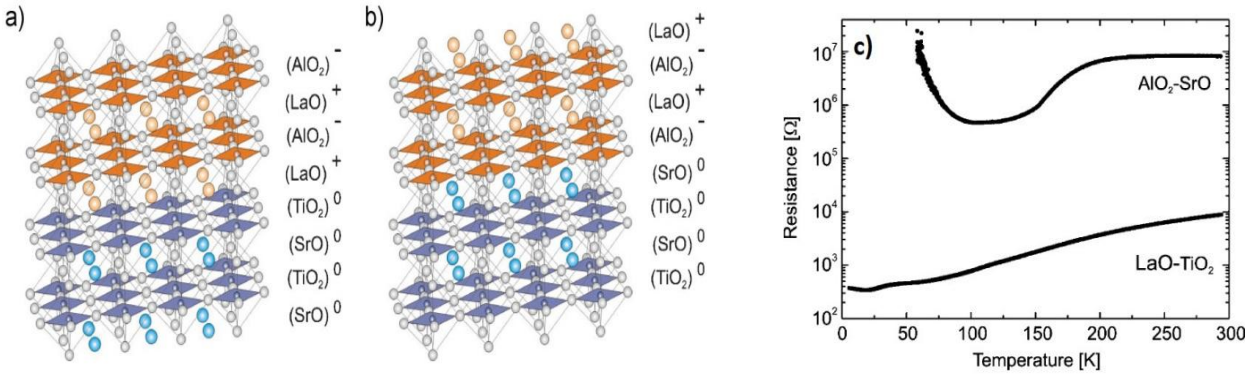

Figure 1.12 Illustration of the two possible atomic stackings for the abrupt $LaAlO_3/SrTiO_3$ heterointerface. a) TiO_2/LaO interface b) SrO/AlO_2 interface. (c) Temperature dependence of the resistance for TiO_2/LaO interface and SrO/AlO_2 interface, (re-printed with permission from [53]).

The 2DEG at $LaAlO_3/SrTiO_3$ interface generally behaves as a Fermi liquid with electron mobility $\mu \propto 1/T^2$ above ~100 K [58]. At room temperature, μ_{300K} ~ 6 $cm^2\ V^{-1}s^{-1}$. The low temperature value is related to sample quality. Values as high as μ ~1000 $cm^2\ V^{-1}s^{-1}$ at 5 K have been reported. Great efforts have been dedicated to enhance the mobility in $LaAlO_3/SrTiO_3$ and similar systems [49, 59].

More recently [59], a mobility enhancement by more than two orders of magnitude (exceeding 70,000 $cm^2\ V^{-1}s^{-1}$ at 2 K) in amorphous $LaAlO_3/SrTiO_3$ was achieved by introducing a single unit cell buffer layer of manganite, $La_{1-x}\ Sr_xMnO_3$ (x = 0, 1/8 and 1/3), at the interface of $LaAlO_3/SrTiO_3$. Besides, Chen. Y. Z. *et al.* [49] demonstrated that the interface between

spinel/perovskite epitaxial alumina (Al_2O_3) films and $SrTiO_3$ single crystal can show electron Hall mobilities as large as 1.4×10^5 cm^2 $V^{-1}s^{-1}$ at 2 K.

The electron density varies widely with fabrication parameters, such as substrate termination [53], oxygen pressure during deposition [60], thickness of $LaAlO_3$ layer [4] and capping of the $LaAlO_3$ [61]. In $LaAlO_3/SrTiO_3$ electron densities in the range 10^{13}-10^{14} cm^{-2}, 0.015-0.15 electron per unit cell at room temperature are often reported. Interestingly, almost all data converge to a value around 2×10^{13} cm^{-2} at low temperatures [61, 62].

Most likely the transport behavior follows from thermal activation of carriers at higher temperatures. The defects form a band of impurity states ~ 6 meV below the Fermi level [58]. When the temperature is high enough these electrons can use the thermal energy to be excited to the Fermi level [63] and hence can contribute to the conductivity.

1.6 Proposed Conduction Mechanisms

Several physical mechanisms which may cause a conducting interface between the polar $LaAlO_3$ film and the non-polar $SrTiO_3$ substrate have been proposed, including purely electronic charge transfer into the interface, the formation of defects in the vicinity of the $LaAlO_3/SrTiO_3$ interface and the catoin intermixing. An overview of these conduction mechanisms is presented below.

1.6.1 Polar Catastrophe Model

The origin of the 2DEG is to this day still highly debated. One popular explanation has its roots in a phenomenon known as the "polar catastrophe" [57]. $SrTiO_3$ and $LaAlO_3$ are similar materials in many ways, but there is one fundamental difference. The individual layers that make up $SrTiO_3$ (SrO^0 and $TiO^0{}_2$) have zero electrical charge, whereas as $LaAlO_3$ has alternating layers of charge ±1. The charged $LaAlO_3$ layers on TiO_2 terminated $SrTiO_3$ generate contributions to the internal potential as shown on the right side of Figure 1.13 (a). It is evident that an infinitely thick $LaAlO_3$ layer would generate an infinite potential. This is of course a very unfavorable situation which in reality will always be somehow avoided. One possible way to do this is the so-called "electronic reconstruction". In this reconstruction, 1/2 electrons per areal unit cell are transferred from the surface of the $LaAlO_3$ layer into the $SrTiO_3$ conduction band within the topmost TiO_2 layer at the interface [57]. As a result, the Ti valence state changes from

4+ to 3.5+, which induces *(n-type)* conductivity. The transfer of electrons as result of electronic reconstruction reduces the potential build-up as seen on the right side of Figure 1.13 (b). In this model, an interfacial sheet carrier density of $n_s = 3.2 \times 10^{14}$ cm^{-2} is expected. In the case of SrO terminated $SrTiO_3$, a p-doped layer should be expected, but the very low mobility of holes in $SrTiO_3$ would likely yield an insulating layer. Furthermore, the electron transfer takes place if the built-up potential is close enough, and this is only true in the case of $LaAlO_3$ thickness exceeding 3-4 unit cells (Figure 1.14 a).

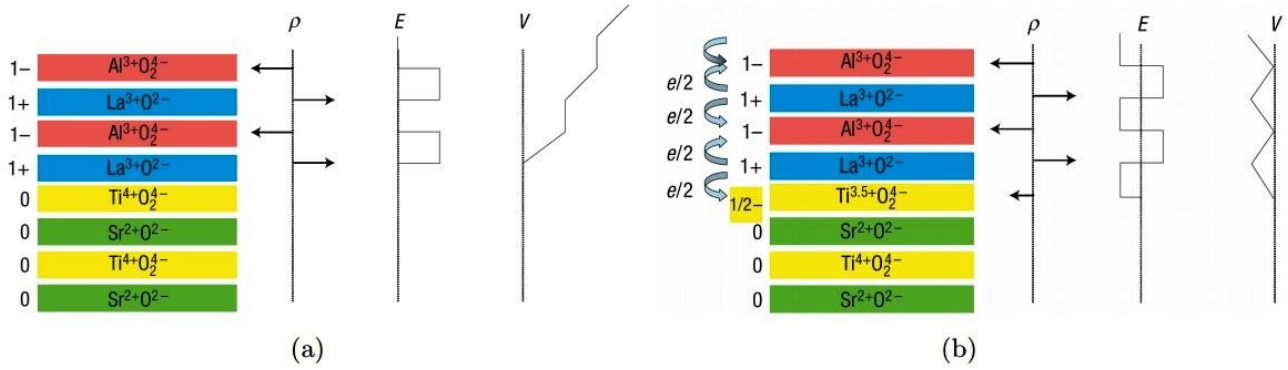

Figure 1.13: illustration of Polar catastrophe model in (a) unreconstructed case and (b) re-constructed case, where half an electron is transferred into the TiO_2 layer, (re-printed with permission from [57]).

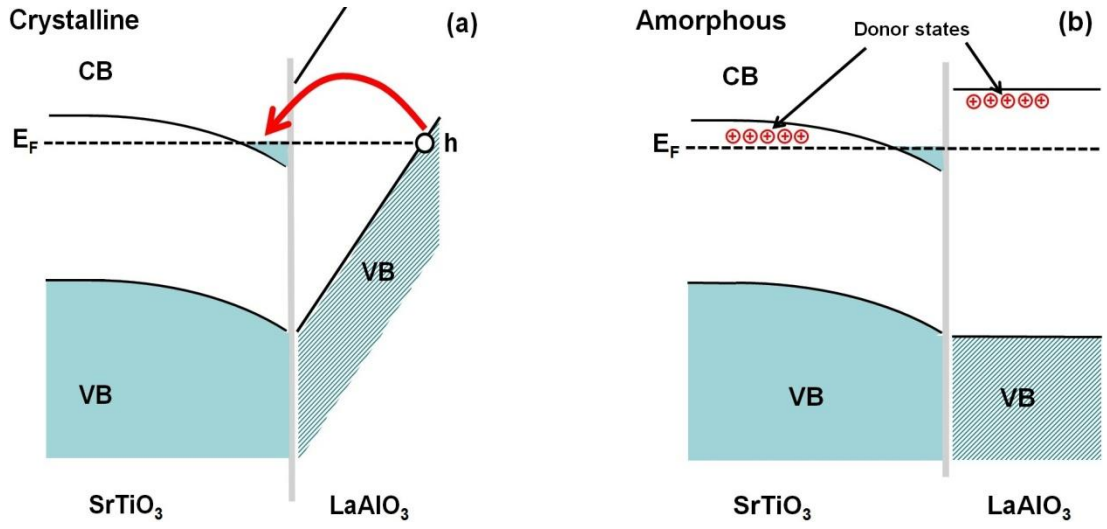

Figure 1.14 Sketch of the band structure of a) crystalline $LaAlO_3/SrTiO_3$ and b) amorphous $LaAlO_3/SrTiO_3$, (re-produced with permission from [64]).

Theoretical calculations based on *Density-Functional Theory (*DFT*)* show in fact a critical thickness typically around 4 unit cells [65].

As already described, experimentally ~ 0.15 electrons per unit cell area are transferred at room temperature. This is far below the nominal 1/2 electron per unit cell area transferred in the purely ionic model (about 3×10^{14} cm^{-2}). One reason for this discrepancy might be that the electrons are distributed over different sub-bands, of which only some contribute to the free electron density which can be determine from Hall measurements [66]. However, X-ray photoelectron spectroscopy (XPS) detects both free and bound electrons and the densities observed with XPS are close to those obtained from Hall measurements [67] perhaps indicate that other mechanism as well might be at play.

Similarly to $LaAlO_3$, $LaGaO_3$ and $NdGaO_3$ are constituted by alternate stack of positively charged A-planes and negatively charged B-planes, resulting in a polar discontinuity when epitaxially grown on $SrTiO_3$.

On the other hand, the band diagram for amorphous $LaAlO_3/SrTiO_3$ as shown in Figure 1.14 (b), is fundamentally different from crystalline. Due to the fact that $LaAlO_3$ is not epitaxially grown, there is no band bending on $LaAlO_3$ side so, that no electron reconstruction is expected [47]. Nevertheless, there are shallow donor states residing in the vicinity of the Fermi level on both sides of triangular quantum well. Presumably, the electrons from these donor states can populate the quantum well and can induce conductivity in amorphous $LaAlO_3/SrTiO_3$.

1.6.2 Oxygen Vacancies

$LaAlO_3/SrTiO_3$ interfaces are very sensitive to the oxygen pressure in which they are grown. A low oxygen pressure during growth leads to samples with much lower sheet resistance. During the low pressure growth some oxygen vacancies are first created in $LaAlO_3$, but due to the chemical potential gradient oxygen escape from $SrTiO_3$ to fill the vacancies in $LaAlO_3$ and leaves $SrTiO_3$ depleted [38].

The original paper by Ohtomo and Hwang [1] considered the possibility that the high carrier density in $LaAlO_3/SrTiO_3$ is due to oxygen vacancies acting as donors. This issue has been subsequently explored [52, 68] showing a strong influence of the deposition conditions on the interface transport properties. From the Brinkiman, *et al.* paper [52] it can be clearly seen that at increasing the oxygen pressure during the deposition of the $LaAlO_3$ layer the sheet resistance increases (Figure 1.15 a). Sheet resistance as low as ~ 10 Ω/□ can be obtained for $LaAlO_3$ grown at 1.0×10^{-6} mbar of oxygen partial pressure (O_2). There is a large jump, more than four order of magnitude in sheet resistance on going from 1×10^{-6} to 3.0×10^{-5} mbar O_2. By further increasing the growth pressure the system reaches a state where a *normal* interfacial conducting state, a superconducting state or a magnetically active state can be present due to factors other than oxygen contents. The transport properties of low-pressure grown $LaAlO_3/SrTiO_3$ samples are also very similar to doped $SrTiO_3$.

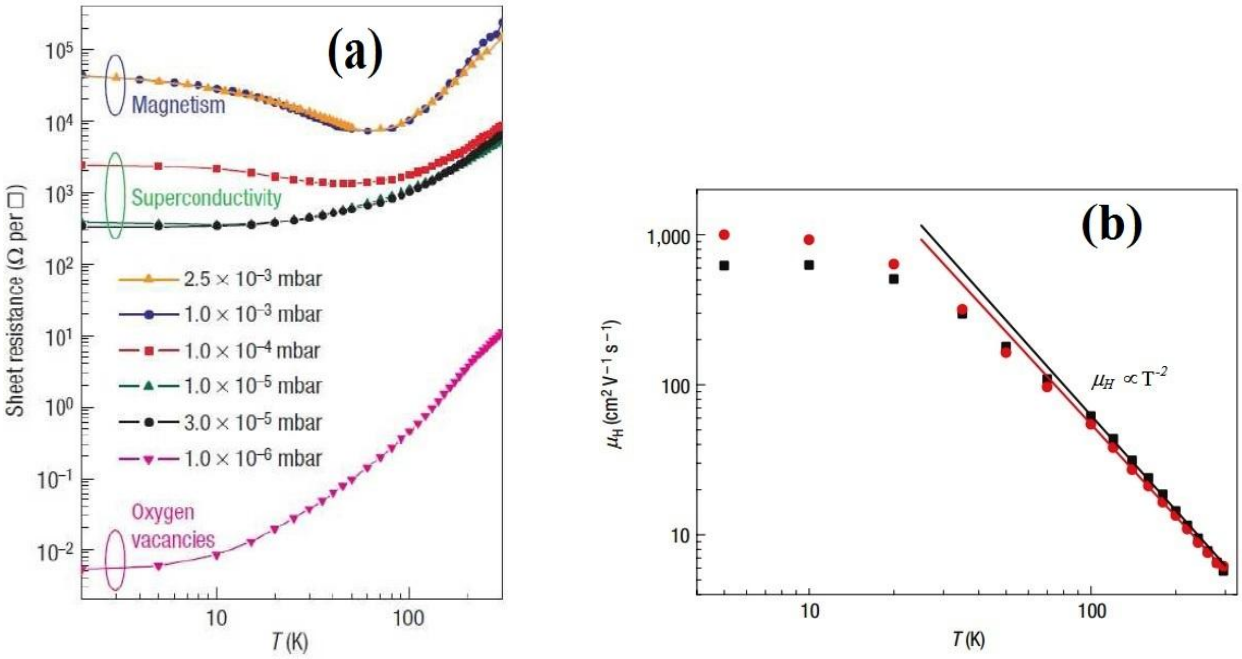

Figure 1.15 Sheet resistance versus temperature for samples grown by pulsed laser deposition under several oxygen pressures as indicated, (re-printed with permission from [52]). Temperature dependence of Hall mobility for $SrTiO_3/LaAlO_3/SrTiO_3$ heterostructures, (re-printed with permission from [58]).

The temperature dependence of the Hall mobility μ_H usually show a T^{-2} power-law dependence above 80 K (Figure 1.15 b). High mobility $LaAlO_3/SrTiO_3$ samples grown at 1.0×10^{-6} mbar of O_2 exhibit Shubnikov-de Haas oscillations [38] and blue light luminescence [69] similar to doped $SrTiO_3$ [39]. It is very difficult to disentangle the vacancy-dominated regime and the interface related regime: electron energy loss spectroscopy (EELS) measurements clearly show the presence of Ti^{3+} for samples at both 1.0×10^{-6} and 1.0×10^{-3} mbar of O_2 [70], but it is difficult to explain the 4 orders of magnitude jump in the sheet resistance from the observed Ti^{3+} signal.

1.7 Quantum Confinement

The charge carriers are confined in a region of ~ 5-10 nm close to the heterointerface [68]. The oxygen partial pressure and the annealing process influence not only the gas properties (see section 1.6.2) but also its spatial extension. In the low partial pressure of oxygen grown samples

(10^{-6} mbar and not annealed), the gas spreads over 10-100 μm in $SrTiO_3$ exhibiting a 3D character [38]. On the other hand, Bastelic *et al.* [71] showed, via cross-section conductive tip atomic force microscopy measurements, that annealing the samples changes the spatial extent to a few nanometers: the gas is confined at the interface and has a 2D character. Basically, the 2DEG in this case shares most properties with 2DEG at the interface of $SrTiO_3$ with vacuum, see e.g. section 1.4.6.

The simplest model for the confinement potential is a triangular potential well with Airy wave functions (Figure 1.8 b, upper part, and 1.16, zoom in-part). The confinement potential at heterointerface results in a complex subband structure [72]. The subband dispersion calculated for some particular electric field strength extends into the $SrTiO_3$. The potential on $SrTiO_3$ side is constant and match the conduction band minima (~ 300 meV). It reduces fairly quickly when approaching the interface forming a triangular quantum well. On the other hand, the potential has an infinite barrier on the $LaAlO_3$ side.

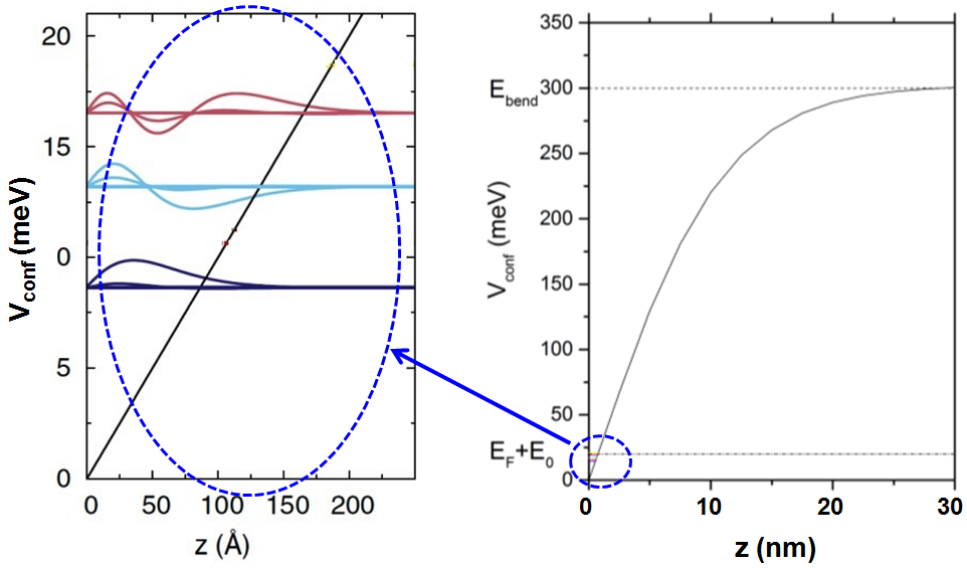

Figure 1.16 Confinement potentials a) triangular potential well with Airy wave functions, (re-produced with permission from [72])

It is worth mentioning here that for semiconducting heterostructures such as GaAs-AlGaAs hosting 2DEG, calculations have been done to model this potential well [73]. But this model cannot be directly applied to the $LaAlO_3/SrTiO_3$ interface for various reasons. First, the fundamental bulk band structure of $LaAlO_3/SrTiO_3$ includes several bands that geometrically differ the one from each other [72], while GaAs-AlGaAs has a single band. Second, the dielectric constant is constant across the GaAs-AlGaAs interface, while in the case of $LaAlO_3/SrTiO_3$ it is highly discontinuous. Furthermore, the dielectric constant of $SrTiO_3$ itself is strongly electric-field and temperature dependent [28]. These complexities make the confinement in the $LaAlO_3/SrTiO_3$ system harder to model than in the GaAs-AlGaAs system.

1.8 External Doping Mechanism

The transport properties at complex oxide interfaces can be tuned by modulating its carrier density by some external agents. This has been successfully done by light illumination [48], or by electric field effect [4]. Both of these doping mechanisms are discussed below**.**

1.8.1 Photo-doping

Light illumination is a tool that is widely used in semiconductors to generate extra carriers by exciting trapped electrons [74]. The main contribution to photoconductivity is captured by the following simple equation:

$$\Delta\sigma = \Delta n\, e\, \mu$$

where $\Delta\sigma$ is the change in sheet conductivity due to light illumination and Δn is the number of photo-excited carrier. The case might be complicated if the mobility (μ) also changes [48]. If we neglect the possibility that a large number of holes are formed (i.e. $\Delta n << n$, where n is the total sheet density in conduction band after excitation), then the optical excitation is represented by the following simple rate equation:

$$\frac{\partial n}{\partial t} = \alpha\ \Phi - \frac{\Delta n}{\tau}$$

where Φ is the incident photons flux, n_o is the sheet carrier density such that $n = n_o + \Delta n$. The last term in equation accounts for the recombination rate with some characteristic time τ.

Photoconductivity may be due to intrinsic or extrinsic excitations [75]. By extrinsic photoconductivity we mean the effect of defects (or trap states) ionization. These ionization energies can be measured and thus provide a spectroscopic technique to get the in-gap defect levels as demonstrated for GaN heterostructures [76] and CdSe alloys [77]. The intrinsic mechanism instead regards the direct promotion of electron from the valance band to the conduction band [78]. In several cases the hole conductivity sum up to the electrons conductivity but for $SrTiO_3$ it was proved that holes are trapped [33].

After the first report of photoconductivity in $LaAlO_3/SrTiO_3$ by Tebano et.al [2] several research groups deeply investigated this phenomenon [48, 79, 80]. For example, Di Gennaro [48] *et al.* studied the photoconductivity in $LaGaO_3/SrTiO_3$ and $NdGaO_3/SrTiO_3$ interfaces. Chan *et al.* [80] enhanced the photoresponse by using Pd nanoparticles. Irvin *et al.* have investigated the photoresponse on the nanoscale and developed the rewritable oxide photodetectors [79].

Many studies [2, 48] reveal that the conductivity in these kinds of interfaces is persistent in nature, i.e. there is still some photoconductivity even after the cessation of optical excitation. The persistent photoconductivity is interpreted in terms of a separation of the electron-hole pairs in real space by an intense built-in electric field. Such separation hinders the recombination process and leads to very long lifetimes of the photoexcited states. Lu *et al.* [81] have found that the insulating state of the interface can be converted to metallic state by the light illumination and made the $LaAlO_3/SrTiO_3$ interface as a promising nonvolatile memory.

1.8.2 Electrostatic Doping

The electron density in 2DEGs at oxide interfaces can be very effectively modulated by the electric field [4]. Such possibility has been successfully exploited to tune the properties of the $LaAlO_3/SrTiO_3$ system, e.g. spanning the superconducting phase diagram [51] or tuning the spin-orbit coupling [82]. This technique can be so effective for insulating samples (i.e. with $LaAlO_3$

thickness below the threshold) that it can drive the samples to the conducting state [4] (Figure 1.17 b).

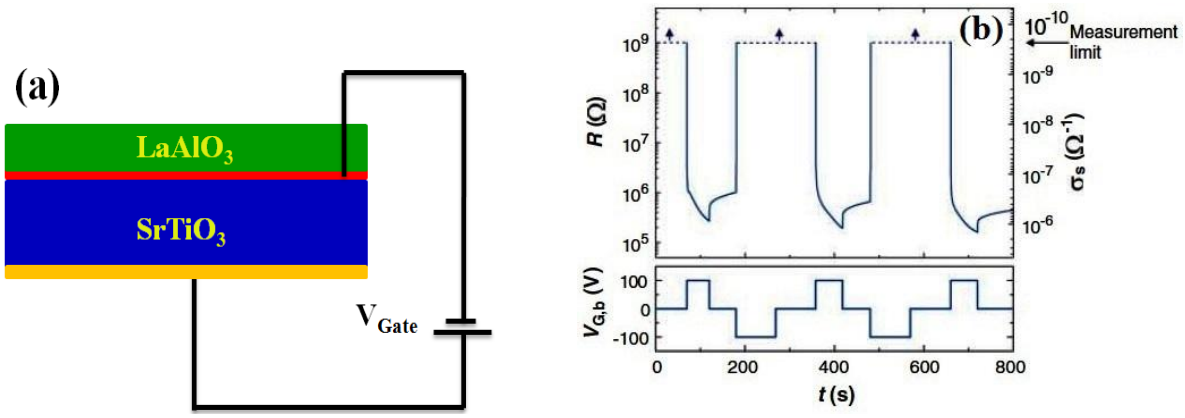

Figure 1.17 (a) Schematic of the back gated $LaAlO_3/SrTiO_3$ (b) metal to insulator transition of 3 unit cells thick $LaAlO_3$ film at 300 K as function of gate bias, (re-printed with permission from [4])

Typically, the voltage is applied by back-gating to the $SrTiO_3$ substrate (Figure 1.17 a). For $V_G > 0$, electrons are added to the 2DEG and the conductivity increases. In the opposite case ($V_G < 0$) the conductivity decreases.

A gated $LaAlO_3/SrTiO_3$ structure can be modeled as a simple parallel plate capacitor [83]. This model takes into account the device geometry and the dielectric constant of the material (ε_r). The capacitance of a system relates an accumulated charge on a capacitor to the voltage drop across that capacitor. For a parallel plate capacitor, the expression reads

$$C = \frac{\varepsilon_o \, \varepsilon_r \, A}{d}$$

where A is the sample area and d is the substrate thickness. As already discussed in section 1.4.4, the dielectric constant of $SrTiO_3$ is strongly temperature and electric field depend [27]. Presently limiting the analysis to the case of small signals, we have

$$\Delta n = \frac{\Delta Q}{e} = \frac{\varepsilon_o \, \varepsilon_r}{e \, d} V$$

This expression shows that the density of the 2DEG can be increased (decreased) by the application of a positive (negative) gate voltage to the sample (Figure 1.17 a).

However, literature reveals that the $LaAlO_3/SrTiO_3$ cannot be simply interpreted in terms of such simplified model due to a quite complex response of the transport properties of the 2DEG to the solicitation of gate voltage. Bell *et al.* [84] and more recently Biscaras *et al.* [3] demonstrated that very anomalous effects occur during and after the application of a positive backgate voltage. Very recent study [85] showed the combined effect of light and electric field on $LaAlO_3/SrTiO_3$, demonstrating some unexpected interplay between the two effects.

Chapter 2

Photoconductivity of Oxides Interface

Abstract

The first part of chapter 2 presents the fabrication procedure of samples, transport characterization via Van der Pauw and Hall Method, and the photoconductivity setup. In the second part, the study of photoconductivity of different oxide interfaces under illumination of variable wavelengths and intensities is presented. A model based on the band diagram is introduced to describe the results. The data allow some considerations on the nature and distribution of defects that are excited by the light.

2.1 Sample Fabrication

The samples investigated in this work have been fabricated at the MODA (Modular facility for Oxide Deposition and Analysis) deposition system at the CNR-SPIN institute, Department of Physics, University of Napoli "Federico II", Italy. The MODA system mainly consists of two major parts: i) thin film growth chamber and ii) the analysis chamber (Figure 2.1). The thin films are grown by *Reflection high-energy electrons diffraction*-RHEED assisted pulsed laser deposition (PLD).

Even though the fabrication process is not the core of this work, it is worthwhile mentioning a few details of the PLD fabrication because it strongly affects the transport properties of the interfaces. More details about PLD can be found in Ref. [86, 87].

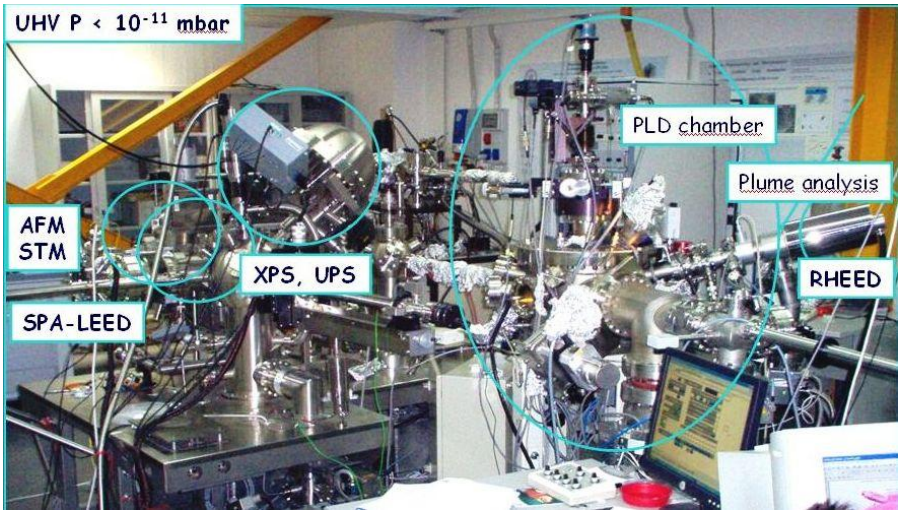

Figure 2.1 MODA Laboratory in Naples, Italy.

2.1.1 Pulsed Laser Deposition

Pulsed laser deposition (PLD) is a powerful deposition technique which is widely used to transfer the complex stoichiometry of multi-component target materials into thin films. During PLD, the desired film material is ablated from a target under specific vacuum conditions by high energetic nanosecond laser pulses. If the laser energy density is sufficient for ablation of the source target, the material evaporates, perpendicular to the target surface, forming a gas plasma with a characteristic shape called *plume*. The plume consists of a mixture of atoms, molecules, ions and clusters. During its expansion, internal thermal and ionization energies are converted into the kinetic energy of the ablated particles. The processes in the plume during transport are influenced by the background gas parameters, and, as a result, characterize the kinetic energy of the particles arriving at the substrate. The kinetic energy can be varied from high energy (~100 eV) in vacuum to low energy (~1 eV) at large ambient pressures and can be used to modify the thin film growth [88, 89].

The substrate material is glued usually by silver paste on a heater placed in the center of the plasma plume in a typical distance of several centimeters from the target. The incident plasma particles nucleate on the surface of the substrate and start to form a film.

The stoichiometry of the deposited films is a result of the complex interplay between laser ablation process and plasma kinetics during the deposition [90]. Thus, the tuning of the process parameters is a crucial prerequisite to obtain high quality epitaxial oxide thin films and heterostructures. Moreover, the controlled variation of the parameters can be used to fine-tune the stoichiometry of the deposited films.

The most important parameters for the PLD of oxide thin films are the laser fluence, the oxygen background pressure, and the substrate temperature. The laser fluence determines the material ablation process. The oxygen background pressure influences the plasma expansion, the kinetic energy of the ad-atoms and their oxidation state. Oxide thin films grown in low background pressure of oxygen have usually high level of defects in the form oxygen vacancies. These defects can be avoided by growing films in high oxygen pressure or by post annealing treatment in oxygen environment [53]. The substrate temperature determines the mobility of the ad-atoms on the surface of the growing film [90]. In order to provide an epitaxial growth of the film, the substrates are heated up to temperatures between 550 °C and 850 °C. At these deposition temperatures, the ad-atoms are able to move on to energetically favored positions on the surface, which leads to a well ordered growth. On the other hand, the films grown at room temperature are highly disorder polycrystalline or even amorphous [47].

The thin films investigated in this work were typically grown by PLD technique on TiO_2-terminated (001) $SrTiO_3$ single crystal substrates having dimensions (length × width × trickiness, $5 \times 5 \times 0.5$ mm^3), resorting to a KrF excimer laser beam (248 nm) with a fluence in the range of 1.3-1.5 J/cm^2 on target and a repetition rate of 1-2 Hz. The crystalline samples were grown at high temperatures range between 600 °C and 800 °C in oxygen partial pressure of 10^{-4}-10^{-2} mbar. After the deposition, the samples were cooled in 1 h to room temperature in the same pressure condition. The amorphous samples were grown at room temperature in oxygen partial pressure of 10^{-4}-10^{-2} mbar.

2.2 Transport Properties

The electrical transport measurements were performed in standard four-probe Van der Pauw configuration [91] , discussed below in section 2.2.1. The resistance was measured in DC mode, by biasing the samples with a current source and measuring the voltage drop with a nano-voltmeter. All the samples were contacted by ultrasonically bonded aluminum wires. To compute the resistance of the samples, unless otherwise stated, a 10 μA current was fed and the consequent voltage drop was measured. The closed cycle refrigerator system, combined with the Lakeshore temperature controller model 331 was used to investigate the transport properties of materials in a temperature range 300-10 K. The details about closed cycle refrigerator system can be found in Ref. [87]

2.2.1 Van der Pauw Method

Generally, in resistivity measurements, it is often difficult to determine accurately the geometry of the sample, limiting the accuracy of the calculated resistivity. In such a case, one often uses the technique of van der Pauw to determine the resistivity of the sample. This technique is applicable for samples of uniform thickness, and of homogeneous and isotropic electrical properties. Additionally, contacts must be taken at the edges of the sample, and their size must be much smaller than the sample size. Figure 2.2 shows a generic four-point van der Pauw configuration. By sourcing a current I through contacts 1 and 2, and measuring the voltage drop ΔV through contacts 3 and 4, the resistance is given by

$$R_{12,34} = \frac{V_{34}}{I_{12}}$$

According to the reciprocity theorem of network analysis: $R_{12,34} = R_{34,12}$. By switching the polarity of the current source, and the voltage meter, one can determine averaged values for $R_a = (R_{12,34} + R_{21,43})/2$, and $R_b = (R_{23,41} + R_{32,14})/2$. In turn, van der Pauw derived the following relation for an arbitrary shaped sample

$$\exp\left(-\frac{\pi}{R_{sheet}}\right)R_a + \exp\left(-\frac{\pi}{R_{sheet}}\right)R_b = 1$$

where R_{sheet} is the sheet resistance define as

$$R_{sheet} = \frac{\rho}{t}$$

with ρ resistivity and "t" thickness of the conducting layer (i.e. the resistivity of the two-dimensional electron gas (2DEG) residing in the quantum well of thickness t). In general, the van der Pauw formula cannot be rearranged to give the sheet resistance R_{sheet} in terms of known functions. The most notable exception to this is when the sample is isotropic square sample i.e. $R_a = R = R_b$; in this scenario the sheet resistance is given by

$$R_{sheet} = R\frac{\pi}{\ln(2)}$$

The sheet resistance of 2DEG is generally measured in ohms per square (or Ω/□).

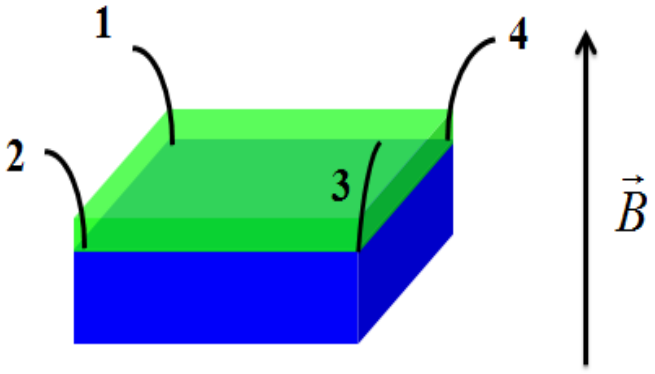

Figure 2.2 Van der Pauw configuration for resistance measurement. The arrow indicates the direction of the magnetic field $\vec{B}$ that is applied in Hall measurements.

2.2.2 Hall Measurement

Electrical measurements as a function of magnetic field allows for variety of transport properties such as electron density and mobility to be determined through well know Hall Effect [92]. The Hall data for this study were collected by using RH 2010 Hall measurement system in the Fondazione Bruno Kessler (FBK) laboratory in Trento. Some measurements were also performed by a setup in CNR-SPIN laboratory in Naples. A simple description of the technique is given below.

The electric current that flows through a conductor in a magnetic field experiences a transverse force on the moving charge carriers which tends to push them to one side of the conductor. A buildup of charge at the sides of the conductors will balance this magnetic influence, producing a measurable voltage, known as Hall voltage (V_H), between the two sides of the conductor.

In order to perform Hall measurements in the Van der Pauw configuration, the current I is fed across terminal 1,3 and the Hall voltage is read across 2,4, or vice versa (Figure 2.2). As known the Hall voltage V_H is by

$$V_H = \frac{R_H}{t} IB$$

where t is the sample thickness and B is the intensity of the applied magnetic field. The parameter R_H is called the Hall coefficient. Once R_H/t is experimentally determined as a proportionality factor between V_H and (I B), one promptly gets the sheet carrier density n as

$$n = \frac{1}{e}\frac{t}{R_H}$$

hence the mobility is found as

$$\mu = \frac{1}{ne}\frac{t}{R_H}$$

Note that (R_H/t) must be determined by linear regression on the V_H-I curves in order to get rid of possible offsets due to emf (electromotive force). Furthermore if the contacts that are used to

probe V_H are not exactly aligned in a direction perpendicular to the current flow, V_H is affected by a spurious ohmic voltage drop. This is eliminated by averaging with measurements performed at opposite B values, as automatically done.

2.3 Photoconductivity Setup

The schematic of the photoconductivity setup used in this study is shown in Figure 2.3. This set-up was developed for electrical and photoconductivity measurements in direct current (DC) mode. The set-up mainly consists of two parts, cryogenic and optical. The sample inside the cryogenic system is separated from the environment by metallic/silver cap having transparent quartz window that allow the light to illuminate the sample directly. A calibrated Si photodiode (Thorlabs-FDS100) was used to measure the light intensity. From the responsivity and voltage drop across the photodiode, the power density was measured which was converted to photon flux counted as *number of photons* s^{-1} cm^{-2}. The photodiode was installed very close to the sample so that the illuminated spot from the light source exposes uniformly and homogenously both the sample and the photodiode. The illuminating sources consist of the following lines:

- UV light, with $\lambda = 365 \pm 10$ nm ($h\nu = 3.40$ eV)
- Blue light, with $\lambda = 445 \pm 10$ nm ($h\nu = 2.70$ eV)
- Green light, with $\lambda = 540 \pm 10$ nm ($h\nu = 2.30$ eV)
- Red light, with $\lambda = 625 \pm 10$ nm ($h\nu = 1.98$ eV)

Some measurements were also performed by different illuminating sources. The monochromatic radiation was obtained by using a Xenon lamp and band-pass interference filters (FWHM 10 ± 2 nm). The selected wavelengths in this case are given below:

- $\lambda = 500 \pm 10$ nm ($h\nu = 2.48$ eV)
- $\lambda = 400 \pm 10$ nm ($h\nu = 3.10$ eV)
- $\lambda = 255 \pm 10$ nm ($h\nu = 4.88$ eV)

The light intensity was attenuated by means of neutral optical density filters in order to obtain fixed photon flux at each wavelength. The optical part further consists of two bi-convex lenses, having diameter 2" each, and with focal lengths 75 and 60 mm mimicking a conventional

telescope. A proper arrangement was done to isolate and shield the photoconductivity setup from the ambient light.

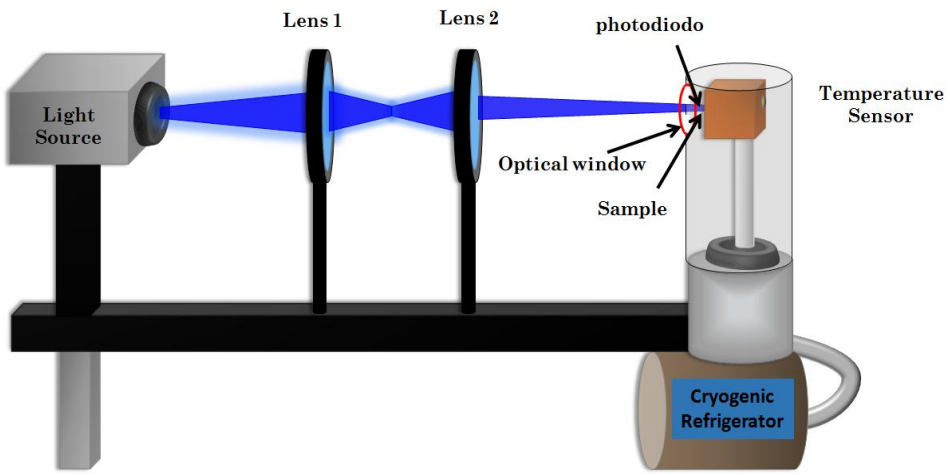

Figure 2.3 Schematic of the photoconductivity set-up

2.4 Transport Properties of Interfaces

Several 2DEGs formed at oxide heterostructures, including crystalline and amorphous $LaAlO_3/SrTiO_3$, γ-$Al_2O_3/SrTiO_3$ and $LaGaO_3/SrTiO_3$ were analyzed in this study. Comparing crystalline and amorphous systems is potentially interesting, because the crucial difference between the two systems consists in the amount of oxygen vacancies that, acting as point defects, may play a role in the conductance and in the photoresponse. The thickness of the overlayer in crystalline samples was ~ 20 nm each, while for the amorphous samples the overlays thicknesses were between 2.4-4 nm. The summary of the fabrication and transport properties of the samples is reported in Table 2.1.

Figure 2.4 shows a comparison of sheet resistance vs. temperature curves for some of the investigated samples. All the hetero-interfaces showed metallic behavior down to 10 K. However a-$LaAlO_3/SrTiO_3$ at times shows small resistance upturn at low temperatures, probably due to

localization effects [93]. The R_{sheet} (T) curves of γ-Al_2O_3/$SrTiO_3$ is also qualitatively similar to that of c-$LaAlO_3$/$SrTiO_3$.

R_{sheet} at room temperature ranges between ~ 5-100 Ω/□ (see Table 1.2). The room temperature mobilities in these hetero-interfaces are almost constant at value ~ 5 $cm^2.V^{-1}.s^{-1}$, indicating that the room temperature sheet resistance is mainly determined by the sheet carrier density.

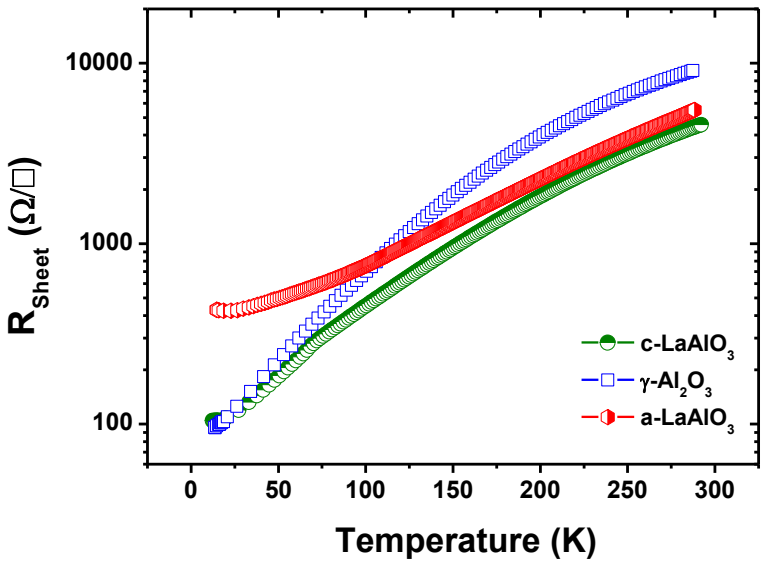

Figure 2.4 R_{sheet} (T) curves for crystalline and amorphous $LaAlO_3$/$SrTiO_3$, γ-Al_2O_3/$SrTiO_3$ collected in dark

Table 2.1: Summary of the fabrication and room temperature transport properties of some samples investigated in this study.

System	***Thickness*** ***(uc)***	***PO_2*** ***(mbar)***	***R_{Sheet}*** ***(Ω/□)***	***n_{2D}*** ***(cm^{-2})***	***μ_{300K}*** ***($cm^2.V^{-1}s^{-1}$)***
c-$LaAlO_3$/$SrTiO_3$	50	3×10^{-2}	20.4	5.5×10^{13}	5.3
c-$LaGaO_3$/$SrTiO_3$	50	3×10^{-2}	5.80	1.7×10^{14}	6.2
γ-Al_2O_3/$SrTiO_3$	50	1×10^{-4}	41.2	2.7×10^{13}	5.0
a-$LaGaO_3$/$SrTiO_3$	10	1×10^{-4}	67.8	2.0×10^{13}	4.8

2.5 Scope of Photoconductivity

A general procedure was adopted for all photoconductivity measurements. The light sources were pre-heated for 20 minutes to get a stable light. The samples were kept in dark for at least 12 hours before the first measurement in order to suppress the photoconductivity effect due to previous exposure or ambient light. In order to provide uniform experimental conditions, all the measurements were collected at 300 K (thermodynamically controlled) in vacuum (10^{-2} mbar). The samples were illuminated for 20 minutes followed by a recovery of 1 hour.

Qualitatively, the samples show a significant increase of the conductivity when exposed to the light of suitable wavelengths. The common feature of the investigated interfaces is that the photoconductivity is persistent in nature, i.e. the samples do not recover the initial state after light exposure has been turn off.

As an example, Figure 2.5 shows the photo-response of amorphous $LaGaO_3/SrTiO_3$ which is exposed to a monochromatic ultraviolet (UV) radiation of photon flux $\Phi = 8 \times 10^{14}$ s^{-1} cm^{-2}, provided by a light emitting diode source. The UV light has energy 3.4 eV ($\lambda = 365 \pm 10$ nm), larger than $SrTiO_3$ in direct band gap (~3.2 eV). The sheet photoconductivity $\sigma_{ph}(t)$ is defined as the difference between the sheet conductivity $\sigma(t)$, measured at time t during the light illumination, and the sheet conductivity in dark conditions before the illumination, σ_o. The photoresponse dynamics shows a sharp increase with response time < 1 s, followed by a slower temporal behavior. The sheet conductivity is increased by more than 30 % with respect to initial dark sheet conductivity (σ_o) in the light illumination session of 20 minutes. The decay was followed for 1 hour, showing that even after the light has been turned off, it still preserves ~17 % of the photoconductivity.

The investigation of samples (Table 2.1) at different wavelength and illumination intensities reveal that the recovery time can vary from 1 hour to more than 24 hours. For red/green and blue light, recovery time is about 1 and 3 hours respectively. For photons at 365 nm, it took more than a day for the samples to restore the initial dark state.

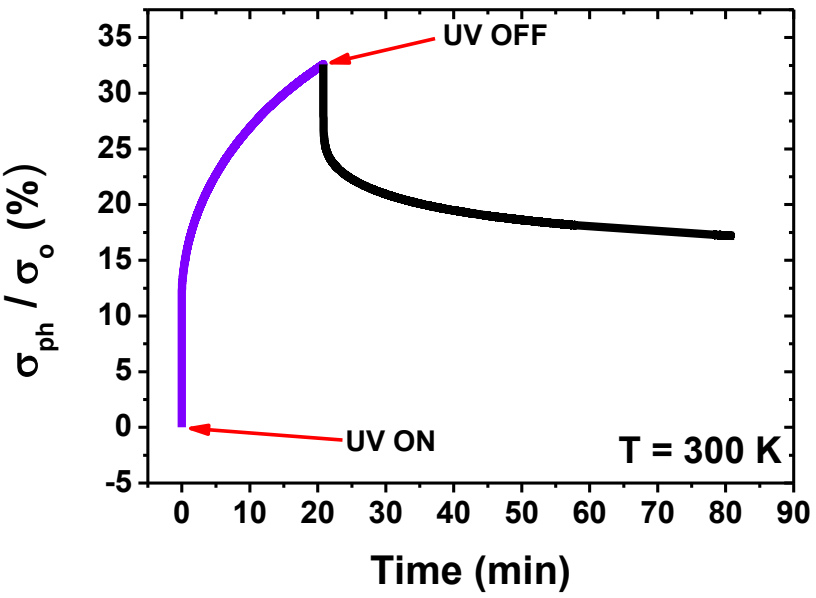

Figure 2.5 Normalized photoconductance rise and subsequent decay collected on a-$LaGaO_3/SrTiO_3$ sample

2.6 The Linear Regime of Photoresponse

A set of measurements was specifically deviated to the assessment of the conditions that give a linear regime of photoresponse. For this purpose 445 nm radiation was varied in the range of photon flux from $\Phi = 2 \times 10^{14}$ to $\Phi = 2.2 \times 10^{15}$ s^{-1} cm^{-2}. Figure 2.6 (a) shows the photoresponse dynamics induced by this blue light at various photon flux for one c-$LaAlO_3/SrTiO_3$.

The photoresponse shown in Figure 2.6 (a) can be considered as typical. It shows a relatively sharp increase in photoconductance, followed by a slow dynamical behavior. The photoresponse is characterized by the quantity σ_{ph}/σ_o, where σ_o is the dark sheet conductivity. As evident from the Figure 2.6 (a), the photoresponse scales with photon flux up to $\Phi = 8 \times 10^{14}$ s^{-1} cm^{-2}, i.e. it increased from ~ 0.01 to ~ 0.025. Above $\Phi = 8 \times 10^{14}$ s^{-1} cm^{-2} no increase in sheet conductivity is seen indicating a saturated regime. It is anticipated that photons at 445 nm mainly excite the in-gap states related to impurities. The observation of saturation is then reasonably due to substantial promotion of most available electrons from the trap states to the conduction band.

The final values of the σ_{ph}/σ_o after 20 minutes of light exposure at different photon flux endorse crossover from linear to saturated regime at increasing intensities (Figure 2.6 b). The range for linear regime was also checked for other wavelengths. The measurements that are reported in the following section were performed in the low photon flux, linear regime. The linear and saturated regimes are discussed in section 2.8.

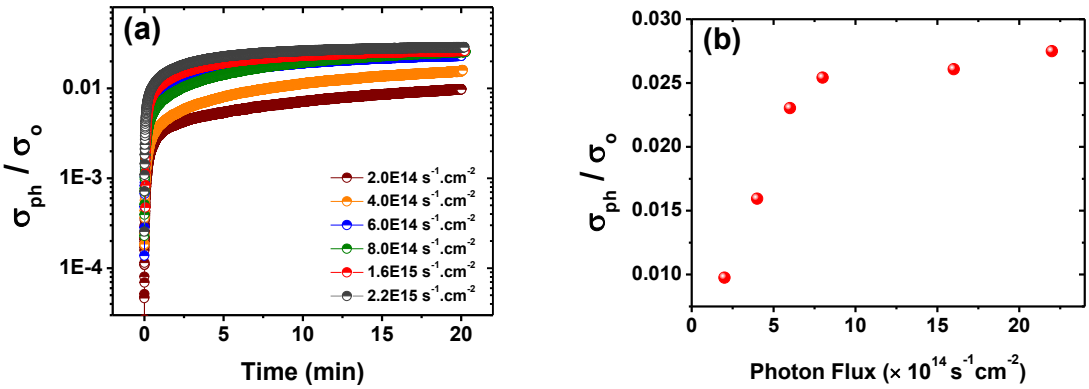

Figure 2.6 (a) Comparison of normalized photo conductance for c-$LaAlO_3$/$SrTiO_3$ at 445 nm at different photon flux (b) final value of photoconductance after 20 minutes of illumination as a function of photon flux indicating linear and saturation regime.

2.7 Dependence of Photoresponse on Wavelength

In order to get an insight of the photo promotion mechanism in different hetro-interfaces several wavelengths were considered to perform photoconductivity measurements. Along with the UV, particularly the wavelengths whose corresponding energies are smaller than the indirect band gap of $SrTiO_3$ (~ 3.2 eV) has been chosen. This choice is very interesting for the mid-gap promotion of the carriers. All the measurements were carried out at the same photon flux $\Phi = 4 \times 10^{14}$ s^{-1} cm^{-2}, i.e. in the linear regime.

Qualitatively the results from the investigated samples are similar. Figure 2.7 shows the time evolution of the photo-conductance induced by four different wavelengths for c-$LaAlO_3$/$SrTiO_3$. The photo-response dynamics shows a relatively steep increase of photo-conductance, followed

by a slower transient behavior. The time evolution of the photo-conductance further shows that, during the exposition, samples exhibit a distinct response for the light of different wavelengths.

The response to the incident light radiation is directly related to the number Δn of electrons promoted into the conduction band.

Basically, high energy photons can excite electrons from valance band to conduction band, while low energy photons can only excite electrons from in-gap trap states. As a result, the photoresponse becomes lower and lower at increasing wavelength; it decreased nearly by one (two) order of magnitude for blue (green/red) light. Since the measurements were conducted by the same photon flux at all wavelengths, and considering that each process of photo-excitation generates one free carrier, it follows that the variation of photo-conductance with wavelength just reflects the variation of photo-generation efficiency.

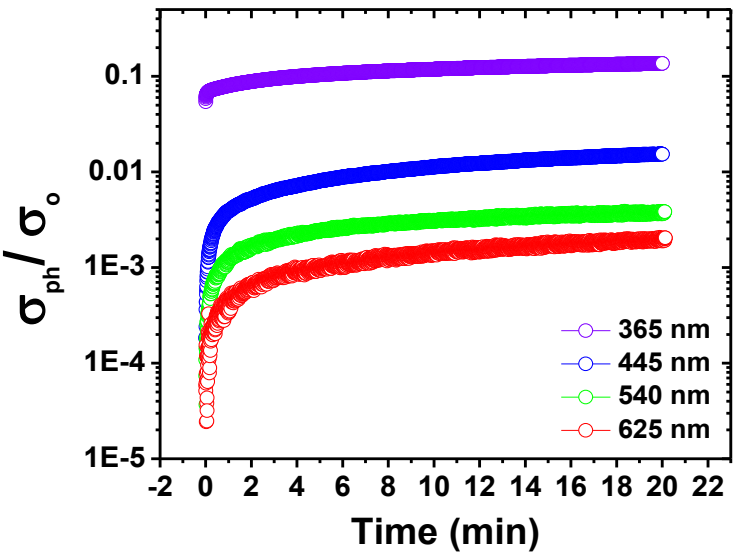

Figure 2.7 Comparison of photo-conductance at different wavelengths and at fixed photon flux Φ = 4×10^{14} s^{-1} cm^{-2} for c-$LaAlO_3$/$SrTiO_3$

The conductivity increase after light is tuned on always characterized by a steep onset followed by a slower transient. The single exponential function cannot describe this process very well. In principle, several functional expressions may be adopted to describe this behavior, including double exponential [48, 64] or stretched exponential functions [94]. In this study the fittings were made by using the following function

$$\sigma_{ph}(t) = \sigma_{\infty} \left\{ A \left[1 - \exp\left(-t/\tau_1\right) \right] + \left(1 - A\right) \left[1 - \exp\left(-t/\tau_2\right) \right] \right\} \qquad 2.1$$

where τ_1 and τ_1 are two characteristic times indicating, respectively, the recombination times of fast and slow processes and σ_{∞} is the saturation value of sheet photo-conductance. Furthermore, A and $1-A$ are the relative weight of the fast and slow components, respectively. The fits were made for all of the investigated samples, but here the fits are only shown for c-$LaAlO_3$/$SrTiO_3$ (Figure 2.8 a-d). The fitting parameters obtained for some samples from the photoresponse of four wavelengths are reported in Table 2.2.

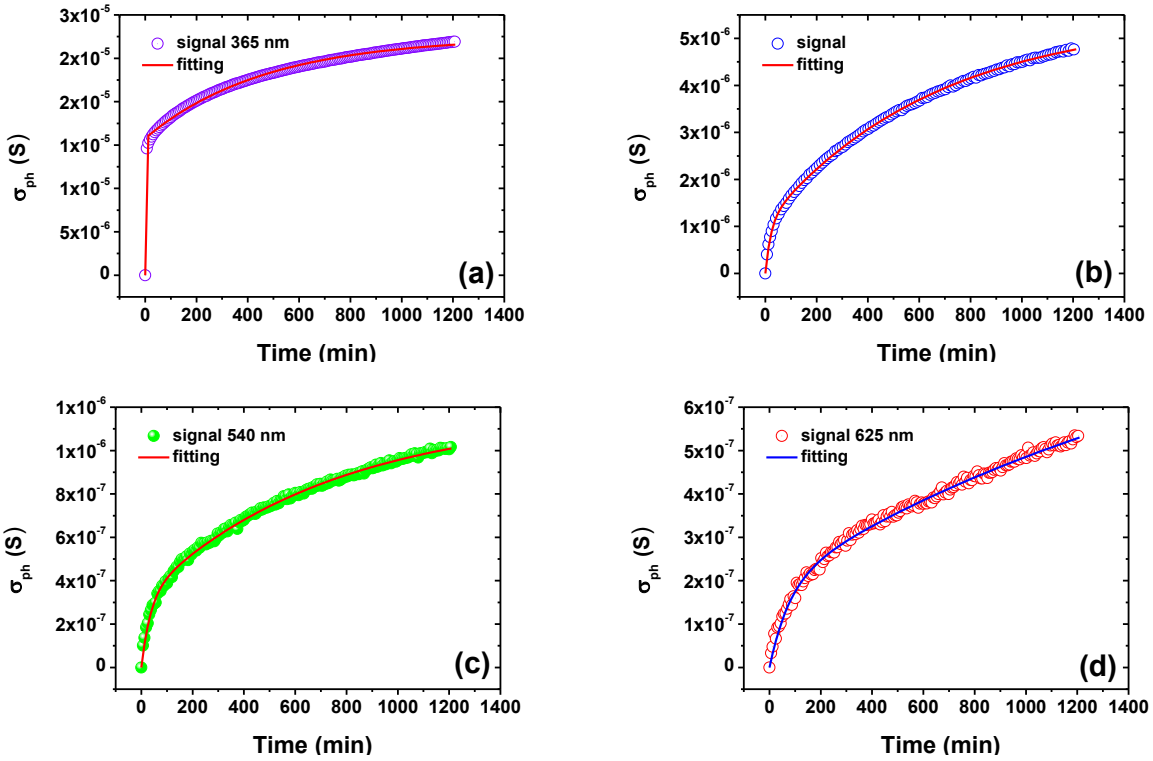

Figure 2.8 Sheet photoconductance of c-$LaAlO_3$/$SrTiO_3$ at (a) 365 nm (ultraviolet), (b) 445 nm (blue), (c) 540 nm (green) and (d) 625 nm (red). The solid lines are fit curves.

The parameters and particularly σ_∞, τ_1 and A, vary with wavelength approximately in the same way for all the samples. For instance, τ_1 decreased from ~ 72 s at 625 nm to ~ 0.4 at 365 nm for c-$LaAlO_3$/$SrTiO_3$ (Table 2.2). However the slow characteristic time τ_2, probably also due to the limited statistical weight of this parameter, resulting in a large error after the fit, shows quite scattered values.

In the photoresponse investigation different kind of interfaces was considered. Since qualitatively they share the same behavior therefore for simplicity only the comparison between crystalline and amorphous $LaAlO_3$/$SrTiO_3$ is presented below.

The full photoresponse is parameterized by $\sigma_\infty/\sigma_0\Phi$, mainly representing the quantum photogeneration efficiency. In Figure 2.9, $\sigma_\infty/\sigma_0\Phi$ is plotted vs. photon energy for two samples,

i.e. crystalline and amorphous $LaAlO_3/SrTiO_3$. In both cases the full photoresponse increases exponentially with energy. However, the photoresponse is much higher for the amorphous sample.

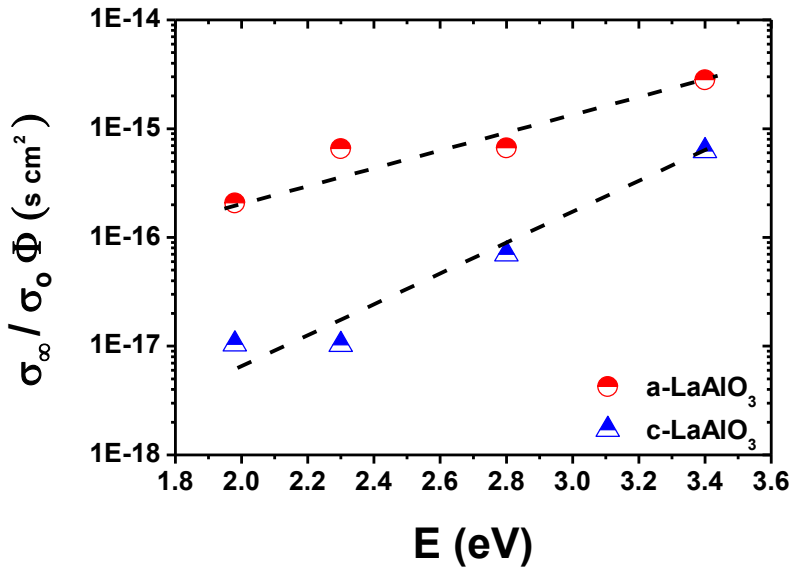

Figure 2.9 Full photoresponse vs. energy for amorphous and crystalline $LaAlO_3/SrTiO_3$ samples collected at photon flux $\Phi = 4\times 10^{14}$ s^{-1} cm^{-2}. Dash lines are guides for the eye.

The full photoresponse can be split in two contributions, related to the fast and to the slow characteristics times, by introducing the following two parameters:

$$fast\ component \Rightarrow = \frac{A\, n_\infty}{\Phi\, n_o}$$

$$slow\ component \Rightarrow = \frac{(1-A)\, n_\infty}{\Phi\, n_o}$$

The fast component of the signal shows for all samples an exponential growth with energy (Figure 2.10 a), similar to previous crystalline samples [48, 64]. The fast component increased from ~ 1.7×10^{-18} s cm^2 at 1.98 eV to ~ 3.0×10^{-16} s cm^2 at 3.4 eV for c-$LaAlO_3/SrTiO_3$. The plot indicates that in all samples the fast channel is almost suppressed at low photons energy, so that

the signal rise becomes slow. The slow component also increases with increasing energy (Figure 2.10 b). It was found that the fast component shows very similar overall behavior in all samples, while the slow component has a large spread (see discussion in section 2.8). This observation seems to suggest that the former component depends on intrinsic properties of the interfaces, while the later may be mainly due to defects.

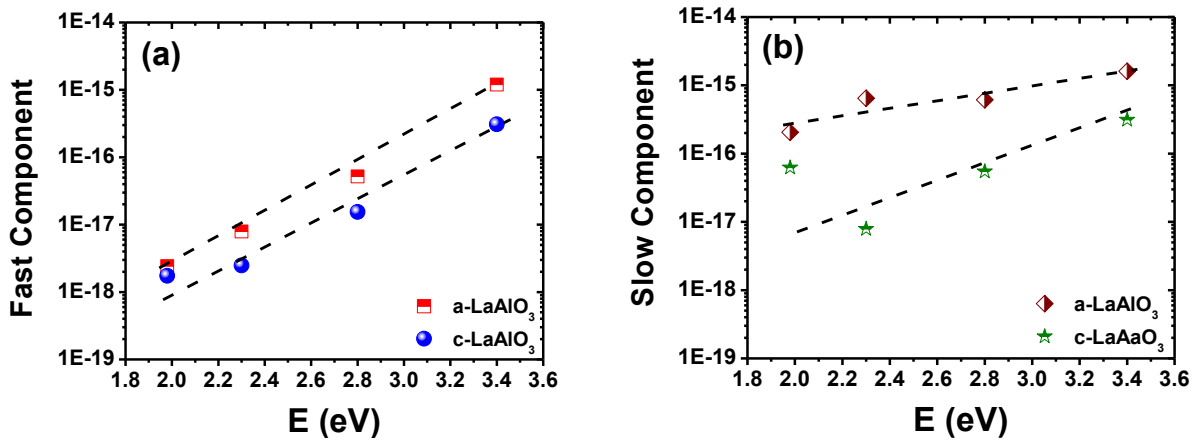

Figure 2.10 (a) fast component and (b) slow component of photoresponse vs. energy for amorphous and crystalline $LaAlO_3/SrTiO_3$ samples collected at photon flux $\Phi = 4\times 10^{14}$ s^{-1} cm^{-2}. Dash lines are guides for the eye.

Table 2.2 fitting parameters for the four different illumination wavelengths

sample	λ (nm)	σ_∞ (μS)	A	τ_1 (s)	τ_2 (s)
c-$LaAlO_3$	625	2.45	0.03	73	18287
	540	0.40	0.24	36	430
	445	2.79	0.22	33	1384
	365	24.6	0.49	0.4	594
a- $LaAlO_3$	625	7.02	0.011	163	7970
	540	21.3	0.012	143	3797
	445	22.5	0.078	71	439
	365	102	0.425	0.2	513
c-$LaGaO_3$	625	0.004	0.01	0.35	31
	540	0.079	0.06	97	4212
	445	6.48	0.03	94	3550
	365	27.8	0.45	0.6	1344

2.8 Discussion

The slow dynamics of recovery after light has been turned off is ascribed to the persistent nature of photoconductivity in $LaAlO_3/SrTiO_3$ and related interfaces, and attributed to the spatial separation of the electron-hole pair under the effect of the local electric field [2, 64, 94]. This phenomenon was characterized in previous works [2, 87] and will not be discussed here. Therefore, the discussion is confined to the raise of photoconductivity after the light is turned on.

In principle, both the variation of mobility and of carrier number can contribute to the change of conductivity. However, the mobility is only marginally affected and this effect will be considered as negligible. Therefore, it will be assumed that the simple relation holds: $\frac{\sigma_\infty}{\sigma_o} = \frac{n_\infty}{n_o}$

To discuss the basis for the linear and saturated photoresponse (described in section 2.6), consider for simplicity that a single channel of promotion and recombination is at play. Figure 2.11 shows a photon of energy hν exciting one defect states and promoting an electron to the conduction band (CB). After a characteristic time, the excited state decays along some path (that can also be very complex, but that will not be discussed here).

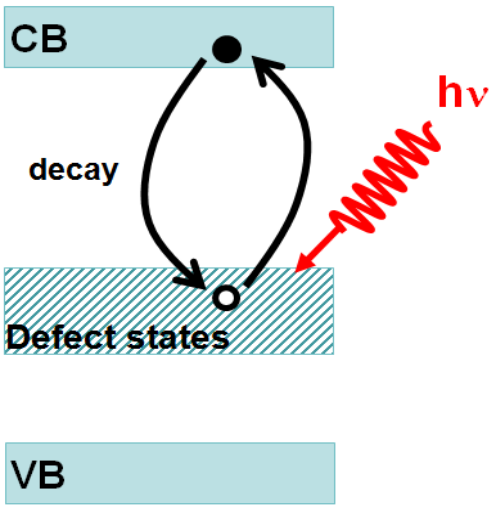

Figure 2.11 The promotion and recombination of electrons from defect states when exited by photon of energy hν.

Be N_o the total number of defects and p are the number of holes left after excitation. The rate equation can be read as

$$\frac{\partial n}{\partial t} = \alpha_o \, \Phi \left(N_o - p \right) - \frac{p}{\tau}$$

the last term in equation account for the recombination rate with some characteristic time τ . In the steady state, the rate of recombination is equal to the rate of excitation i.e. dp/dt=0, leading to the following expression:

$$p = \frac{\alpha_o \, \Phi \, N_o}{\alpha_o \, \Phi + \gamma}$$

where $\gamma = \tau^{-1}$. In the low photon flux regime $p \propto \Phi$, i.e. the response is linear. On the other hand, if $\alpha_o \, \Phi >> \gamma$, the equation point to a constant value N_o, independently from photon flux.

The naïve 1-channel model thus allows to understand the mechanism of saturation, but it is of course too rude to allow a satisfactory description of the dynamics. The simplest model to explain the results is reported in Figure 2.12. The right panel (Figure 2.12 a) shows the diagrams for crystalline samples [64, 95]; the left panel (Figure 2.12 b) describes instead amorphous samples.

As explained in section 1.6.1 of chapter 1, the right sides of the band diagrams for crystalline and amorphous heterostructures are deeply different the one from each other. For crystalline heterostructures, according to the standard electron reconstruction model, the bands of overlayer are bent upwards by the macroscopic electric field. The upturn of the bands is so sharp, that the valance band edge is already lifted by a fraction of eV close to the interface. On the other hand, all the valance band edge states of the overlayer share the same energy in amorphous structures. Nevertheless, defect states that extend very much within the gap of the overlayer may be very important in amorphous structures [59].

Both for crystalline and amorphous structures, the quantum well that is formed at the interface within $SrTiO_3$, confine the mobile electrons in the 2DEG. The point defects, which is mainly

identify with oxygen vacancies, add to the bands a distribution of trap states, forming a broad in-gap band. Such states are mainly localized in a region close to the interface. The in-gap states are very crucial for analyzing photoresponse for photon energy smaller than the $SrTiO_3$ gap. Due to the different fabrication procedure, the density of vacancies is expected to be higher in amorphous samples.

There could be many possibilities for photo-promotion dynamics but for simplicity only two channels are considered. These are denoted as "sc" (slow channel) or "fc" (fast channel) to indicate slow and fast dynamics, respectively. The main channel of fast excitation is a direct promotion from the valance band on the $SrTiO_3$ side to the conduction band. The slow process is here identified with the promotion of electrons from the donor states overlayer side the conduction band of $SrTiO_3$. The oxygen vacancies in amorphous interfaces and the overlayer band bending in crystalline structures reduced the optical gap respectively.

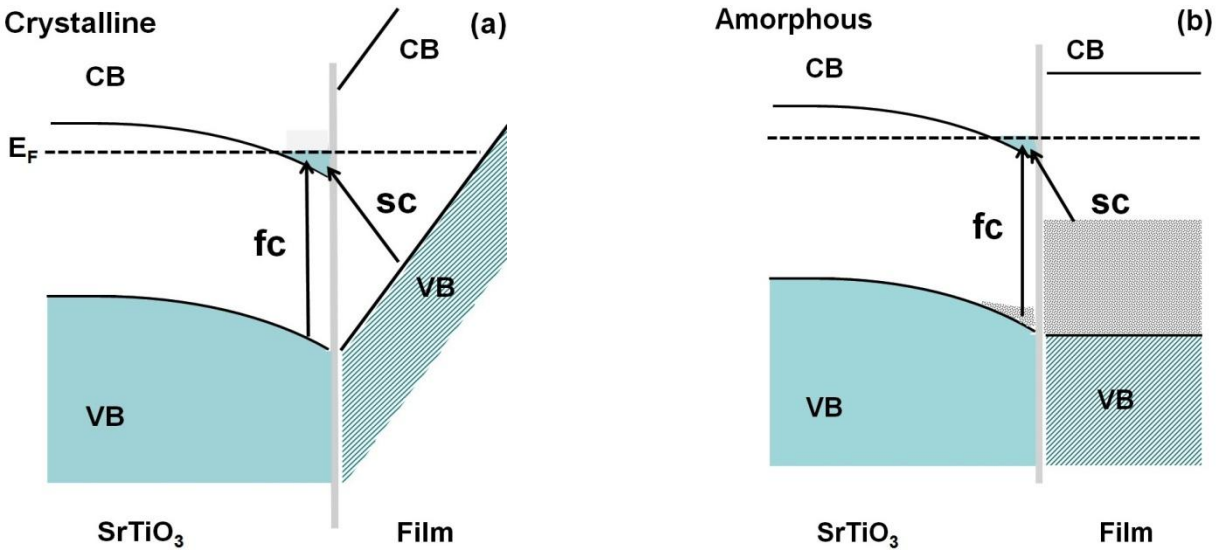

Figure 2.12 Schematic of the band structure of a) crystalline and b) amorphous. The grey dotted region represents the band of in-gap states. The slow (sc) and fast channels (fc) of photogeneration are represented by arrows.

In order to discuss the relation between the sketches (Figure 2.12) and the fitting function (equation 2.1) integrated density of states of the full interface region is introduced in Figure 2.13. Consider a generic scenario that takes into account, along with the valance band (VB), the presence of in-trap states and two characteristic times. Mainly, the idea is that two separate channels of excitation contribute simultaneously (Figure 2.13 a). The promotion rate of each channel is proportional to the flux of impinging photons Φ (measured in s^{-1} cm^{-2}) and to the quantum efficiency of photoemission, that is "α", ("β") for the first (second) channel. The channel 1 is the direct excitation from $SrTiO_3$ VB to the conduction band (CB). Each excitation leaves a hole in the VB and the number of such holes is "p". Let "P" be the total number of states that can be excited by a photon with energy E. The channel 2 is the excitation from a reservoir of trap states. Each excitation leaves an empty trap state and the number of such states is "q". At each photon energy, only the states that are close enough to the CB can be excited. Let "Q" be the total number of states that can be excited at energy E.

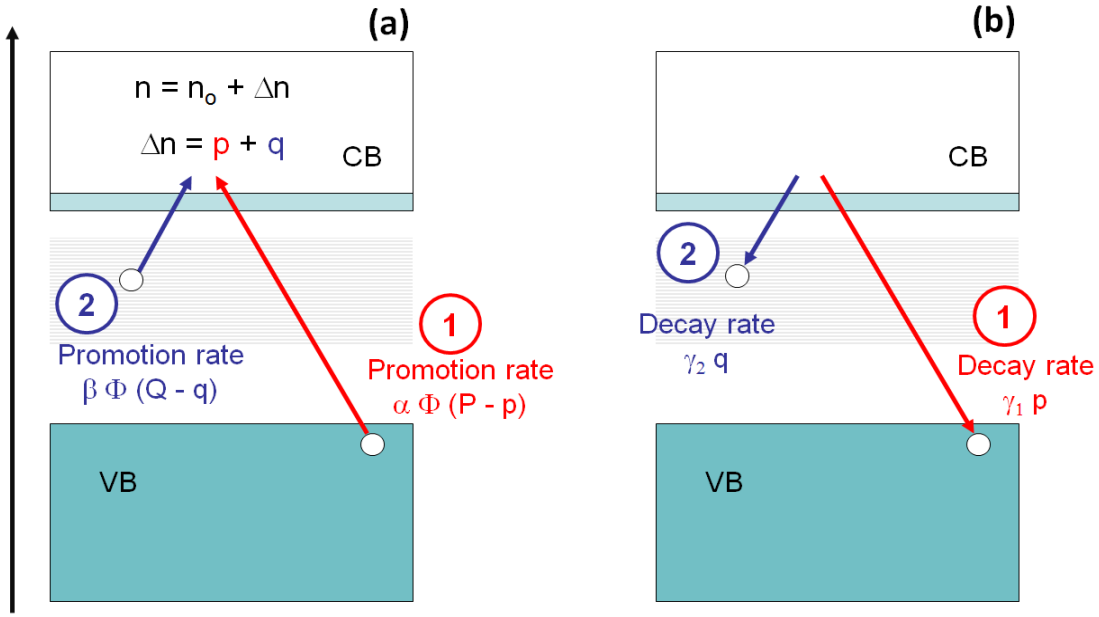

Figure 2.13 Schematic of two independent channels that contribute at the same time (a) promotion of electrons in the valence band (red arrow) and the defect states in the gap (blue arrow) (b) recombination process in the valence band (red arrow) and the defect states in the gap (blue arrow).

Now consider the reverse processes of recombination (Figure 2.13 b). Each such process is proportional to the number of empty states in the recombination band, which is “p” and “q”, respectively. Furthermore, it is proportional to the total number of electrons in the CB.

The rate equation which takes into account the promotion and recombination processes for both channels read:

$$\frac{dp}{dt} = \alpha\,\Phi\,(P - p) - \Gamma_1 np \qquad\qquad \frac{dq}{dt} = \alpha\,\Phi\,(Q - q) - \Gamma_2 nq$$

The total number of excited electrons is $\Delta n = p + q$, hence the total number of electrons in CB is $n = n_o + \Delta n$, where n_o is the equilibrium sheet carrier density. However, when conducting samples are considered, the CB already contains many electrons before the excitation.

$$\Delta n << n_o \;\Rightarrow\; n \approx n_o$$

Furthermore, in the linear regime the following assumptions hold

$$p << P \;\Rightarrow\; (P - p) \approx P$$

$$q << Q \;\Rightarrow\; (Q - q) \approx Q$$

Asserting the above discussion, the following rate equations are given for the first and the second channel.

$$\frac{dq}{dt} = \beta\,\Phi\,Q - \frac{q}{\tau_2} \qquad\qquad \frac{dp}{dt} = \alpha\,\Phi\,P - \frac{p}{\tau_1}$$

The solution of above equations has exponential of the form $p = p_o\left[1 - exp(-t/\tau_1)\right]$ and $q = q_o\left[1 - exp(-t/\tau_2)\right]$, yielding

$$\Delta n = p_o\left[1 - exp(-t/\tau_1)\right] + q_o\left[1 - exp(-t/\tau_2)\right] \qquad 2.2$$

Equation 2.2 gives a basis for the fitting function (equation 2.1) used to analyze the photoresponse.

Comparison with data

The outcome of the model can be compared with the data. In crystalline structure, the excitation by low energy photons is a slow process that promotes electrons to the quantum well from the overlayer VB; the fast process, instead, is accomplished by high energy photons, from the $SrTiO_3$ VB states (Figure 2.9 and 2.12 a). This observation is consistent with Ref. [64]. For the set of amorphous samples investigated in this work still the excitation by low energy photons is a slow process, promoting to the quantum well electrons from the overlayer VB and the fast process requires high energy photons (Figure 2.9 and 2.12 b). The latter case of amorphous structure assumed that the in-gap states in overlayer side are at higher energy than in $SrTiO_3$ side (Figure 2.12 b). This is the reason why the "sc" is dominated by low energy photons. Furthermore as described in section 2.7, the fast component exhibits more vibrant trend while the slow component shows strong variability from sample to sample. The latter is mainly attributed to the defect states in a given sample. It is known that depending on the growth conditions, the distribution of defects can be greatly changed in samples [60]. This explains why the slow component shows a more variated behavior in different samples.

It was shown in Figure 2.9 that the photoresponse behavior grows exponentially with increasing energy of the incident radiation up to the direct band gap of $SrTiO_3$. In order to discuss this behavior, the following toy model is presented.

Consider the Figure 2.14 which shows the density of states (DOS) verses energy profile for $SrTiO_3$. E_v and E_c are the valance and conduction band edges that are separated by direct band-gap, Δ (~3.6 eV). Arbitrarily, $E_v = 0$ is assumed. The recent photoemissions spectroscopy measurements [96] reveal that, unlike conduction band, the valance band is not sharp i.e. it has a tail that extends exponentially in the band gap (Figure 2.14). This exponential profile emerges because of the in-gap states that are particularly relevant in photoconductivity. The present model also takes into account this tail. The final results of the model are discussed.

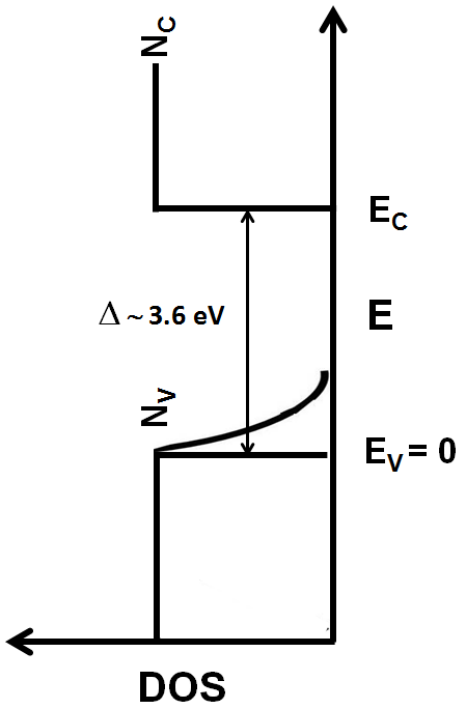

Figure 2.14 Density of states (DOS) vs. energy profile of c-$LaAlO_3$/$SrTiO_3$, Δ is the direct band-gap of $SrTiO_3$

Mainly the following two cases can be considered;

1) In case the energy of incident photon is smaller than the gap i.e. $\Delta - h\upsilon > 0 \Rightarrow \Delta > h\upsilon$, the transition involves initial state in the exponential tail then $\Gamma_{i\to f} \propto \exp\left(h\upsilon/\varepsilon_c\right)$, where ε_c is a characteristic energy. This expression anticipates that the signal will grow exponentially as a function of incident photon energy.
2) In case the photon energy is greater than the gap i.e. $\Delta - h\upsilon < 0 \Rightarrow \Delta < h\upsilon$, the optical rate is $\Gamma_{i\to f} \propto h\upsilon$.

The solid lines (Figure 2.15) based on this model describes in a reasonable way the experimental data.

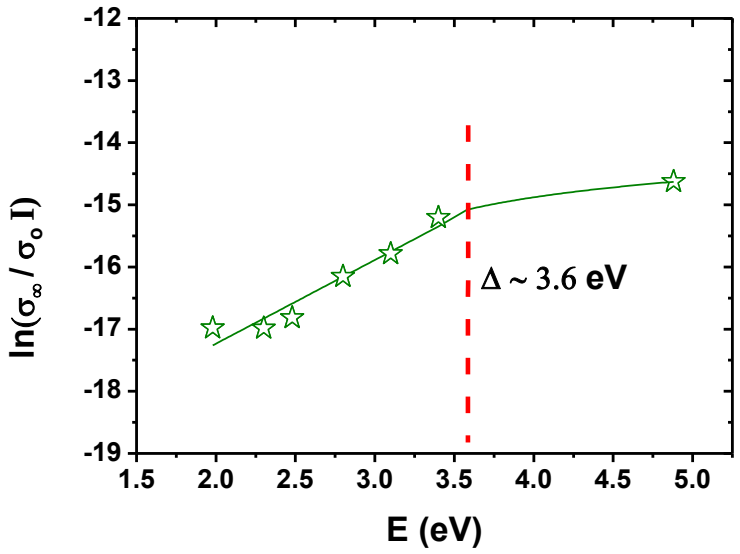

Figure 2.15 Photoresponse vs. energy for c-$LaAlO_3/SrTiO_3$ collect at photon flux $\Phi = 4\times 10^{14}$ s^{-1} cm^{-2}. The solid lines are fit curves according to the model, dotted line indicates, Δ, the direct band-gap of $SrTiO_3$.

3.9 Summary

In summary, this chapter presented the time-resolved photoconductance of amorphous and crystalline $LaAlO_3/SrTiO_3$, and other similar interfaces irradiated by light of wavelengths in the range 365-625 nm. Both kind of interfaces exhibit a photoconductance that is persistent in nature. The experimental results show that both for the crystalline and amorphous interfaces, the photoresponse increases exponentially with incident photon energy up to the direct gap of $SrTiO_3$.

Chapter 3

Transport Properties of Oxide Interfaces under the Effect of Electric Field and Light

Abstract

Chapter 3 presents the transport properties of different oxide heterointerfaces under the effect of the electric field, and under the combined effect of light in the VIS-UV range and electric field. The low temperature gate cycles show strong hysteretic behavior. A model is introduced to calculate the charge density modulated by the electric field.

3.1 Experimental Setup

The electrical transport measurements under the electric field effect were performed in the temperature range 10-300 K in dark condition in a closed cycle refrigerator. The resistance of the samples was measured by standard van der Pauw method. A three terminal devices were realized by placing a metallic sheet on the back of the substrate (back gate configuration). To this aim, a silver paste film was used. The two-dimensional electron gas (2DEG) acts as a channel modulated by the gate voltage (V_G). In the most experiments, the gate potential was applied by using a Keithley picoammeter 6487 as schematically shown in Figure 3.1. According to Figure 3.1, for a positive gate voltage the interface is negatively charged and for negative gate voltages it is positively charged. The resistance of the 2DEG was determined by injecting 10 μA current. In all the cases, the gate current (<10 nA) was much lower than the channel current, 10 μA.

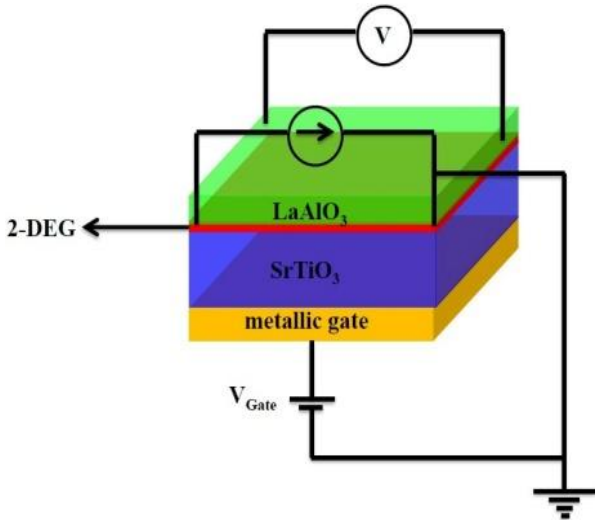

Figure 3.1 Schematic of gated $LaAlO_3/SrTiO_3$ with silver paste as a metallic back gate.

3.2 Transport Properties of Interfaces

In this chapter the transport properties of different samples under the effect of gate voltages are presented. These samples include "standard" (001) oriented $LaAlO_3/SrTiO_3$ and an amorphous $LaGaO_3/SrTiO_3$ samples.

Figure 3.2 shows a comparison of R_{sheet} (T) curves for some of the investigated samples. All the samples showed metallic behavior down to low temperature. Nevertheless, their transport parameters show a large variation. The room temperature sheet resistance ranges between 10 and 68 kΩ/□. The sheet carrier density, as determined by Hall effect measurements, ranges between ~ 2.06×10^{13} and ~1.10×10^{14} cm^{-2}. The resistive ratio R_{290K}/R_{10K} ranges between 18 and 168. A summary including growth conditions, thickness and transport properties of the samples is reported in Table 3.1.

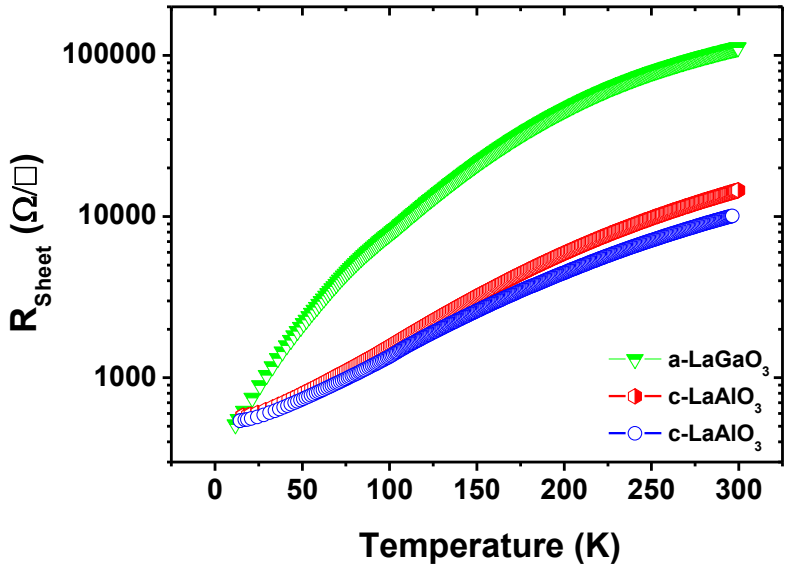

Figure 3.2 R_{sheet} (T) curves for crystalline $LaAlO_3/SrTiO_3$ and amorphous $LaGaO_3/SrTiO_3$.

Table 3.1: Summary of the fabrication and room temperature transport properties of some samples investigated in this study

System	***Thickness (nm)***	***PO_2 (mbar)***	***R_{Sheet} (kΩ/□)***	***R_{290K}/R_{10K}***	***n (cm^{-2})***
c-$LaAaO_3/SrTiO_3$	4	1×10^{-3}	10	18	1.10×10^{14}
c-$LaAlO_3/SrTiO_3$	4	1×10^{-2}	14	25	8.20×10^{13}
a-$LaGaO_3/SrTiO_3$	4	1×10^{-2}	68	168	2.06×10^{13}

3.3 Scope of Electric Field Effect

The back gated $LaAlO_3/SrTiO_3$ (Figure 3.1) can be compared to conventional field effect device, e.g. a MOSFET. In a conventional MOSFET device, SiO_2 is employed as (dielectric) barrier between the channel and the gate. The barrier height is about 3.2 eV. Typical electric fields in the nm-thick barrier can exceed 10^8 V/m. The loss current through the barrier is mainly due to tunnelling effect [74], and it is very low.

In a back-gated oxide 2DEG, the situation is largely different. Direct tunnelling to the back-gate is impossible due to the thickness of the barrier (0.5 mm). Only low fields of the order of 10^3 V/m are applied. The back-gate metal/$SrTiO_3$ interface is characterized by an energy difference between the Fermi level of the metallic electrode and the $SrTiO_3$ conduction band and is typically of the order of 1eV (Figure 3.3) [97].The interface bending of the $SrTiO_3$ conduction band below the Fermi level virtually defines a border. The barrier height on the 2DEG side is extremely low and can be estimated of the order of 10^{-1} eV [72].

The application of a back-gate voltage can largely modify the energy landscape in the proximity of the 2DEG, both because of the Fermi level tuning and because of changes of the conduction band profile, and thus of the quantum well profile.

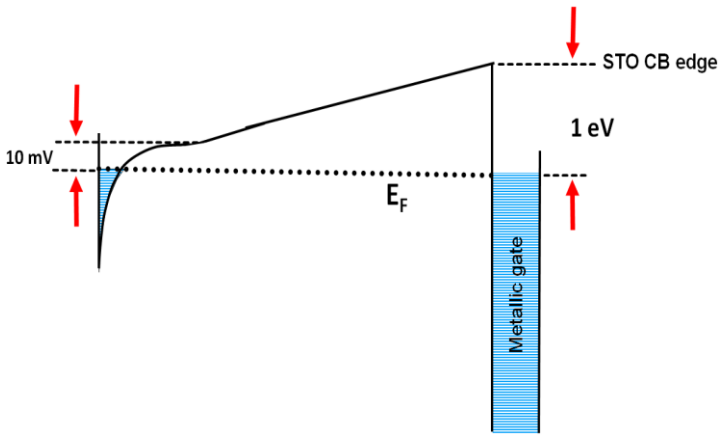

Figure 3.3 Energy band diagram for gated oxide interface. At $V_G = 0$ the Fermi levels are aligned. Due to the difference between the conduction band (CB) edge level on both sides, a band bending of $SrTiO_3$ results.

In our experimental configuration the 2DEG is grounded. The chemical potential of the 2DEG and the gate are identical at zero gate bias (Figure 4.3 b). At $V_G > 0$, the Fermi level of gate and the bottom of the well goes down (Figure 3.4 a). This is due to the charge transfer to the quantum well by the external generator hence the resistance of the system is expected decrease. On the contrary, in the case of negative gate voltage the carriers are removed from the quantum well because the Fermi level moves up (Figure 3.4 c) and an increase in resistance is expected.

This situation is largely similar to that of a simple parallel plate capacitor separated by a dielectric material. Depending on the direction of the polarity, one plate of the capacitor is charged or discharged. The amount of charge, $e\Delta n$ (Δn is the variation in sheet carrier density), that is transfer by the voltage (V) is given by the expression

$$e\Delta n = \varepsilon_o \varepsilon_r E = \varepsilon_o \varepsilon_r V/d$$

where ε_o is the permittivity of the free space and ε_r is relative permittivity (dielectric constant) of the dielectric layer of thickness *d*. Note that if the mobility remains fixed, then the added (subtracted) charge to the plate/channel will decrease (increase) the resistance. At constant bias, the amount of charge scales with the dielectric constant. It is well known that the dielectric constant of $SrTiO_3$ is strongly temperature depends [27]; it increases from ~ 300 at room temperature to ~ 24000 at 4 K (see section 1.4.4 in chapter 1). This dependence anticipates that at fixed V_G a larger variation in resistance will occur at low temperature in comparison to room temperature.

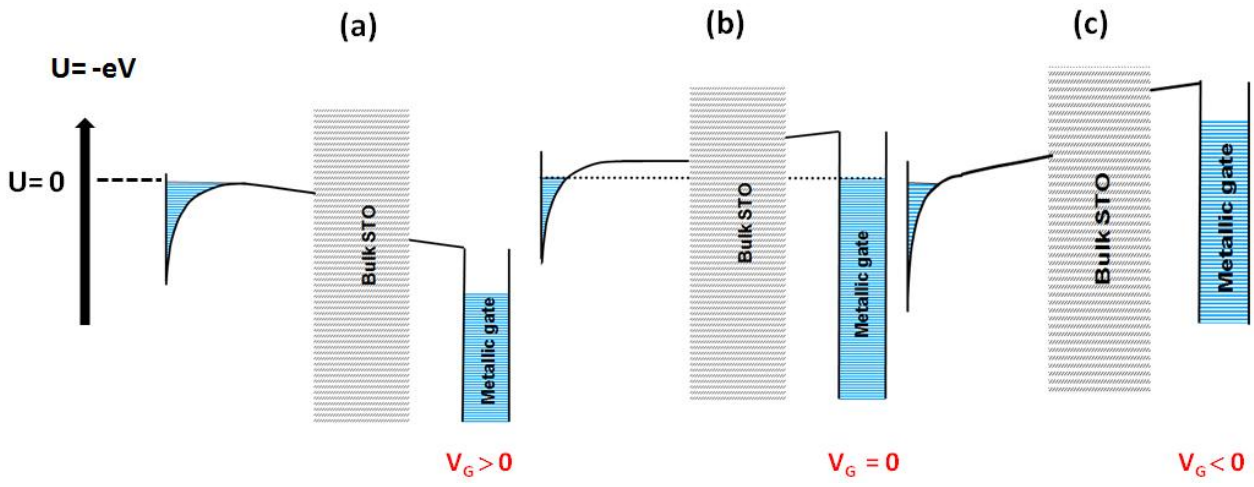

Figure 3.4 Energy band diagram for back-gated oxide interface with Fermi level at U = 0, for (a) accumulation mode, $V_G > 0$ (b) equilibrium, $V_G = 0$ and (c) depletion mode, $V_G < 0$. Note that gray part is so thick that the barrier shape is not (strictly) represented.

3.4 The Effect of Temperature

Figure 3.5 (a,b) compares the change in sheet resistance for 4 nm thick c-$LaAlO_3$/$SrTiO_3$ as function of gate voltage (V_G) at low (10 K) and room temperatures. The gate voltage between 0 and ± 200 V (ΔE = 4 kV/cm) for one minute each step was applied as shown in the lower panel of Figure 3.5 (a,b). The samples response is basically characterized by the variation in sheet resistance as function of V_G. The sheet resistance decrease from ~ 15 to 4.8 kΩ/□ in the enhancement mode (+200 V) (Figure 3.5 a). On the other hand, in the carrier depletion mode (-200 V) it increase from ~ 15 to 15.2 kΩ/□. The total variation in sheet resistance at room temperature ($\Delta R_{\pm 200V}$) with respect to R_o (V_G = 0) is ~ 2.5 %. At 10 K (Figure 3.5 b) this variation is more than 100 % for the same gate potential due to high dielectric constant of $SrTiO_3$ at low 10 K.

It is worthwhile noting that the field effect modulation at room temperature exhibits quite conventional behavior, there is no hysteresis corresponding to $V_G = 0$ (which is present at low temperature, see section 3.5). Furthermore, the first positive polarization (FPP) at low temperatures persistently changes the sheet resistance of the samples, as discussed at length in chapter 4. In this section the attention is confined to the behavior that is observed after few starting cycles and that repeats always identically by further cycling.

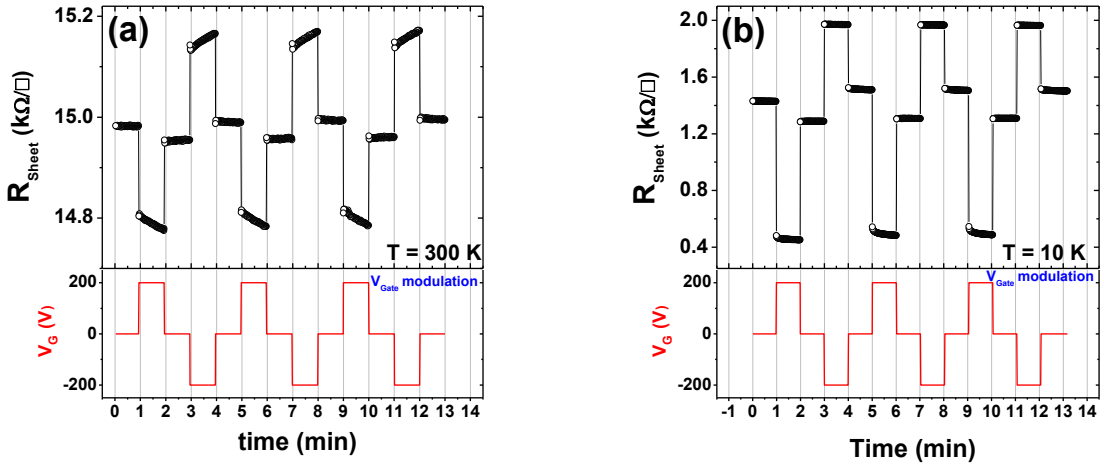

Figure 3.5 Comparison of variation in sheet resistance in c-$LaAlO_3$/$SrTiO_3$ as function of gate bias at (a) 300 K (b) 10 K.

At room temperature the samples response to the gate voltage was also tested on the long time scale of hour. For example, Figure 3.6 shows the behavior of the sheet resistance as a function of time, while the gate voltage is changed. Initially the gate voltage is off and sheet resistance stays nearly constant around 50 kΩ/□. By applying V_G = +200 V the sheet resistance drops to 31.3 kΩ/□ over 60 minutes. After switching off V_G the sample sheet resistance during 60 minutes increases only to 33.7 kΩ/□ and do not restored to its initial state showing some memory effect (see section 3.7 for discussion). By applying the opposite polarity (V_G = -200 V) charge carriers are effectively withdrawn from the interface and the sheet resistance increases anomalously to 577 kΩ/□ in less than an hour exhibiting a high resistive state. At this point the sheet resistances

reached to the instrumental compliance limit. It is expected that the +200 V can bring it back to low resistive state.

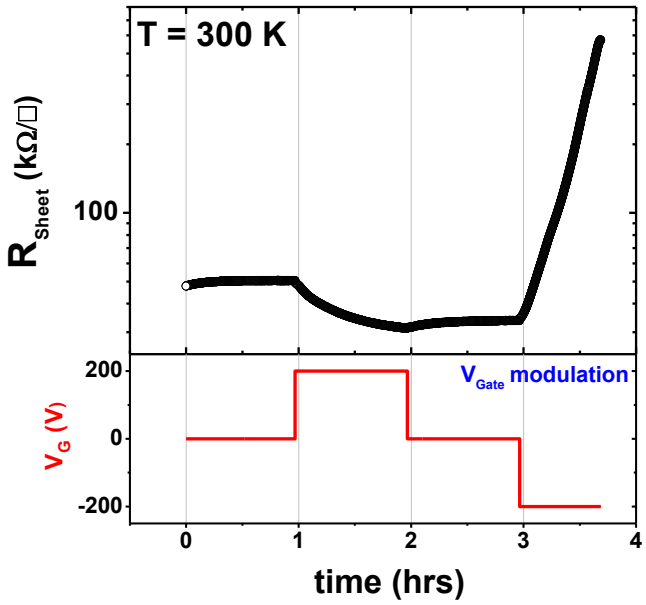

Figure 3.6 Sheet resistance variations as function of gate modulation for c-$LaAlO_3$/$SrTiO_3$ at room temperature on long time scale.

R_{sheet}-T curves under different gate biases on many samples were also collected. Figure 3.7 shows the R_{sheet}-T plots for 4 nm thick c-LAO/STO collected in 0 and ± 200 V gate bias. As expected, up to 100 K the dielectric constant of $SrTiO_3$ increase marginally, the variation in sheet resistance for +200 and -200 V are largely indistinguishable from zero bias curve. Below 100 K in enhancement mode (+200 V) the sheet resistance dropped more quickly than unbiased mode. Similarly for -200 V there is conductivity lose by a factor one with respect to zero bias curve.

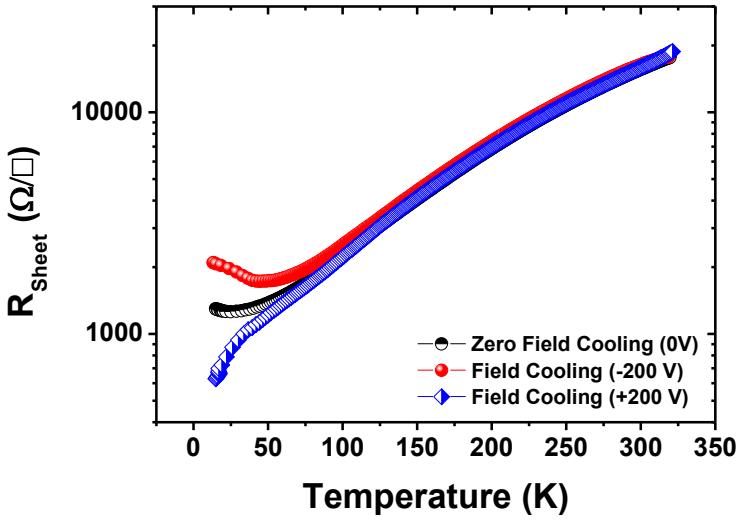

Figure 3.7 R_{sheet}-T cooling plots for c-$LaAlO_3$/$SrTiO_3$ at fixed V_G = 0, +200 and -200 V.

3.5 Hysteretic Behavior

In the gate bias measurements especially at low temperatures, the resistance exhibits hysteretic behavior. The hysteretic behavior arises from the difference in the resistance at $V_G = 0$ after each positive and subsequent negative gate pulse. Figure 3.8 (a,b) shows a typical hysteretic behavior, it compares the normalized change in resistance ($\Delta R/ R_o$, where R_o is the initial resistance at $V_G = 0$) as function of gate bias for c-$LaAlO_3$/$SrTiO_3$ at two different temperatures, 10 and 100 K. The gate bias was applied in sequence 0, +200V, 0, -200V, 0. The resistance mismatch at $V_G = 0$ after positive and negative gate pulse, parameterized by $\delta R/ R_o$, is more than 14 % (indicated by *double*-headed *arrow in* Figure 3.8 a). The magnitude of the hysteretic behavior become smaller with increase in temperature, it reduces to < 1 % at 100 K (Figure 3.8 b).

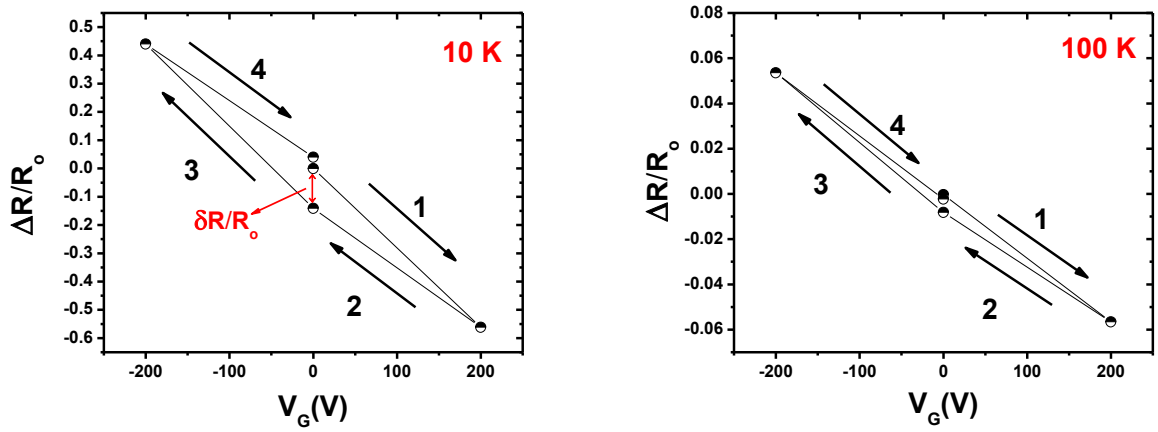

Figure 3.8 V_G modulation of normalized resistance at (a) 10 K (b) 100 K showing hysteretic behavior, the arrows and numbers indicates the order in which the gate bias was applied. Solid lines are guides for the eye.

To further clarify the hysteretic behavior the data for the same temperatures are plotted in different scheme where the change in resistance is recorded as a function of gate modulation (Figure 3.9 a,b). The resistance of the sample stays higher than the previous $V_G = 0$ after the depletion mode (-200 V) as enclosed by the cycle (Figure 3.9 a). On the other hand after the enhancement mode (+200 V) the resistance stays lower. The same observation comparatively smaller in magnitude was observed for 100 K (Figure 3.9 b).

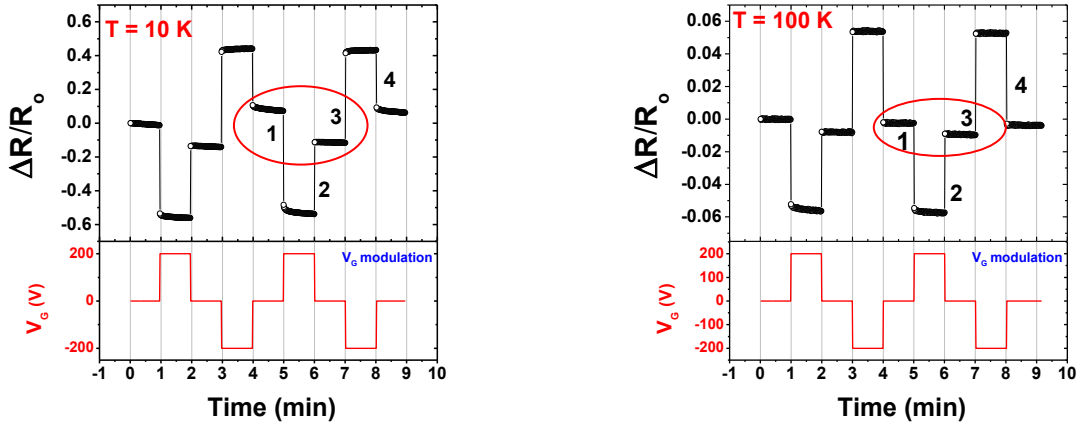

Figure 3.9 Hysteretic behavior corresponds to $V_G = 0$ indicated by circle at (a) 10 K (b) 100 K, The numbers refer to Figure 3.8.

Since the response after positive or negative is not very flat but shows some transient behavior, one may suspect that the time allowed was not enough to relax the system. To examine this possibility, the measurements on relatively long time scale were also performed but still the hysteretic value $\delta R/ R_o$ remains. As an example, Figure 3.10 (a) shows the gate modulated resistance at 105 K after waiting 15 minutes each step. It is clear that on the time scale of minutes, the difference in resistance at $V_G = 0$, which is parameterized by $\delta R/ R_o$, is still present (Figure 3.10 b). The same was also checked at low temperature (12 K), where the transient response was found to be faster, and still a giant hysteretic behavior was demonstrated. From Figure 3.9, it is clear that $\delta R/ R_o$ do not scale with $\Delta R/ R_o$, this suggests that we are not trivially observing the effect of ε_r vs. temperature.

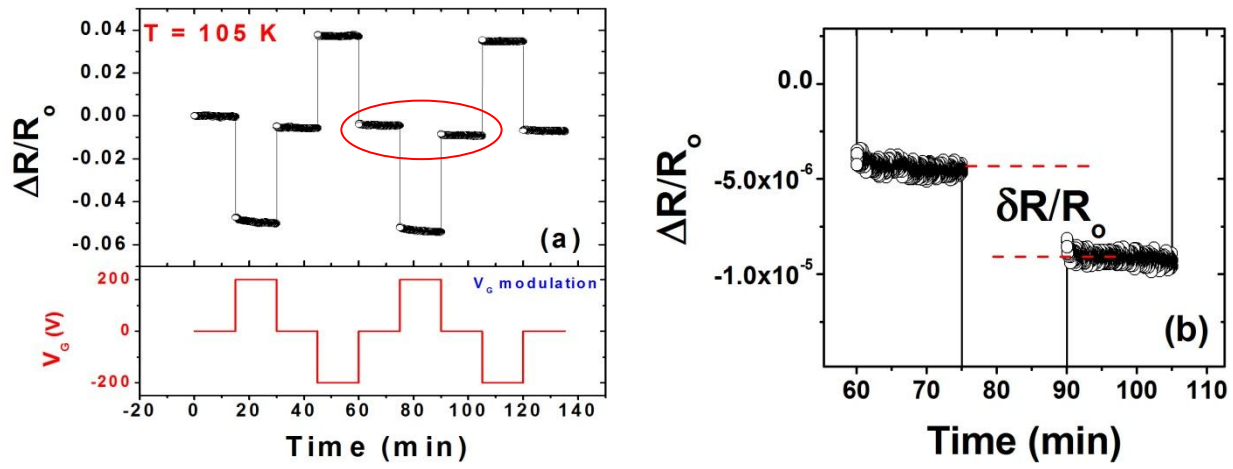

Figure 3.10 (a) Hysteretic behavior corresponds to $V_G = 0$ at 105 K on time scale of 15 minutes, enlarge view of the hysteretic behavior (quantified by $\delta R/ R_o$).

The hysteretic behavior as a function of temperature was thoroughly investigated. The samples were first cooling down to 10 K then the gate voltage measurements at different temperatures during the heating from 20 to 240 K were collected. Measurements during the cooling from 240 to 20 K were also performed. This was done by first cooling the sample down to 10 K, then performing the gate voltage step at 20 K to irreversible change the state of the sample (see chapter 4, section 4.1). The samples were then heated to 300 K. Finally, the gate cycle

measurements were collected while cooling from 240 to 20 K. The extracted data for the hysteretic behavior as a function of temperature during cooling and heating is depicted in Figure 3.11.

Quantitatively, the hysteretic behavior is high in the low temperature regime, it is really significant only for T < 70 K but then sharply drops for T > 70 K. It is important to note that a minute hysteretic behavior still exists at 240 K (i.e. $\delta R/ R_o \neq 0$). In the temperature range 25-50 K the value of $\delta R/ R_o$ changes depending whether the measurements were collected during cooling (from 240 to 20 K) or during heating (from 20 to 240 K). This is indicated by the arrow in Figures 3.11.

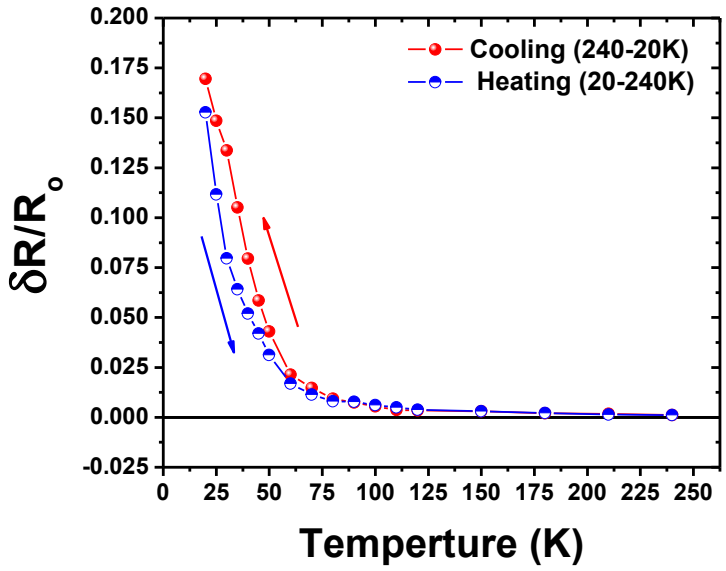

Figure 3.11 Hysterical behavior, which is parameterized by $\delta R/ R_o$, as a function of temperature during cooling and heating for c-$LaAlO_3$/$SrTiO_3$. Solid lines are guides for the eye.

3.6 Carrier's Density Estimation

Figure 3.12 (a,b) shows the change in sheet conductance ($\Delta\sigma$) at 10 and 100 K when the gate bias is sweep between 0 and ± 200 V in steps of 20 V. In such measurements, V_G is kept constant at each step value for Δt = 20 s.

As already described in section 3.3, the gated $LaAlO_3/SrTiO_3$ in the steady state works like a parallel plate capacitor with dielectric insulator between them. The areal charge density ($e\Delta n$), that is induced at a given gate voltage V_G applied across an insulator of thickness d (0.5 mm for $SrTiO_3$ in the present study) is given by

$$e\Delta n = \int_0^{V_G} \varepsilon_o \varepsilon_r \frac{V}{d}.dV \qquad 3.1$$

where ε_o is the permittivity of the free space and ε_r is relative permittivity. The above equation also takes into account the dependence of ε_r on temperature and strength of electric field. Once Δn is computed, it is possible to plot $\Delta\sigma$ vs. Δn (Figure 3.12 c,d). At 90 K, the curve is almost linear with electron density Δn in the range ~ 3×10^{12} to -3×10^{12} cm^{-2} for V_G sweep from +200 to -200 V (Figure 3.12 c). At 10 K, at the same strength of electric field, due to high dielectric constant at low temperature, the density increases by one order of magnitude. Furthermore, the plot at 10 K is highly non-linear and is characterized by two slopes (Figure 3.12 d). These distant slopes have physical meaning in terms of band filling and are discussed in section 3.7.

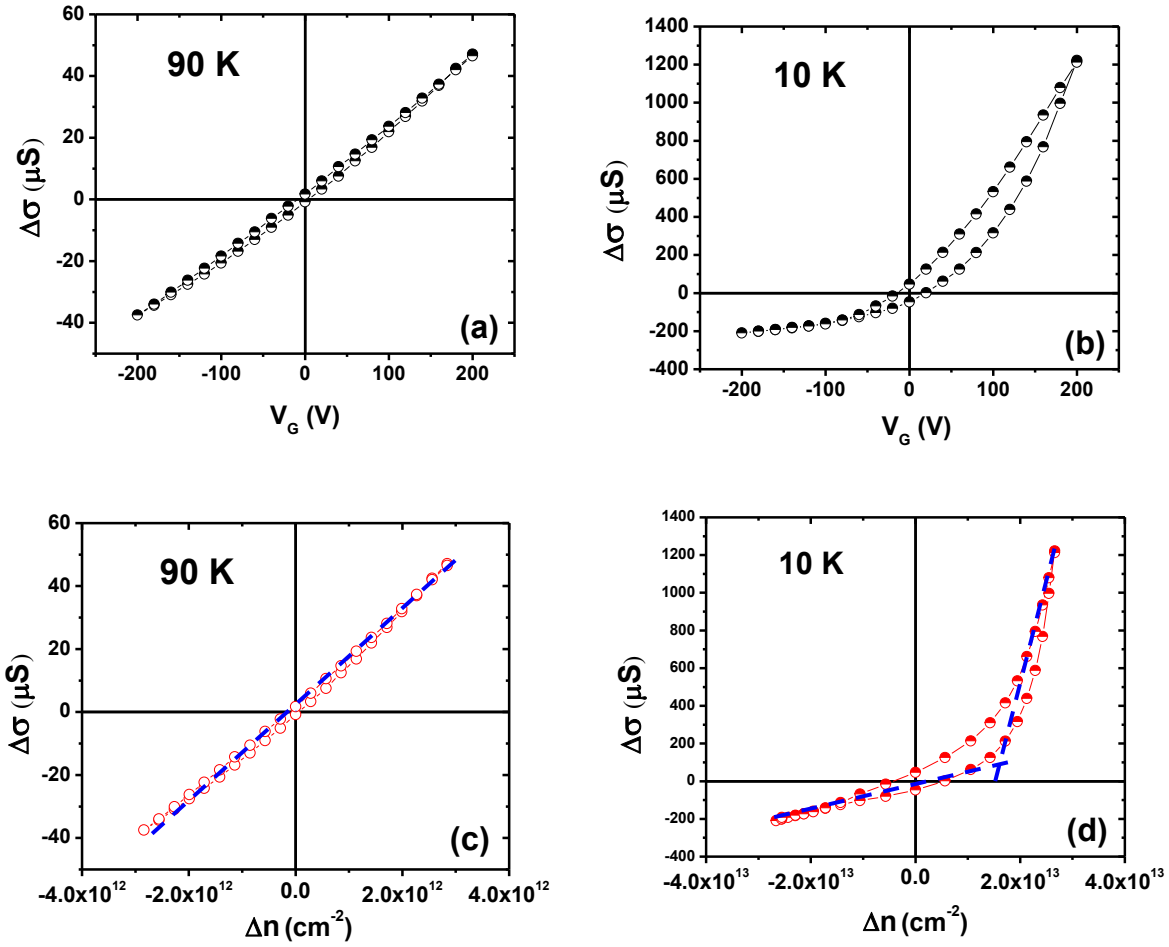

Figure 3.12 Sheet conductivity change for c-$LaAlO_3/SrTiO_3$ as a function of gate modulation at (a) 90 K (b) 10 K. Estimated field induced sheet carrier density at (c) 90 K (d) 10 K, the blue dotted line shows different slopes. Solid lines are guides for the eye.

3.7 Discussion

The (same) memory effect and resistive switching described in section 3.4 (Figure 3.6) were previously reported for crystalline $LaAlO_3/SrTiO_3$ [98] and amorphous $LaAlO_3/SrTiO_3$ [99]. These behaviors in the interfaces at room temperature can be possibly ascribed to two reasons, i) electromigration of oxygen vacancies [100] or ii) trapping and de-trapping of electrons in $SrTiO_3$ [101].

In the case of electromigration of oxygen vacancies, a positive back-gate potential attracts the negatively charged oxygen-ions and gathers oxygen vacancies at the interface. These vacancies

change the electrical properties of the interface exhibiting a low resistive state. On the contrary, a high resistive state occurs at negative gate bias [99].

In the latter case, vacant trapping states limit the electronic flow and lead to high resistive states. Accumulation of electrons at the interface occurs at a positive back-gate potential which fills the trapping states and the samples exhibit low resistive state. Upon removal of the field the de-trapping of electrons occurs very slowly. This effect is reminiscent of memory-behavior [98].

No memory behavior was seen [98] when $LaAlO_3$ was employed as a gate dielectric in top gate experiments thus pointing that $SrTiO_3$ plays a significant role.

The change in sheet conductance vs. field induced sheet carriers density (Figure 3.12) can be understood in the frame of the Drude model. The mobility can be defined as the slop of sheet conductance vs. sheet charge density:

$$\mu = \frac{1}{e}\frac{\partial \sigma}{\partial n} \qquad 3.2$$

The constant slope at 90 K (Figure 3.12 c) implies that all the carriers share the same mobility, quantitatively estimated by equation 3.2 as ~ 75 $cm^2\ V^{-1}s^{-1}$. At 10 K, instead, we find that the carriers posses two different mobilities, depending on the filling of th quantum well. In Figure 3.12 (d), the slop in the depletion mode correspond to $\mu \sim 60\ cm^2\ V^{-1}s^{-1}$ while in the enrichment mode it is about 10 times more, i.e. 600 $cm^2\ V^{-1}s^{-1}$.

The different mobilities can be understood in terms of E-K diagram as depicted in Figure 3.13. It is well established that interfacial electrons reside in the t_{2g} conduction bands of $SrTiO_3$ [21]. In the bulk, the bands are degenerate (see section 1.4.3, chapter 1). At the interface this degeneracy is lifted due to tetragonal distortion. The interface crystal field splits the t_{2g} states in a lower d_{xy} singlet, and an upper d_{xz}, d_{yz} doublet energy bands (Figure 3.13). The d_{xy} reside at or in the immediate proximity of the interface, on the other hand d_{xz} or d_{yz} electrons naturally extend further away from the interface [102]. At 90 K, due to low dielectric constant, the injected carrier density is lower than 10 K, thus all electrons are expected to reside in the d_{xy} band and only one type of carrier exists in the system with constant mobility (see Figure 3.12 c). At 10 K, the field

modulated density is higher than 90 K, therefore higher density raises the energy level and the Fermi energy enters the d_{xz} and d_{yz} bands. As both of the states get populated it is expected to observe contributions from carriers of new mobility hence two slopes can be naturally accepted (see Figure 3.12 d). It is important to mention that the d_{xy} band has a larger effective mass in the z-direction than the d_{xy} and d_{yz} bands but it exhibits lower mobility due to Anderson localization [66].

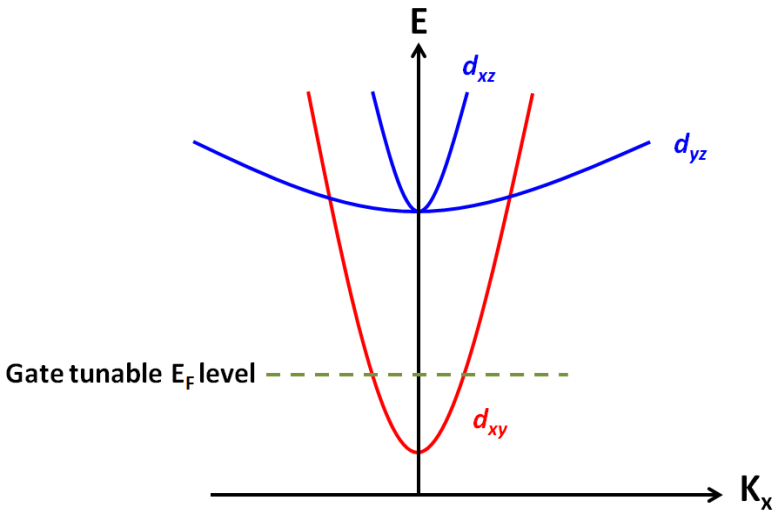

Figure 3.13 *d*-orbital energy bands of $SrTiO_3$ near the interface. The d_{xy} band is lower in energy compared to the d_{xz} and d_{yx} bands, the gate tunable Fermi level is indicated by dash line.

3.8 Combined Effect of Electric Field and Light

The effect of electric field and light together is recently reported by Lei, Y. *et al.* [85]. The authors showed that change in resistance as function of gate modulation can be enhanced, both in response and magnitude, under light illumination of suitable wavelength. In order to further understand this phenomenon, the present study explores this effect by considering the gating cycles in the presence of light illumination with wavelength ranging from visible to ultra violet (UV). According to the measurement scheme (like described in section 3.3), gate voltages (for 5 minutes each step) between +200 V and -200 V were applied to the back gate of $SrTiO_3$ while the c-$LaAlO_3$/$SrTiO_3$ interface was grounded and the 2DEG resistance was recorded with/without light illumination (Figure 3.14).

In the absence of illumination, the application of V_G = +200 V (-200 V) yields two distinct responses marked respectively by a sharp jump followed by a steady decrease (increase) of resistance on the time scale of minutes. The same V_G cycles were then performed under light illumination of different wavelengths, 625, 540 and 445 nm. Before collecting the data under illumination, the samples were first exposed to light for 20 minutes to get the saturated resistance value. The initial decrease in the resistance marked by arrow is due to photoconductivity effect (Figure 3.14). Note that the gate bias was applied for a short time (5 minutes) only; the aim was not to compare the steady state under different conditions.

The gating effect of positive V_G is marginally enhanced by illumination. On the other hand, the field effect in depletion mode (-200 V) is significantly enhanced by light illumination of lower wavelength (Figure 3.14). In the presence of light of photon flux $\Phi = 2 \times 10^{15}$ s^{-1} cm^{-2} (for λ = 625 nm), gate field drives the resistance much faster to ~12 % than the dark (~ 3 %) showing that the slow process has been markedly accelerated by light illumination. The variation in the resistance is progressively decreased with decrease in wavelengths. Other lower wavelengths 540 and 445 nm respectively shows a variation of 11.5 % and 6 % in depletion mode. At zero gate bias, after the -200 V bias, the resistance drops quickly for lower wavelengths in sequence λ = 445, 540, and 625, nm suggesting that only photoconductivity effect is at play.

Similar experiment was also extended to amorphous $LaGaO_3/SrTiO_3$ samples where similar illumination enhanced gating effects are observed, implying a generic nature of this phenomenon.

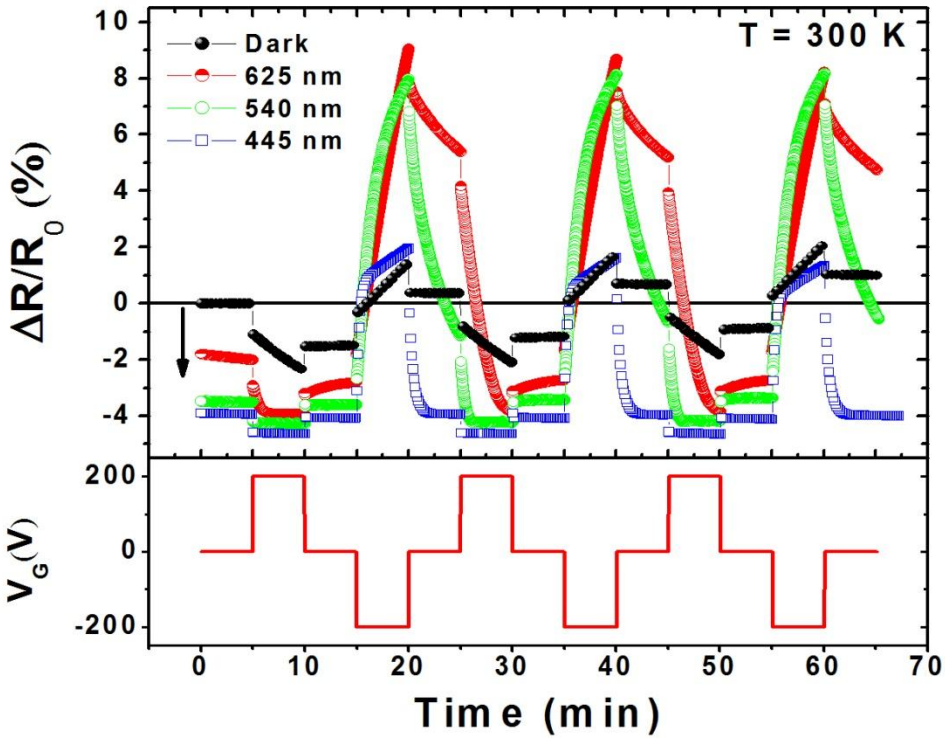

Figure 3.14 Room temperature normalized resistance variations for c-$LaAlO_3/SrTiO_3$ as function of time under field effect, recorded in the presence/absence of a light illumination.

In Figure 3.15, the loops of $\Delta R/ R_o$ vs. V_G are reported for both dark and light conditions. To this aim, 1s long steps of V_G were applied. Initially in the dark, the field effect modulates the resistance by ± 1 % with weak hysterical behavior (Figure 3.15). The sample was then illuminated for 30 minutes by red light (λ = 625) of photon flux $\Phi = 2 \times 10^{15}$ s^{-1} cm^{-2}, and the resistance dropped by 3 % due to photoconductivity effect. Under light illumination, the V_G cycles enhanced the variation in resistance; the span was about ± 2.5 %. Furthermore, the hysteresis corresponding to V_G = 0 was much stronger. Undoubtedly, the total variation in resistance is smaller than Figure 3.14 mainly because of the shorter time spent on each V_G step.

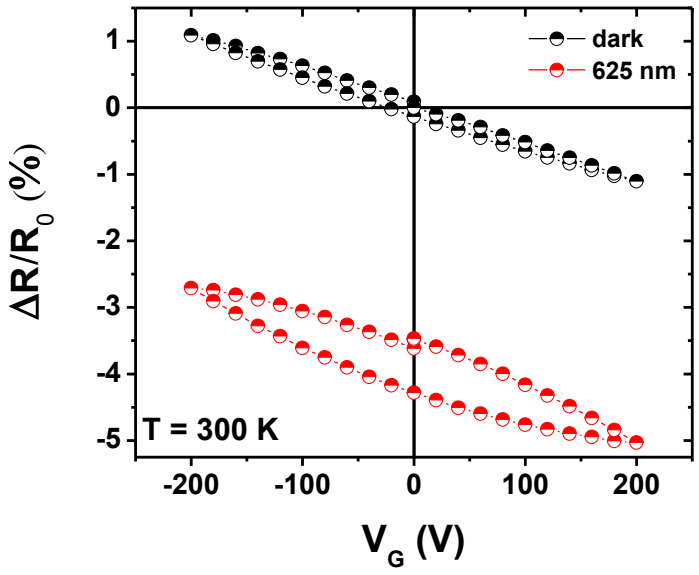

Figure 3.15 Normalized resistance variations for c-$LaAlO_3$/$SrTiO_3$ as function of time under field effect at 300 K, collected in the dark and illumination at λ = 625 nm.

Interestingly, the samples show no variations in resistance by gate modulation in the presence of UV photons (365 nm, 3.4 eV) at flux $\Phi = 1 \times 10^{14}$ s^{-1} cm^{-2}. In Figure 3.16, the gate modulation of sheet resistance in dark and under UV illumination was then compared by using lower photon flux. The resistance variation by field effect in dark shows a quite conventional behaviour. To combine the effect of field and light, the sample was first illuminated by UV light at $V_G = 0$. After 10 minutes the gate voltage was applied. However, even at the lowest exposed flux ($\Phi = 10^{13}$ s^{-1} cm^{-2}) it was impossible to distinguish any clear effect of gating.

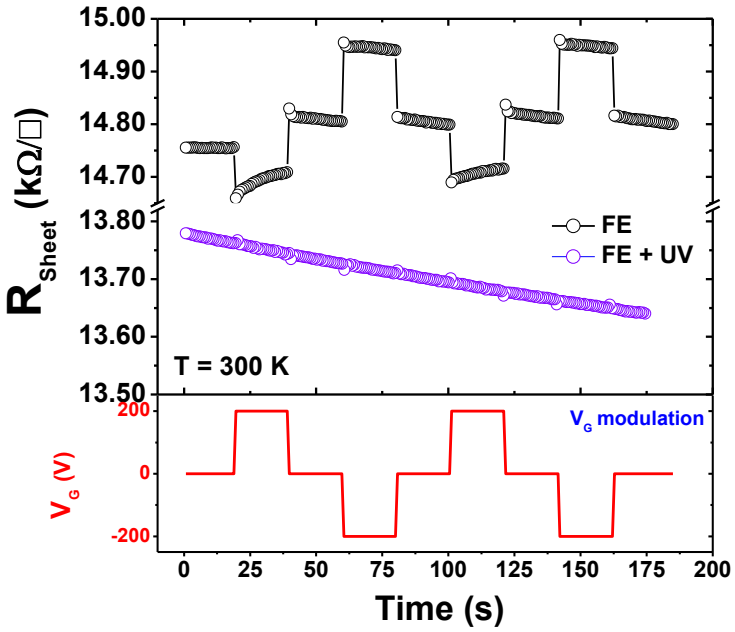

Figure 3.16 Sheet resistance variations for c- $LaAlO_3/SrTiO_3$ as function of time under field effect (FE), recorded in the dark and illumination at λ = 365 nm.

3.9 Discussion

In order to discuss the light-enhanced gating effect consider the gated $LaAlO_3/SrTiO_3$ under the depletion mode, i.e. $V_G < 0$ (Figure 3.17). In dark, before applying the gate bias, the Fermi level in the quantum well and metallic electrode coincide. A negative voltage to the metallic electrode takes away carriers from the quantum well (indicated by red arrow, Figure 3.17). At this point, presumably some electron from the trap states starts to creep into the quantum well (denoted by process 1, black arrow). This delayed dynamics potentially slow down the process and determines the slow transient after the initial jump in resistance (see Figure 3.14).

The creep process can be accelerated by shining light of higher wavelengths (e.g. 625 or 540 nm), because low energy photons can effectively excite trap states (process 2, Figure 3.18). The photo-excited carriers fall into the quantum well and are immediately driven away along the external circuit. High energy photons excite deeper states. With photons at λ = 445 nm, the

mechanism of photo-promotion and of depletion by field effect become competitive. In the considered experimental situation, the photo-promotion is high enough to substantially reduce the resistance drop.

In extreme case of UV photons (3.4 eV), that can promote valance band electron to the quantum well (process 3, Figure 3.18), the mechanism of photo-excitation and field effect become even more competitive. In the present scenario, due to excess of photo-exited carriers, it is impossible to disentangle any clear gating effect.

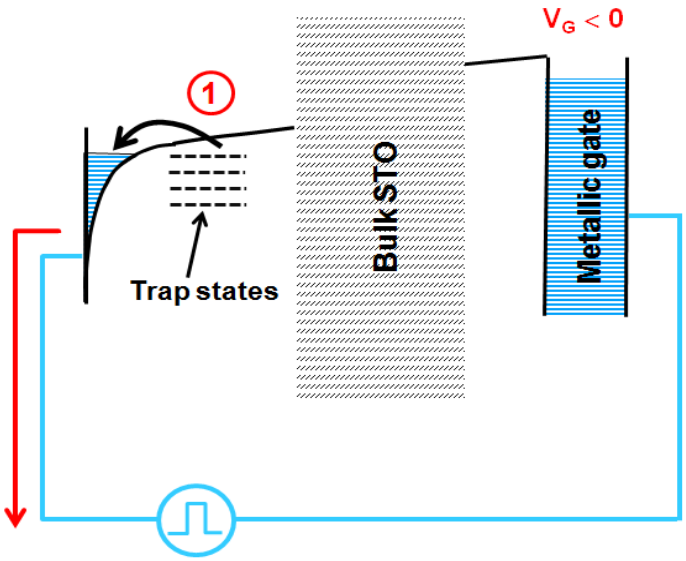

Figure 3.17 $LaAlO_3/SrTiO_3$ band diagram at negative gate bias. Red arrow indicates the electron flow across the external circuit. The black arrow indicates the creep process of electron from the trap states in to the quantum well (process 1).

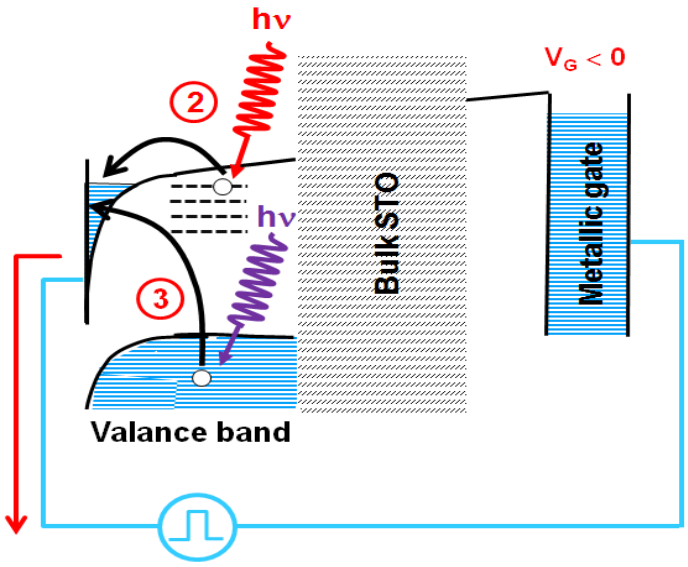

Figure 3.18 $LaAlO_3/SrTiO_3$ band diagram at negative gate bias. The different photo-promotion mechanisms of low and high energy photons are highlighted.

3.10 Summary

In this chapter, the transport properties of interfaces probed by electric field and light were studied. The hysteresis is really significant for T < 70 K but then sharply drops for temperatures above 70 K. The values of mobilities obtained from the slop of $\Delta\sigma$ vs. n plots were discussed in terms of carrier filling in different bands. It was further described with the help of model that gating effect can be enhanced, both in response and in magnitude, in the presence of low energy photons. Such measurement showed no response in the presence of UV light.

Chapter 4

Low Temperature Transport Properties and Electro-optical Switching of oxide interfaces

Abstract

This chapter presents the transport properties of oxides interface under the effect of electric field at low temperature. It is shown that, beside the "standard" field effect, more complex effects take place under the application of a back-gate voltage. Such effects include persistent deep carrier depletion after a positive back-gate voltage that can persistently switch samples with low initial density from the metallic ground state to an insulating state. Such insulating state can be erased by light illumination. We further show that the samples can be repeatedly switched between the conducting and insulating state by the alternated application of suitably tailored back-gate voltage pulses and light pulses.

4.1 Low Temperature Electric Field Effect: First Positive Polarization

As anticipated in chapter 3, the first positive polarization (FPP) when applied at low temperature, persistently changes the resistance of the samples. The first section of the present chapter deals with this effect and its sample-dependence. The most important parameter which determines the FPP behavior turned out to be the intrinsic sheet carrier density of the samples. On this basis the samples were divided into three groups;

- high sheet carrier density sample (sample A, i.e. c-$LaAlO_3/SrTiO_3$)
- intermediate sheet carrier density sample (sample B, i.e. c-$LaAlO_3/SrTiO_3$)
- low sheet carrier density sample (sample C, i.e. a-$LaGaO_3/SrTiO_3$)

The summary of the fabrication and room temperature transport properties of these samples are reported in Table 3.1 of chapter 3.

As a first experiment shown in Figure 4.1 sample A, a "virgin" c-$LaAlO_3/SrTiO_3$ sample (i.e. never having been employed in a field effect experiment before) was cooled to 20 K. A train gate voltage steps lasting one minute each was then applied as shown in the lower panel of Figure 4.1 (a). The response is basically characterized by the change in sheet resistance as function of time under field effect (higher panel of Figure 4.1 a).

The FPP effect is highlighted in Figure 4.1 (b). It takes place after the first V_G = +200 V step and it determines the drop of sheet resistance. The sheet resistance has a sudden drop (from ~ 0.55 to 0.40 kΩ/□), and quickly saturates at ~ 0.43 kΩ/□ (Figure 4.1 b). Afterwards, the FPP persistently changes the resistance of the sample, i.e. the sheet resistance at V_G = 0 from 0.55 to 1.25 kΩ/□ respectively (Figure 4.1 a).

It is also observed that in the cycles that follow the FPP, the sample is stabilized to a metastable state, characterized by a number of notable features: a constant $(R_{sheet})_{-200V}$ value (the subscript indicating V_G) as a function of time; a time-dependent $(R_{sheet})_{+200V}$ value, characterized by a time constant of the order of minutes; and an hysteretic $(R_{sheet})_{0V}$ value, that is higher after the positive V_G pulse and lower after the negative pulse. Particularly the latter parameter is strongly temperature dependent, and it is furthermore it is very sensitive to the cooling and heating cycles. The properties of such metastable state have been thoroughly reported in chapter 3, so that the attention here will be focused on the mechanisms associated to the FPP only.

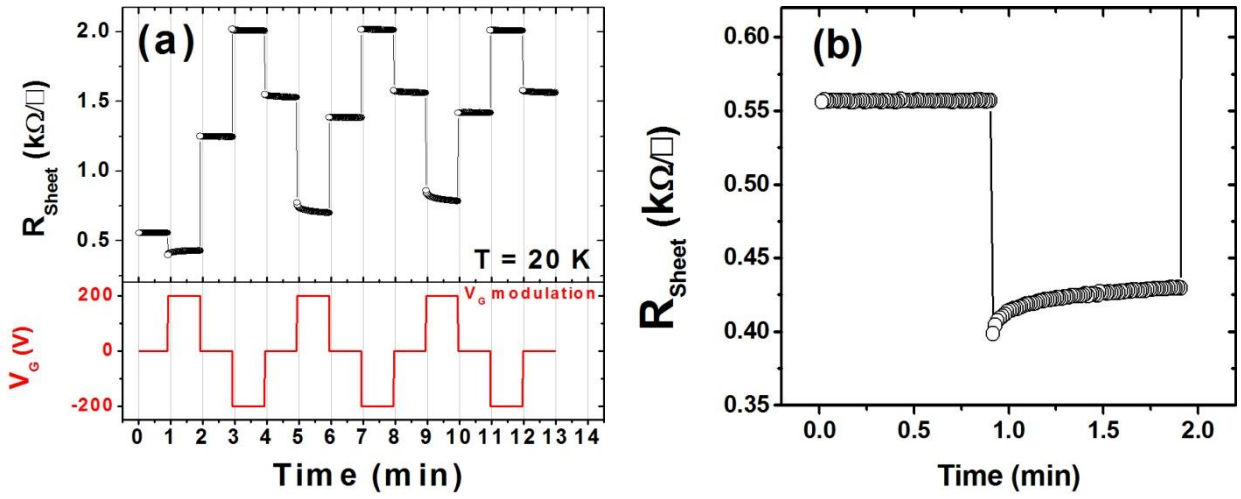

Figure 4.1 (a) Sheet resistance of the 2-DEG as functions of gate voltage measured at 20 K in a sample with high sheet carrier density (sample A). (b) The FPP effect is highlighted.

The same measurement procedure was extended to sample B. The R_{sheet} vs. V_G plot is qualitatively similar for both samples, but quantitative differences are strong, particularly in the depletion mode. Sample B shows the same FPP effect after first V_G = +200 V step as indicated in Figure 4.2 (a,b). On the other hand, after the -200 V step, the sheet resistance increases by at least three orders of magnitude and falls out of the sensitivity range of the instrumentation (Figure 4.2 a). The measurement compliance limit is indicated by gray region (~ 9 MΩ/□). In the following cycles, the sample passes from insulating state at V_G = -200 V to conducting state at V_G = 0 and V_G = +200 V.

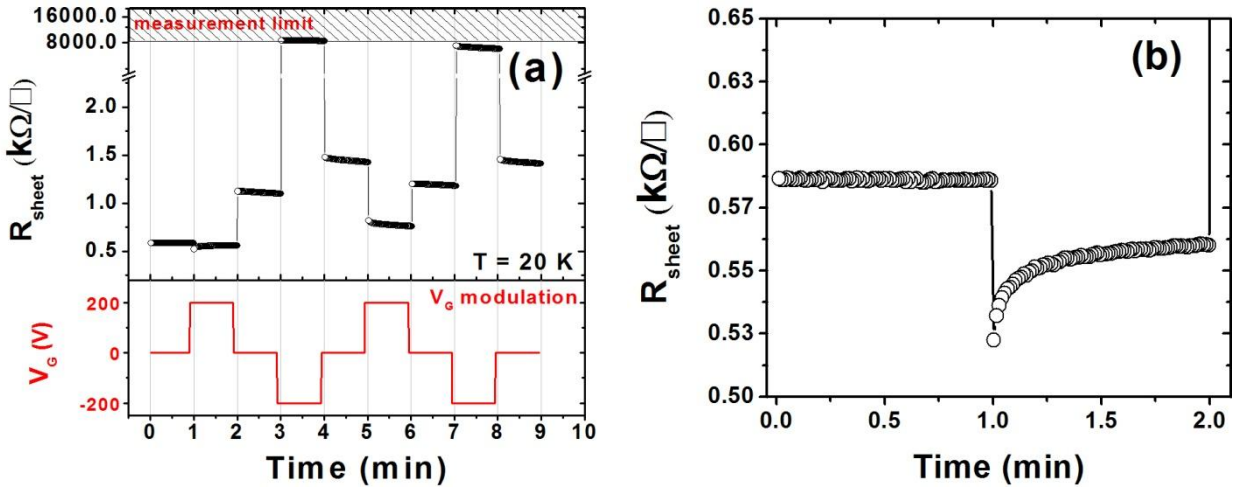

Figure 4.2 (a) First positive polarization at 20 K for the sample with intermediate sheet carrier density (sample B), the sample switches to insulating state at V_G = -200 V (b) The FPP effect is highlighted.

Figure 4.3 reports a similar characterization for sample C. During the FPP, the maximum measured sheet resistance in this case is about 0.7 kΩ/□ (Figure 4.3 a,b), which is higher than the previous two cases of sample A and B. After the FPP, the sample is brought into a deeply charged-depleted mode, with a sheet resistance increase of at least four orders of magnitude. The sample remains in the insulating state even when V_G is brought to zero (Figure 4.3 a), thus demonstrating the behavior of a non-volatile memory. In order to erase the memory, a step at $V_G > 0$ is required.

To investigate the minimum erasing voltage, measurements were performed where the positive step is applied at V_G = 100 V (Figure 4.4). It was found that the sheet resistance is decreased only to ~ 700 kΩ/□, demonstrating that this gating was insufficient.

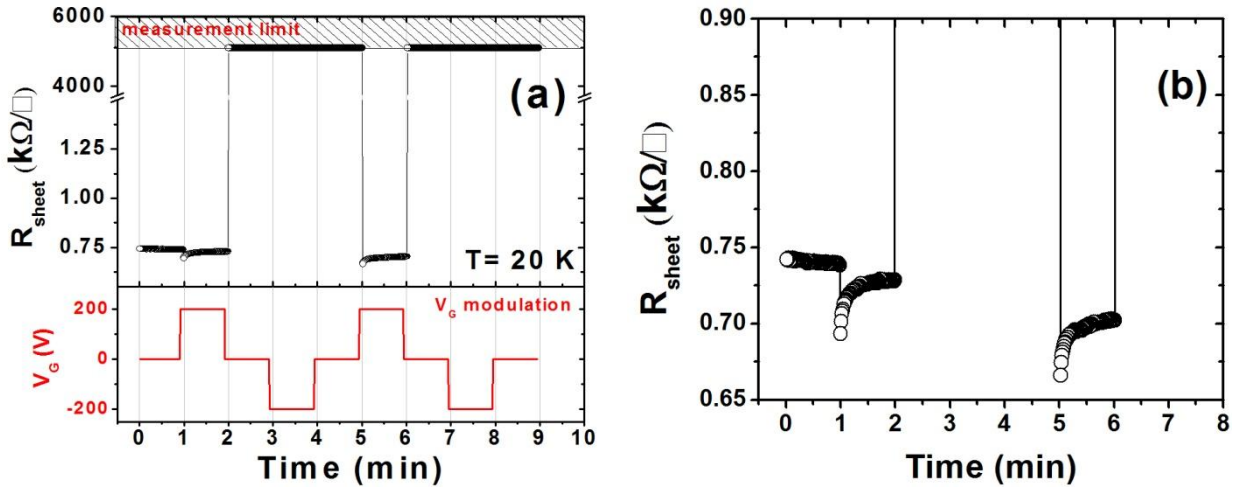

Figure 4.3 (a) First positive polarization at 20 K for the sample with low sheet carrier density (sample C), the sample remains in insulating state for V_G = 0 and -200 V. (b) FPP effect is repeatable for each positive gate bias.

Measurements were performed at 100, 60, and 40 K to investigate the temperature dependence of the memory effect. Figure 4.5 shows the result for sample C. After the FPP, the maximum sheet resistance observed in depletion mode is ~ 15 kΩ/□, so that the insulating state is not observed. Note, however, that it is at all possible that the insulating regime may be obtained by applying a higher voltage, in order to compensate for the reduction of ε_r with temperature.

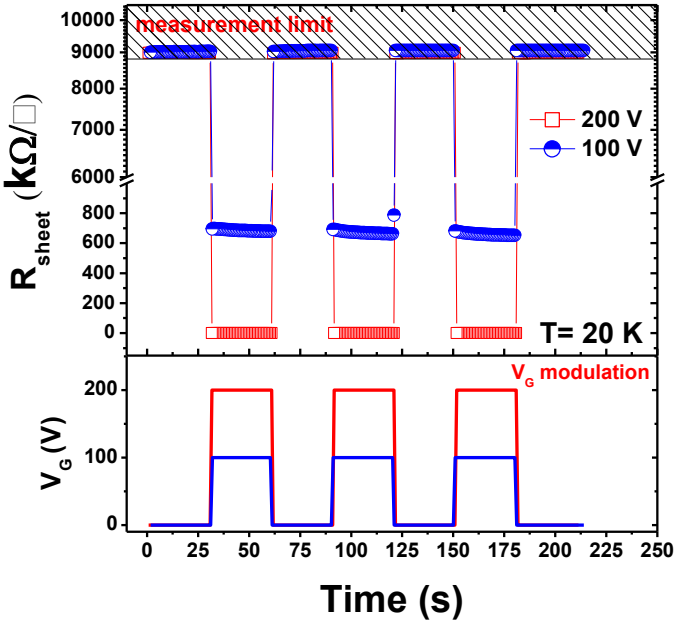

Figure 4.4 V_G modulation of sheet resistance at 20 K for sample C showing that the complete conducting state after FPP can be restored only at V_G = +200 V and not by lower voltage.

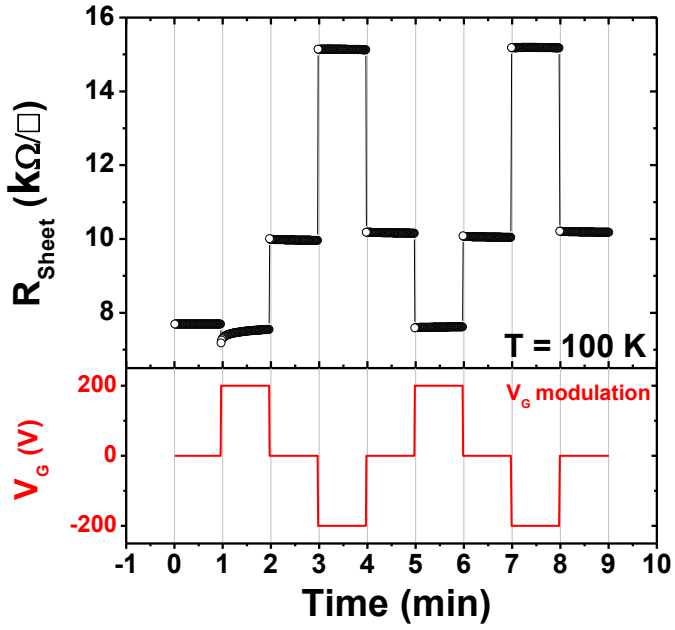

Figure 4.5 V_G modulation of sheet resistance for sample C at 100 K, measurable changes in the sheet resistance indicates that the giant effect after FPP (deep charged-depletion) occurs only at low temperature (20 K).

4.1.1 R_{sheet} (T) Curves in Field Effect

The persistent change of the samples sheet resistance after first positive polarization (FPP) is clearly manifested in the sheet resistance vs. temperature plots. As an example, in Figure 4.6 (a) the virgin R_{sheet} (T) for sample A is compared with R_{sheet} (T) after performing the gate voltage measurement at low temperatures. Both curves show data collected during sample cooling. To this aim, the sample was first cool down to 10 K (black solid curve), then the gating cycles were performed in the temperature range 20-300 K at gate bias ± 200 V. The values of sheet resistance at $V_G = 0$ and at $V_G = \pm 200$ V are indicated by the solid dots. The first gating cycle ($V_G = 0$, $V_G = +200$ V and $V_G = 0$) at 20 K persistently brought the sample into a high resistance state different from the virgin state (black arrow).

The R_{sheet} (T) of sample C is substantially different (Figure 4.6 b). The FPP at 20 K sent the sample to the insulating state. Upon heating, around 170 K the sample resistance become measurable but still at room temperature the sheet resistance is one order of magnitude higher than the virgin state.

Previous studies [3, 84] revealed that the metastable state due to the low temperature gating cycles can be erased by warming the samples to room temperature. This procedure did not prove to work in the present study. Instead, a special technique of long gate treatment for ~15 hours in the carrier enhancement mode (+200 V) at room temperature (Figure 4.7 a) has proved to be always effective. This treatment brought all the samples back to the virgin state. The a-$LaGaO_3/SrTiO_3$ (sample C), however, took only 30 minutes to restore its initial state (Figure 4.7 b). The R_{sheet} vs. T of the sample A and C in the virgin state and in the recovered state are compared in Figure 4.6 a and b.

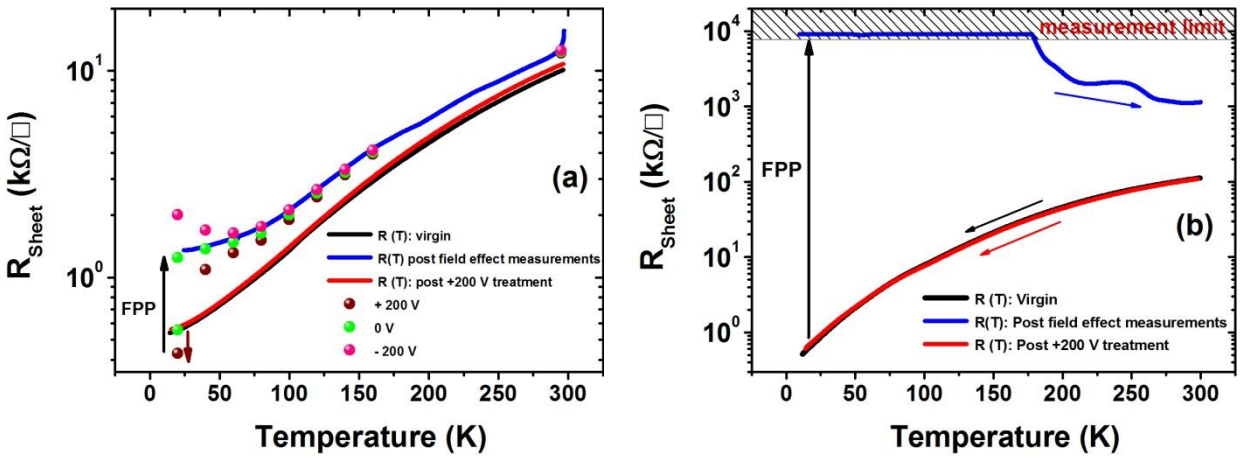

Figure 4.6 R_{sheet}-T curves for virgin and gate voltage treated samples (a) c-$LaAlO_3$/$SrTiO_3$ (sample A) and (b) a-$LaGaO_3$/$SrTiO_3$ (sample C). The arrow marks the FPP effect.

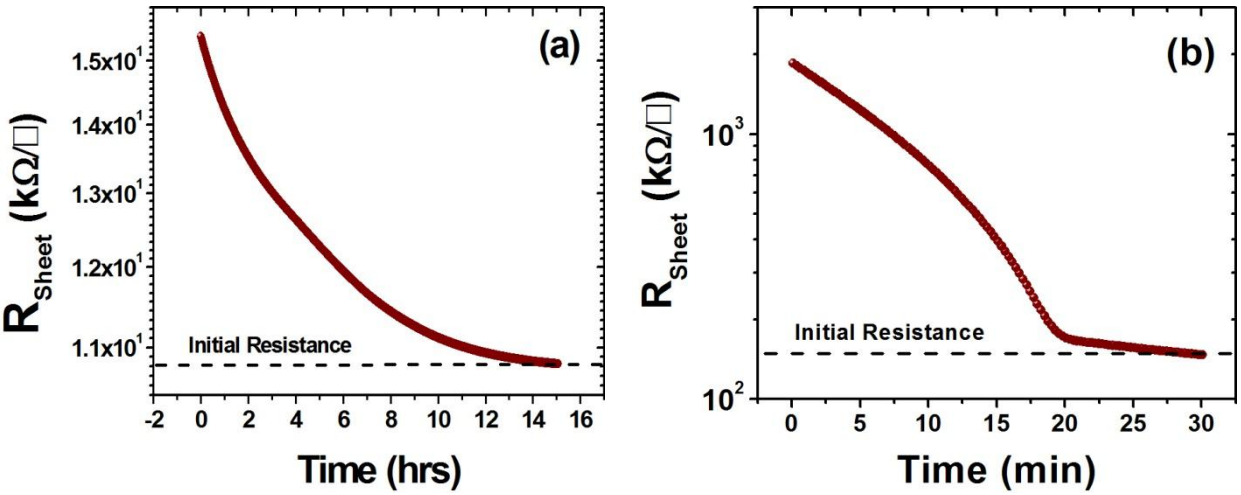

Figure 4.7 Recovery of the pristine state of (a) sample A and (b) sample C under the effect of a gating at 300 K. Note the different time-scale of the processes.

4.1.2 Model for First Positive Polarization

In the section 3.3 of chapter 3 the energy band diagram of gated $LaAlO_3/SrTiO_3$ has been introduced. In order to discuss the First Positive Polarization (FPP) effect one ought to modify the band diagram by considering empty localized in-gap states (LIGS) in the vicinity of the quantum well on $SrTiO_3$ side [3, 64]. The modified band diagram can be compared with the floating gate MOSFET device. In the following the floating gate MOSFET is shortly discussed, in order to introduce the comparison with oxide interfaces and, to explain the FPP effect.

The difference between the floating gate MOSFET [103] and the standard MOSFET is the addition of a new gate, called the floating gate (labeled as "c" in Figure 4.8), between the original gate ("e") and the channel ("a"). The original gate is called the control gate. The floating gate is an isolated conducting island: it is surrounded on all sides by oxide insulator (marked as "b" and "d"). The channel is typically realized by conducting n-type source and drain through a p-type path, that is simplified in the sketch in Figure 4.8.

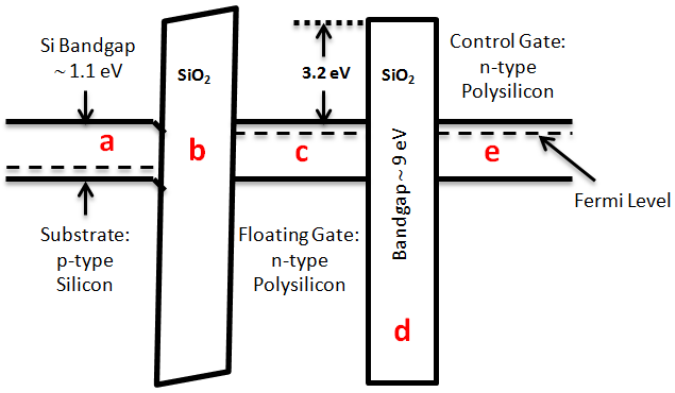

Figure 4.8 Energy band diagram of floating gate MOSFET.

In the operation, a positive V_G is applied. If the electric field that is hence built in the region between the channel and the floating gate is high enough, the floating gate is charged by either the Flower-Nordheim (FN) tunneling (mechanism 1 in Figure 4.9 a) or via hot-electrons injection (mechanism 2 in Figure 4.9 a) [104]. Once the electrons are "captured" in the floating gate, they stay there even in zero field, because there is no direct path for them to flow back (Figure 4.9 b). This retention mechanism makes a non-volatile memory floating gate MOSFET devices.

To discharge the floating gate, a negative voltage pulse is applied at control gate. The same effect is also achieved by shining the UV light (3.4 eV), in such a way that the photons provide the trapped electrons the energy required to overcome the barrier (3.2 eV).

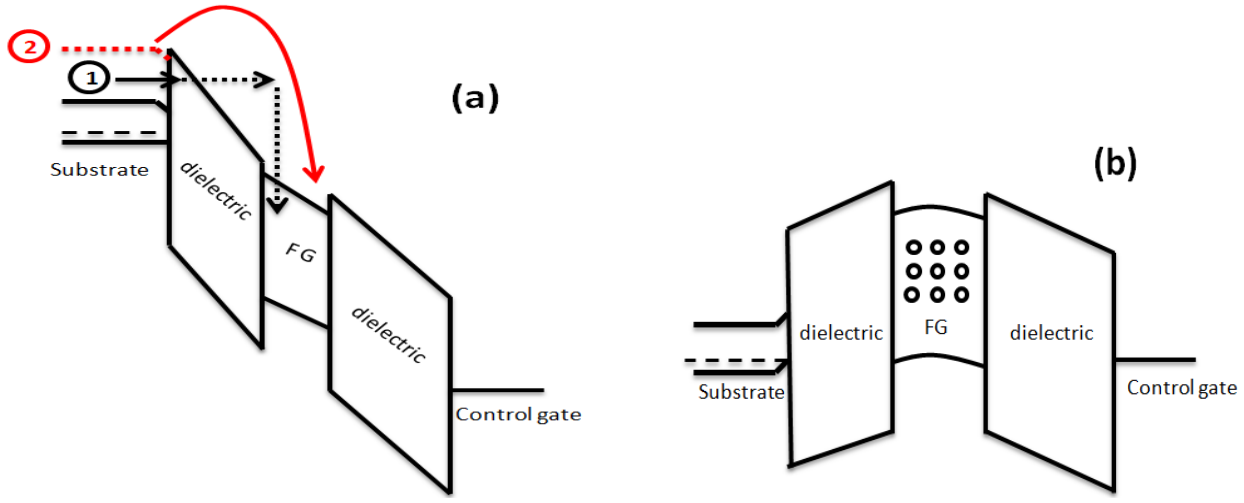

Figure 4.9 (a) Positive V_G at the control gate charge the floating gate via (1) Flower-Nordheim tunneling mechanism or (2) via hot-electrons injection. (b) At $V_G = 0$ the electrons are captured in the floating gate.

Figure 4.10 shows the band picture of a gated oxide interface. For convenience the same notation is used in both band diagrams (Figure 4.8 and 4.10). In the gated oxide interface the quantum well acts as the conducting channel. The empty localized in-gap states (LIGS) act as floating gate ("c") separated from the channel by a thin insulting layer (with thickness of the order of *nm*), marked as "b". The dielectric bulk $SrTiO_3$ ("d") isolates the metallic gate from the rest of the system.

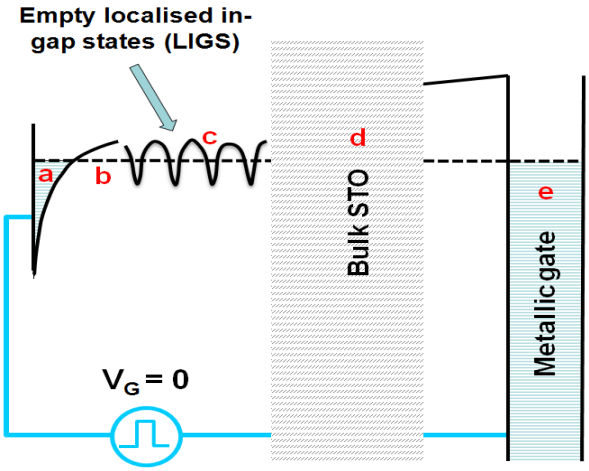

Figure 4.10 Energy band diagram of the back-gated oxide interface, the empty localized in-gap states (LIGS) in the vicinity of the quantum well act as floating gate. At zero gate bias the Fermi level of 2DEG and metallic gate coincide.

Based on this band diagram the effect FPP can be explained as follow. In order to be definite, the situation of sample A is considered. Imagine that a gate bias is applied in the sequence 0 → +200 → 0 → -200 V (lower panel of Figure 4.11). At V_G = 0, the Fermi level of 2DEG and metallic gate are aligned (state 1). At positive V_G, the Fermi level in the gate electrode is lowered and some charge transferred from the electrode to the quantum through the external circuit. But at the same time, if the quantum well is filled up, part of the charge creeps from the quantum well into the LIGS (labeled as "2" in Figure 4.11 and 4.12 b). By applying again V_G = 0, the charge transfer is reversed. However, the electrons trapped in the LIGS cannot flow back to the gate, so that in the equilibrium the quantum well filling will be less than in the virgin state (state 3). Note

that here a 'sum rule' applies: the equilibrium conditions at $V_G = 0$ imply that the sum of the charges in the quantum well plus the LIGS is kept constant, or otherwise an electric field develops and a gate voltage appears. During the successive cycles, no further filling of the LIGS takes place. Once the excess electrons have been “trimmed”, in fact, the Fermi level never exceeds again the edge of the quantum well, even under positive bias.

The sample is now persistently different. In order to bring it back to the virgin state, the procedure described in section 4.1.1 is required. This is quite different from the floating gate MOSFET. However, just as for those devices, it is possible to use light to erase memory. This will be shown in section 4.2.

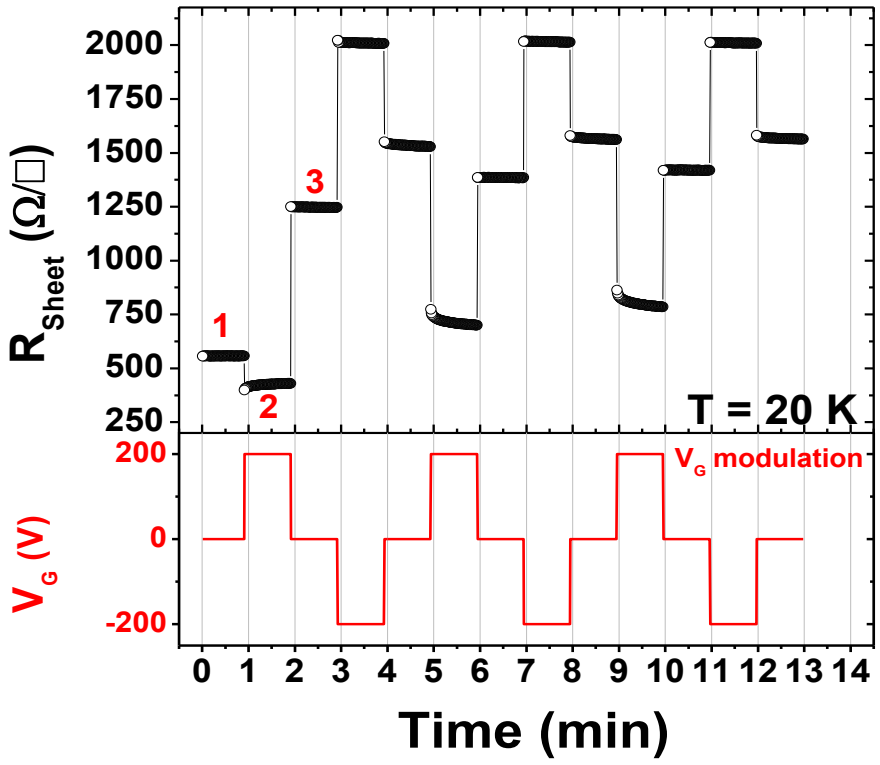

Figure 4.11 Sheet resistance of the 2-DEG vs. time under the effect of gating for sample A at T = 20 K).

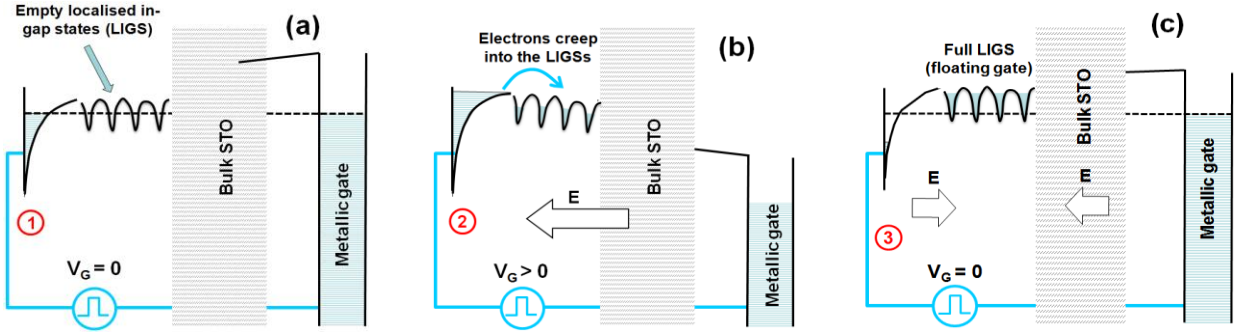

Figure 4.12 Energy band diagrams of a back-gated oxide interface (a) before applying gate bias, a virgin state; (b) during FPP, shows the carrier escape to LIGS; (c) after FPP, indicates the filled LIGS states.

4.1.3 De-trapping from LIGS

Previous studies demonstrated that the electrons trapped by LIGS are released by a thermally activated process with two characteristic temperatures, i.e ~ 70 K (6 meV) and ~ 170 K (14.5 meV) [3, 105]. Let "l" be the distance at which electron are trapped from the interface, "l" is comparable to the quantum well extension (~ 10 nm), which is much smaller than the thickness d = 0.5 mm of the $SrTiO_3$ substrate. It is not possible to de-trap the electrons by a negative gate voltage (V_G = -200 V) because the potential energy drop between the LIGS and Fermi level in the quantum well is $eV_G \times l/d$ ~ 4 meV, that is still lower than the necessary 6 meV. Partial resetting by samples warming to room temperature can be understood as a result of the shallow nature of the defect states. At the same time, it was observed (see Figure 4.6 a,b) that only warming to the room temperature is not generally enough. This may be also ascribed to the characteristic energy of some defect states, even though further analysis about this issue is required.

4.2 Alternative Re-setting Technique

It was presented in section 4.1 that the first positive polarization (FPP) at low temperature persistently brought the samples to high resistive states or even to insulating state. It was further shown that the initial state can be restored by heating the samples to room temperature and then by applying a gate voltage V_G = +200 V for several hours. For some samples this resetting procedure can last as long as 24 hours. This circumstance motivated the search for a different approach to the problem of sample resetting. The alternative route is based on the action of light, as illustrated by the following example.

Figure 4.13 shows the effect of electric field and light at 20 K for sample C. The sample had been brought into a deep depletion state after FPP. By exposing the sample to red light (indicated by arrow) at energy 1.98 eV (λ = 625 nm) with photon flux $\Phi = 10^{14}$ s^{-1} cm^{-2}, the previous conducing state was restored and stabilized even after light was turned off.

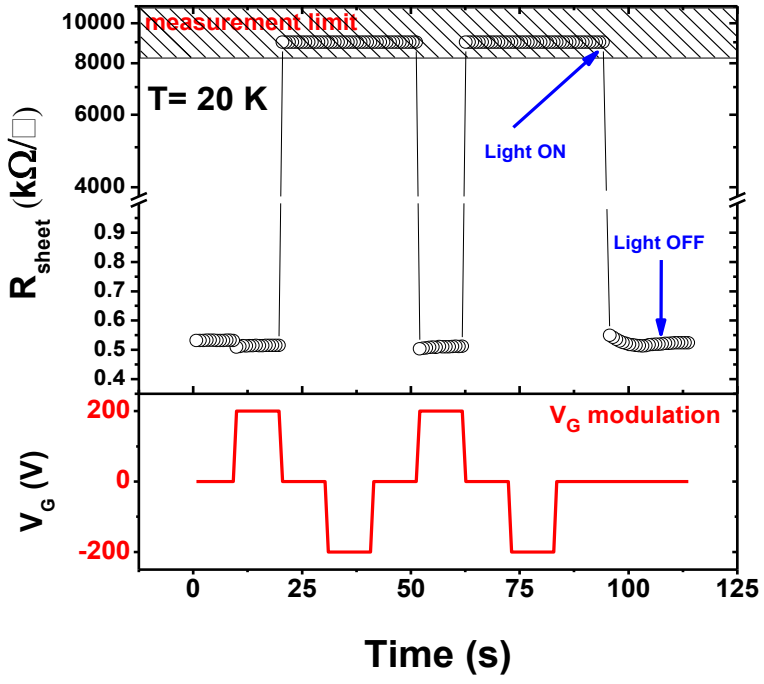

Figure 4.13 V_G modulation of R_{sheet}, for sample C, the insulating state is erased by shining red light the subsequent conducting state prevails even after the illumination is stopped.

The effect is also shown in Figure 4.14, where the full history of the sample treatment is shown. The sample is first cooled down, then subject to the FPP/light exposition cycling, shown by the arrows, and finally heated up again. The R_{sheet} (T) curve upon heating after resetting by exposure to light is not very different from the R_{sheet} (T) collected during the first cooling.

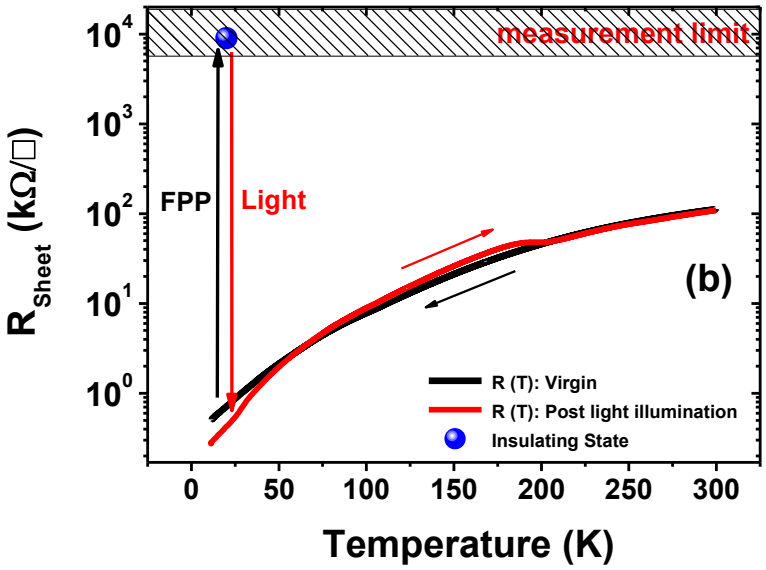

Figure 4.14 Thermal cycling of the sample, showing that the exposure to light after FPP effectively restores the pristine transport properties.

4.3 Oxide Interfaces as Optoelectronic Devices

The above mentioned results lead to the idea of electro-optical operation of oxide iInterfaces. In fact, the devices are driven to insulating state by a voltage pulse, while the light illumination restores the conducting state. Figure 4.15 represents one such cycle (λ = 625 nm, photons flux Φ = 10^{15} s^{-1} cm^{-2}). After the voltage pulse was applied for < 3 s (left vertical scale of the lower panel), the sheet resistance increased by more than four orders of magnitude. The sample was then exposed to light for 20 s (right vertical scale of the lower panel) to restore the conducting state. The remarkable outcome of this measurement is that oxide interfaces can be set in two stable states with dramatic difference in transport properties, i.e. can be operated as non-volatile memories.

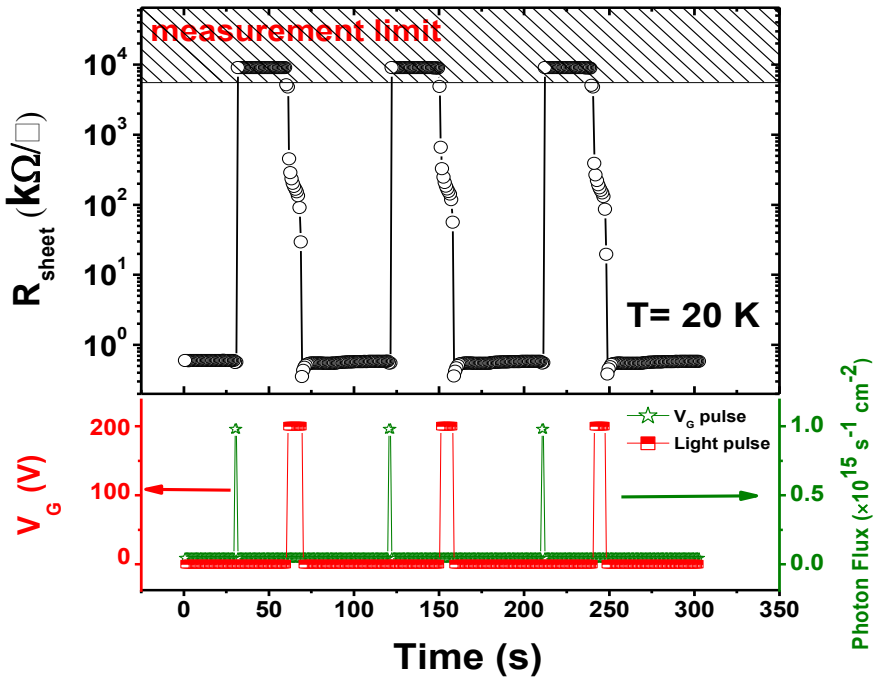

Figure 4.15 Electro-optical switching for sample C, high and low resistive states can be obtained by alternately applying voltage (left vertical scale in lower panel) light pulse (right vertical scale in lower panel) respectively.

The seemingly slow dynamics is not a real concern. It must be brought in mind that here we deal with 0.5 mm thick $SrTiO_3$ barrier between channel and gate and with device area ~ 5 × 5 mm^2. A scaling of devices is expected to completely change the scenario. However, it is worth to explore the application of different light sources.

Figure 4.16 shows the variation in sheet resistance of the sample subject to alternate voltage and light pulses of red light with higher intensity of photon flux $\Phi = 10^{16}$ s^{-1} cm^{-2}. The switching is now fast enough to be out of the range in the DC measurements.

By using the green light at energy 2.30 eV (λ = 540 nm) or blue light at energy 2.70 eV (λ = 445 nm) with lower intensities of photon flux $\Phi = 10^{14}$ s^{-1} cm^{-2} the response is also fast (Figure 4.17). However, there is a problem associated to green and blue light; the insulating state after

exposition to such sources becomes unstable. This means that green and blue light perturb the sample persistently and hence the robustness of the switching (metal to insulator transition) is compromised.

The best example of such unstable effect is Figure 4.18, showing data collected after sample exposure to blue light. Like in the standard procedure, the sample is sent to the insulating state by a voltage pulse. However, after the gate voltage is set to zero, the insulating state is not stabilized as a result of previous illumination (20 minutes before the experiment). The sheet resistance spontaneously drops about one order of magnitude before a blue light pulse is applied. In the following cycles the spontaneous drop is more and more evident, until the stable conducting state is spontaneously recovered at the time indicated by the arrow (Figure 4.18).

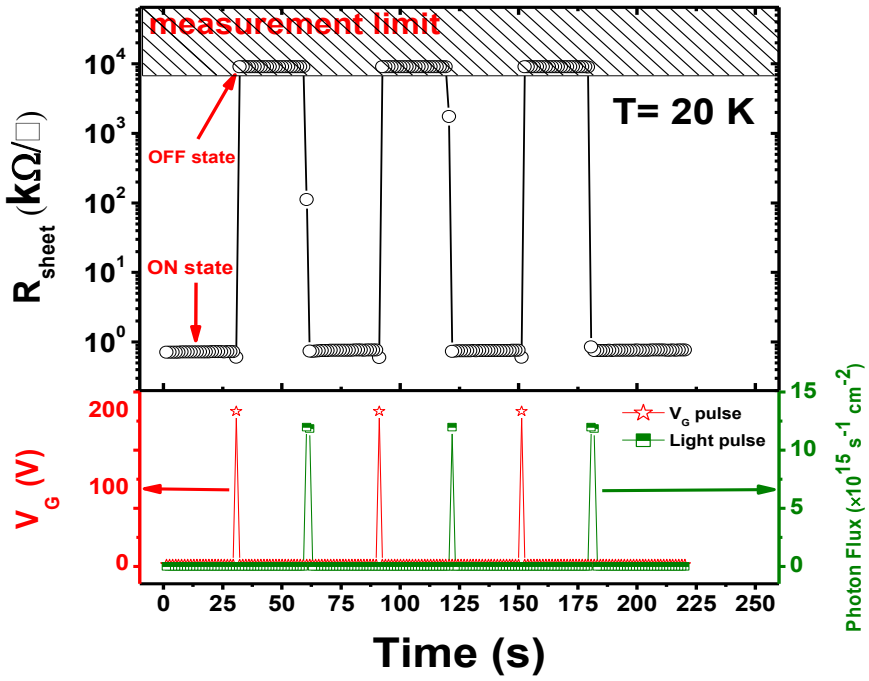

Figure 4.16 Electro-optical operation for sample C, the insulating state is erased faster when resorted to higher intensity of photon flux $\Phi = 10^{16}$ s^{-1} cm^{-2}.

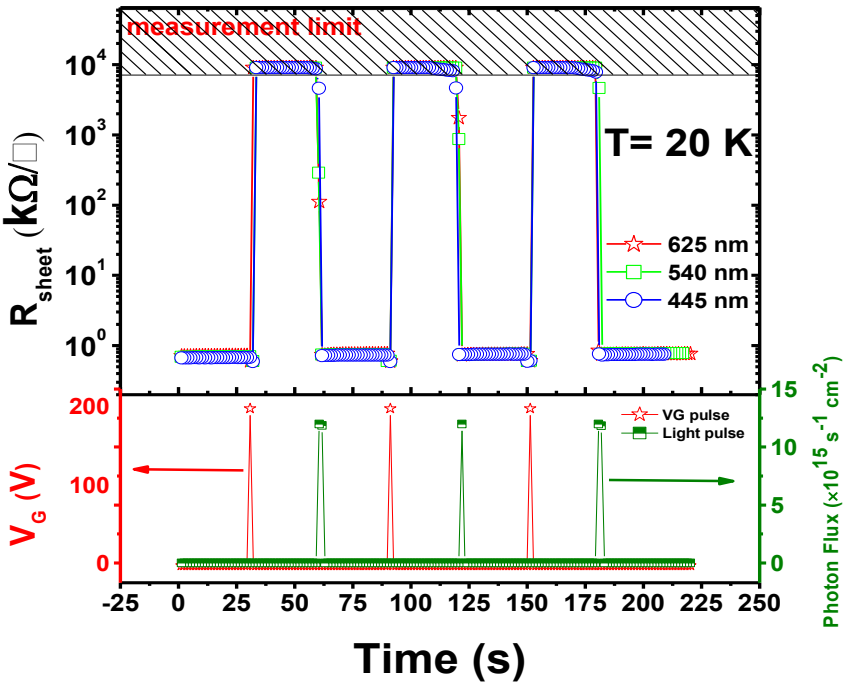

Figure 4.17 Electro-optical switching for sample C, accomplished by red, green and blue light.

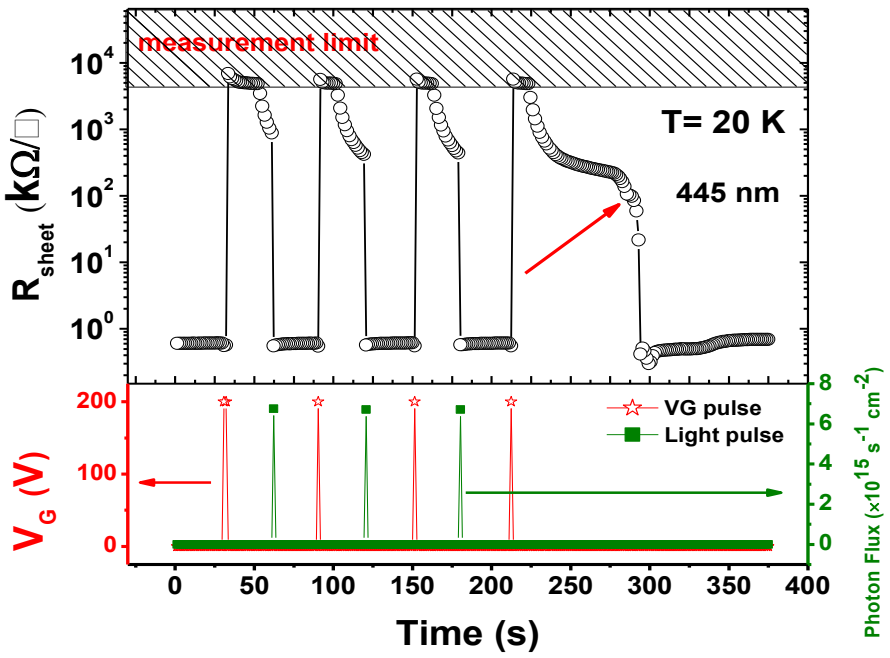

Figure 4.18 Electro-optical operation with λ = 445 nm, showing the spontaneous drop of sheet resistance after the gating.

4.3.1 Electro-optical Switching: Multi-level Control of Resistive States

The previous experiment indicates that there is an accumulative effect in light exposure. This is actually also true for exposure to the gate voltage, as shown in Figure 4.19. The sample was exposed to a series of V_G pulses with increasing voltage.

Initially, V_G = +25 V was applied as FPP, the sheet resistance of the sample jumped by less than three orders of magnitude. Next, after applying a gate voltage of 50, 75, 100 V the sheet resistance increased step by step; the later jumps are smaller in magnitude than the very first low voltage jump (V_G = +25 V). The sample was eventually sent to the insulating state at V_G = +125 V. Similarly, while switching from insulting to conducting state, a red light of low intensity of photon flux $\Phi = 10^{14}$ s^{-1} cm^{-2} was used to slightly change the sheet resistance. Each time the sample was exposed for 3s, the sheet resistance dropped by less than one order of magnitude. The intermediate states were observed for a few minutes. The final drop in sheet resistance during the last light exposure is of nearly three orders of magnitude.

An important issue of the electro-optical switching is the stability of the resistive states. It was found that the levels are unstable for V_G < 100 V, corresponding to $R_{sheet} < 10^3$ kΩ/□ (Figure 4.19). For higher voltages (V_G = 125-200 V) the states exhibit good stability. Similarly, for the light exposure the sheet resistance is stable for $R_{sheet} > 10^3$ kΩ/□ whereas it is relatively unstable for $R_{sheet} < 10^2$ kΩ/□.

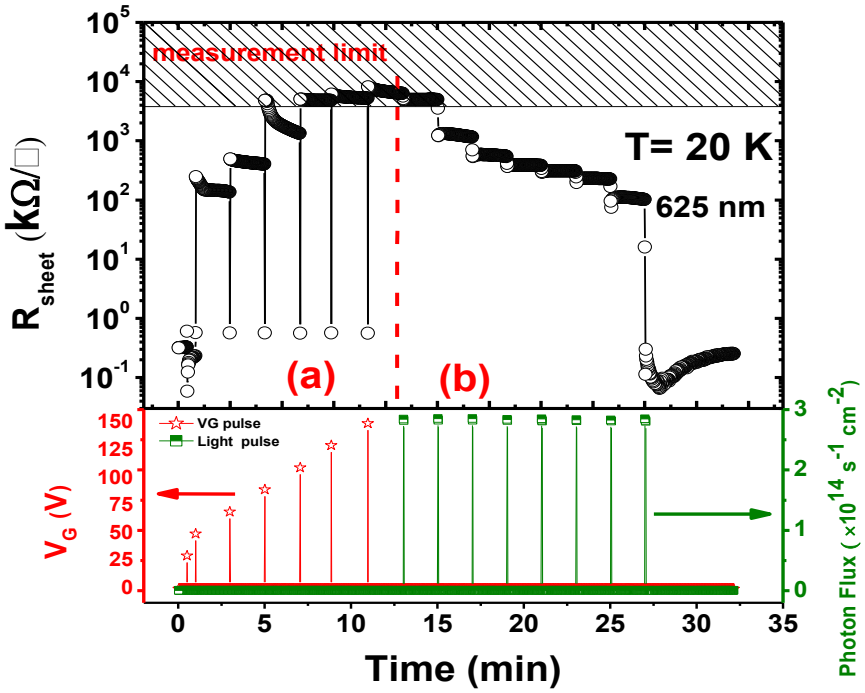

Figure 4.19 (a) Effect of a sequence of positive V_G pulses with increasing amplitude. During each positive gating the sheet resistance is low; immediately after, as an effect of FPP, the sheet resistance goes high. The high-resistance value depends on the positive gating value and displays a multi-level nature. (b) Effect of a sequence of light pulses (λ = 625 nm, Φ = 10^{14} s^{-1} cm^{-2}). After each pulse the sheet resistance partially drops, displaying again its multi-level nature.

Further measurements were performed to check the long time stability. As an example, Figure 4.20 shows that a measurement lasting for several hours. After the FPP at V_G = + 60 V, the sheet resistance increased by more than three orders of magnitude. This state was observed for two hours until a V_G = +200 V pulse was used to send the sample to a high resistance state. Afterwards, the sample was left unperturbed. During 9 hours, the sheet resistance only slightly decreased from ~ 9×10^3 to 7×10^3 kΩ/□.

Similarly, to verify the stability after one resistance level was determined by light exposure (Figure 4.20), the sample was exposed to train of pulses of light (λ = 625 nm, Φ = 10^{14} s^{-1} cm^{-2}, t = 3s). The resistive states were observed for 1-2 hours, always finding good stability. Eventually, the system falls to a very low resistive state. This state was tried to stabilize by light exposure together with positive gate voltage, but it soon restored to pristine state. The origin of such low resistive state at present is not clear.

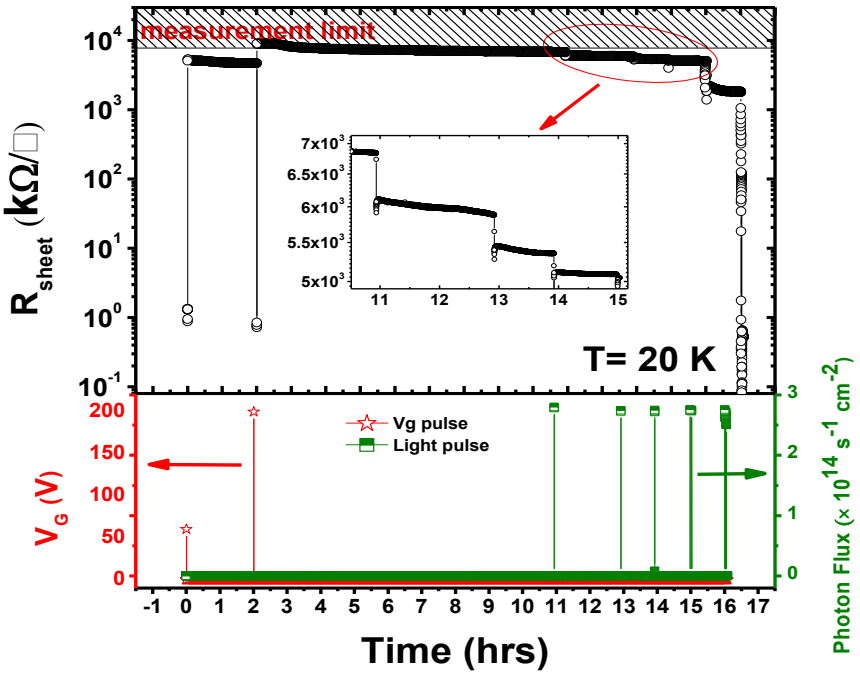

Figure 4.20 Multi-level electro-optical switching showing stability on the time scale of hours. Insert shows different resistive states accessed by red light illumination.

4.4 Discussion

In section 4.1 the possible operation of an oxides interface as non-volatile memory was introduced. It was shown that it is possible to fabricate sample (e.g. sample C, see Table 3.1 in chapter 3) that can be commuted between high and low-resistance states and that can persistently remain in both such states in the absence of external perturbation. The 'OFF' state, i.e. the high-resistance state is achieved by first positive polarization (FPP). This section discusses the issue of the erasing mechanism, i.e. the switching to the 'ON' state of low-resistance, as accomplished by light illumination.

In the virgin state, the localized in-gap states (LIGS) close to the quantum well are mostly empty and the device is in 'ON' state (Figure 4.21 a). As already explained, (see section 4.1.2), after the FPP the LIGS states are filled, thus leaving the quantum well depleted (Figure 4.21 b). The electrons that are injected into the floating LIGS are trapped by the energy barrier (~ 6 meV) [3]. Therefore, the rate of spontaneous emission of electrons from the oxide over this barrier is negligibly small. A sufficient energy must be provided to over the barrier. This is done by illuminated the samples with red light (1.98 eV, λ = 625 nm), transferring the charges from the LIGS back to the quantum well, the device is in ON state again (Figure 4.21 c). These cycles can be repeated many times.

Controlling the intermediate resistive states at lower voltages (Figure 4.19) can be discussed in term of band bending and creeping of the carriers from the quantum well into the LIGS in a controlled manner. Gate bias > 125 V completely deplete the quantum well. Instead, by lower voltages (like 25, 50 100 V) only some part of carrier is transferred to the LIGS. In this case the quantum well still contains carriers that contribute to the conductance, thereby allowing to access the intermediate resistive states.

Similarly, during the light illumination of samples in the 'OFF' state, the light pulses gradually add carriers to the quantum well from the LIGS, thus decreasing the sheet resistance step by step.

Qualitatively, the device operation discussed above resembles the EPROM (erasable programmable read-only memory) device which is a type of memory chip that retains the data even if power supply is switched off [104]. In EPROM devices, the floating gate is programmed

(charged) by an electrical signal to the control gate. Once programmed, it can be erased by exposing it to strong UV light.

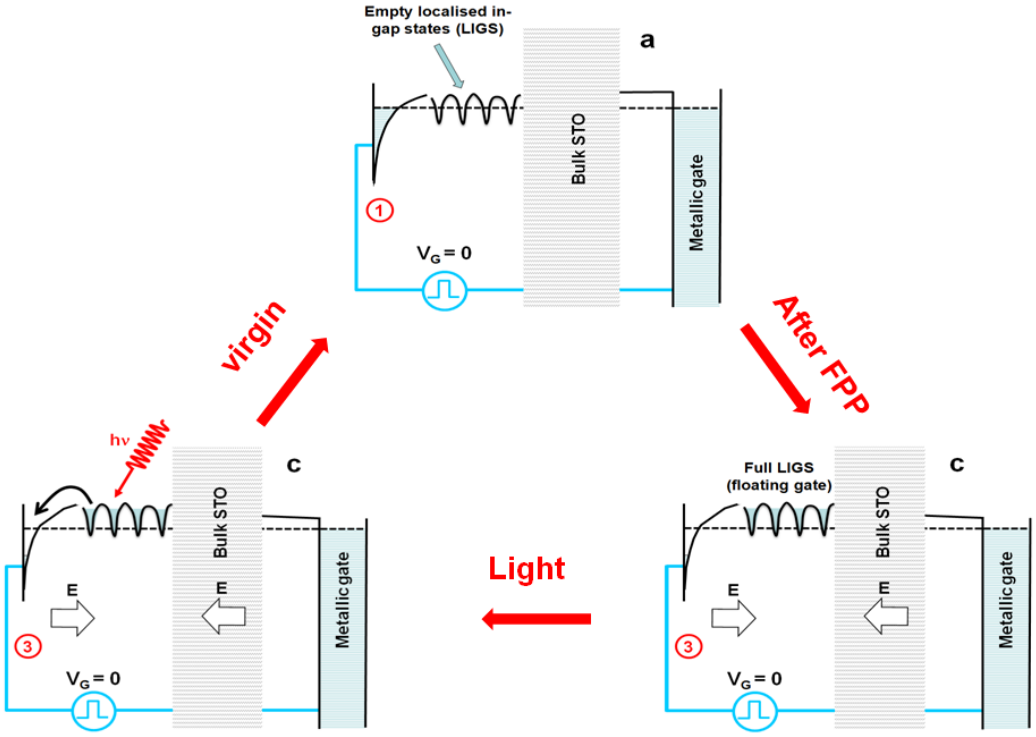

Figure 4.21 Sketches to explain the erasing process by light (a) before applying gate bias, a virgin state (b) PFF results in full LIGS (c) light illumination brought the sample back to the virgin state.

It is worthwhile noting that the devices demonstrated in the present work cannot be quantitatively compared with the devices used in the flash memory because of the following reasons.

In flash memory device, the thickness of the dielectric layer is ~ *nm* [104], while in the present study the thickness of the dielectric is of the order of *mm*. Thus, at equal applied bias, the electric

fields differ by at least five orders of magnitude. Experimentally measured switching time for the ultrafast metal-insulator transition in VO_2 based electronic probed by different pump-probe methods was in the range of *fs-ps* [106]. In order to obtain the minimum switching time and hence the maximum device operation speed, one needs, obviously, to diminish the device dimensions.

For the room temperature operation of the present electro-optical device the real issue might be the barrier height of the LIGS (~ 6 meV) [3]. The sufficiently high room temperature thermal energy (~ 25 meV) can destroyed the insulting state. In principle, deep level defect can be introduced in $SrTiO_3$ by doping to overcome this anticipated problem.

4.5 Summary

In this chapter, the nature and properties of the highly resistive state obtained by back-gating 2DEGs via first positive polarization (FPP) pulse have been investigated. It is shown that, also according to the initial sheet carrier density, the samples can be brought into a persistent insulating state after a positive polarization pulse. This persistent state, under many aspects, is analogous to the floating-gate MOSFET devices. In low carrier-density samples, a non-volatile four-order-of-magnitude resistive switching to the insulating state is obtained. The metastable insulating state induced in the samples is characterized by an extreme light sensitivity, so that a four-order-of-magnitude switch back to the pristine metallic state is obtained thought a modest dose of red photons. Furthermore the possibility of multilevel switching and its stability on the scale of hours is also demonstrated.

Chapter 5

An Investigation of the Intrinsic Limitation of Low Temperature Mobility

Abstract

Chapter 5 investigates the origin and nature of the defects state and evaluates its effect on the mobility of the system. This evaluation is performed by comparing the residual resistive ratio with the sheet carrier density at room temperature. The scaling of the residual resistive ratio with the sheet carrier density after the external perturbation, i.e. by light or by electric field is also discussed.

5.1 Residual Resistive Ratio vs. Sheet Carrier Density

This study was performed to understand the origin and nature of carrier numbers whether they are coming from donor defect states in the material, or if they are provided by other mechanisms. The correlation between the number of carriers and defect states strongly takes into account the presence of oxygen vacancies while the absence of correlation can be associated with the mechanism such as the electronic reconstruction which is insensitive to the presence of defects (see section 1.6 in chapter 1).

The contribution of the defects donor to the transport properties of the investigated samples is evaluated by comparing the residual resistive ratio (RRR) with the sheet carrier density (n) at room temperature. The RRR was assessed by the ratio between the resistance of the samples at 290 K and 10 K (the lowest temperature that can be achieved in the measurements) i.e. $R_{290\ K}$ /$R_{10\ K}$. The RRR may vary substantially for a material depending on the amount of impurities. It serves as a rough index of the purity and overall quality of a sample. Since resistivity usually

increases as defect prevalence increases, a large RRR is associated with a pure sample. The RRR is basically the reflection of mobility of the samples [107].

For the RRR, R_{sheet}-T measurements for a number of samples including crystalline and amorphous $LaAlO_3/SrTiO_3$, γ-$Al_2O_3/SrTiO_3$ and $LaGaO_3/SrTiO_3$ have been performed. As an example, Figure 5.1 shows the plot of R_{sheet}-T curves for two γ-$Al_2O_3/SrTiO_3$ samples exhibiting RRR 187 and 78. For each sample the carrier density at room temperature was also determined by Hall Effect. In order to investigate the scaling of RRR with carrier number over a wide range, a number of samples were fabricated under a variety of conditions of growth pressure, temperature and thickness. Transport parameters for some of the simples showing different RRR and n are reported in Table 5.1, while the full summary of these results for RRR vs. n is depicted in Figure 5.2. The data shows a general trend that RRR increase with decrease in n.

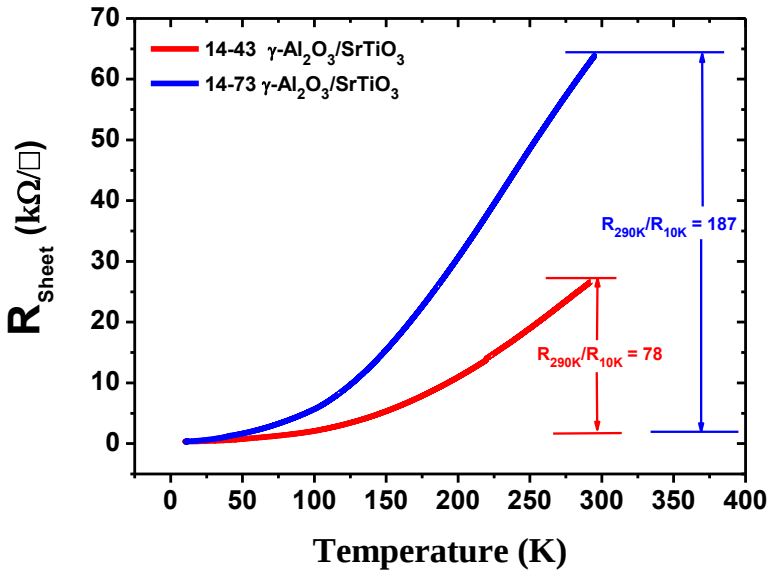

Figure 5.1 R_{sheet}-T curves for γ-$Al_2O_3/SrTiO_3$ samples fabricated under different grown conditions, residual resistive ratios (RRR = $R_{290\ K}$ /$R_{10\ K}$) are indicated, 14-43 and 14-73 are sample numbers.

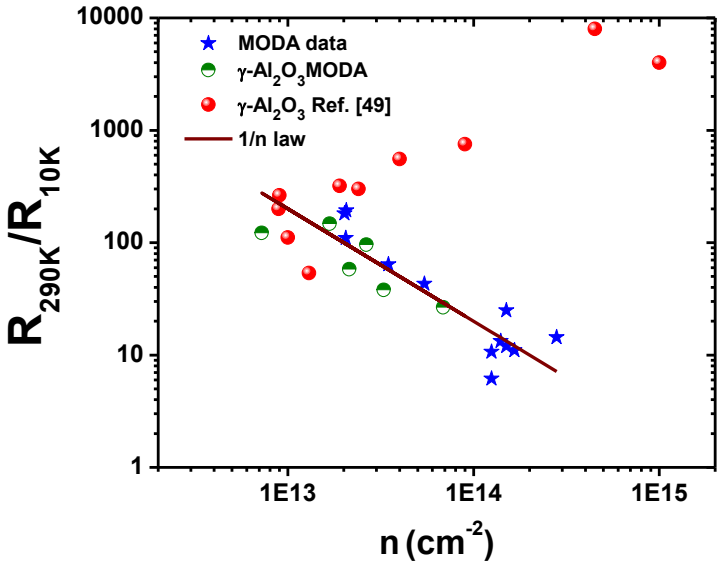

Figure 5.2 Residual resistive ratio vs. sheet carrier density for different (MODA) samples (samples fabricated for the present study) exhibits 1/n law trend, for comparison, γ-Al_2O_3/$SrTiO_3$ samples from Ref [49] shows deviation from the trend.

Table 5.1: Transport properties of some of the samples used in the study RRR and n.

System	$(R_{sheet})_{290K}$ (kΩ)	$(R_{sheet})_{10K}$ (kΩ)	*RRR*	*n* (cm^{-2})
c-$LaAlO_3$/$SrTiO_3$	2.04	0.47	43	5.4×10^{13}
c-$LaGaO_3$/$SrTiO_3$	5.80	5.2	11	1.6×10^{14}
a-$LaGaO_3$/$SrTiO_3$	67.8	0.37	182	2.0×10^{13}
γ-Al_2O_3/$SrTiO_3$	41.2	0.42	96	2.6×10^{13}
$NdGaO_3$/$SrTiO_3$	303	9.5	31	6.0×10^{13}

To explain this trend, here a simple model based on Drude formula i.e. $\sigma = ne\mu$ is presented. The model basically takes into account the electron mobility dependence on temperature. At room temperature the mobility is limited by the phonon scattering, yielding $\mu \propto T^{-2}$. At low temperature the scattering from impurities becomes dominant, so that assuming that the scattering rule holds, we have $\mu^{-1} = An_i + BT^2$, where A, B are constants, and n_i is the number of impurity centers that contributes to the scattering. Hence the resistive ratio reads:

$$\frac{R_{290K}}{R_{10K}} = \left[\frac{BT_{290K}^{\ 2}}{A} \left(\frac{n_{10K}}{n_i} \right) \right] \times \frac{1}{n_{290K}}$$

where n_{10K} and n_{290K}, respectively, are the sheet carrier density at 10 and 290 K.

If the ansatz $n_{10K} \approx n_i$ is made we immediately get $R_{290K}/R_{10K} \propto 1/n_{290K}$ according to the experimental evidence. The explanation of the ansatz is based on the hypothesis that each charge carrier is originated from a defect, and that furthermore, each ionized donor also behaves as a scattering center. Note that this assumption does not require that the donor sites are inside the quantum well. In fact, ionized donor that are located in the vicinity of the well equally contribute to the scattering process due to the screened columbic potential, that extends its range over several unit cells length.

Note that the high mobility γ-$Al_2O_3/SrTiO_3$ samples from Ref. [49] do not follow the scaling rule $R_{290K}/R_{10K} \propto n^{-1}$. However, this appears as quite a unique exception, because the generality of data from literature fit the described scenario. However, different physical explanations have been provided.

Y. Xie et al. [108] tuned the carriers at the $LaAlO_3/SrTiO_3$ interface using surface treatments induced by conducting atomic force microscopy, solvent, and heating. The authors demonstrated that mobility varies inversely to n in a universal manner both for as-grown samples as well as for the samples in which the carrier density is tuned by different techniques. They propose that this is the result of the scaling of the quantum well width with n. In this model, for low n, the width

of well is large, the carriers suffers from less scattering, thereby leading to high mobility. The reverse would hold for high n.

In order to compare the two differ interpretations a special experiment was devised, in which the sheet carrier density n and the RRR of samples perturbed by the light and field effect were evaluated.

Figure 5.3 (a,b) compares the $R_{sheet}(T)$ for the virgin and, blue light and field effect perturbed samples. The field effect measurements at low temperature persistently change the resistance of the samples (see section 4.1 in chapter 4). At room temperature this change is still evident. This allows to find new RRR with respect to virgin $R_{sheet}(T)$ (Figure 5.3 b). In the perturbed state after light or field effect, the new carrier densities were determined by the following method.

A small signal of the gate bias (30 V) across 0.5 mm thick substrate was applied only to change the carrier density and presumably not the mobility. The mobility was calculated from the slop of $\Delta\sigma$ vs. Δn plot, i.e. $\mu = \Delta\sigma/\Delta n$ (Figure 5.4) (see section 3.6 in chapter 3 for further details). The calculated mobility was used to find the total sheet density after perturbation by light or electric field by the following formula:

$$n = \Delta\sigma/e.\mu$$

The sheet carrier density and mobility measured using this method shows very good agreement with the data obtained by Hall Effect. The data for $R_{290\ K}/R_{10\ K}$ vs. n are reported in Figure 5.5 (a,b).

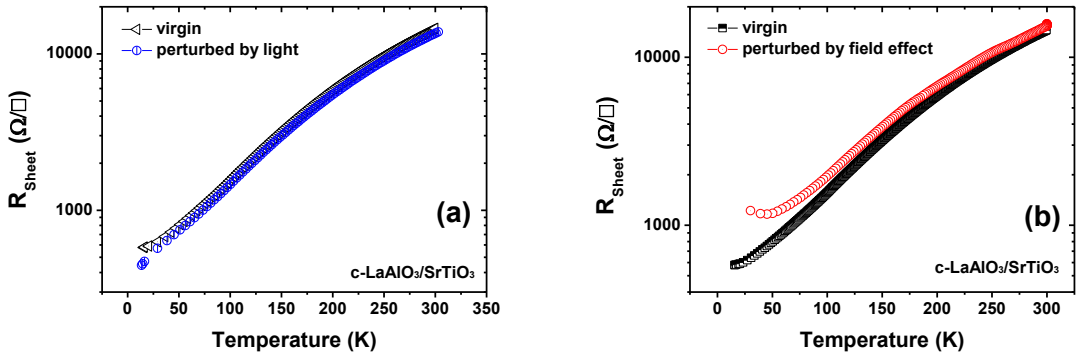

Figure 5.3 Comparison of R_{sheet}-T virgin curves after perturbation by (a) light and (b) electric field effect.

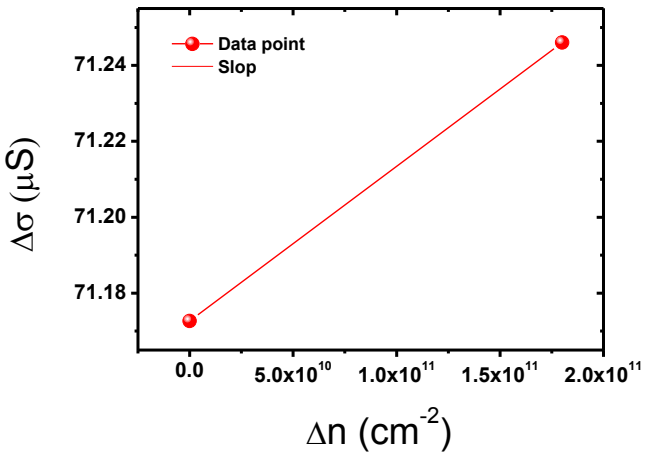

Figure 5.4 Sheet conductivity change for c-$LaAlO_3$/$SrTiO_3$ as a function of field induced sheet carrier density at 300 K. The mobility is calculated from the slop.

The claim in Ref [108] was that in whatever way the carrier numbers is changed, the scaling law $\mu \propto 1/n$ holds. Instead, our data show that this is not the case when the perturbation is provided by light or field effect. This strongly underscores the universal mechanism provided by those authors.

On the contrary, the data of the Figure 5.5 (b) support the idea that the scaling law is just due to the identification of scattering centers and donors. In fact, the external perturbation by light or by field breaks this identity by providing/subtracting carrier without creating further scattering centers. As a result, the highest mobility pertains to the highest sheet carrier density, that is the opposite of the scaling law.

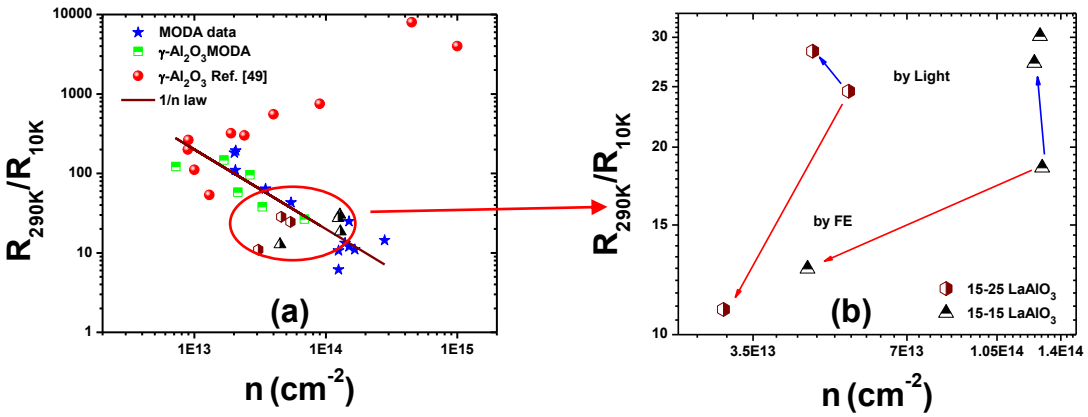

Figure 5.5 (a) $R_{290\ K}/R_{10\ K}$ Vs. n plot, the circle emphases samples subjected to external perturbations (b) zoom in of (a) indicating the movement of data points probed by light and field effect (FE).

5.2 Summary

In summary, in this chapter the residual resistive ratio and the sheet carrier density at room temperature were compared. We showed that for as-grown samples, the residual resistive ratio follows the inverse proportionality law with sheet carrier density. This law is explained by assuming that each charge carrier is originated from a defect that also acts as a scattering center. The data showed that the scaling law breaks when the perturbation is provided by light or field effect. This evidence is also explained by the model, when considering that the extra carriers in these cases are not provided by local defects.

Summary of Results

In this thesis the electric transport properties of two-dimensional electron gases (2DEGs) formed at oxide heterostructures were probed under two external perturbations, i.e. light and electric field. The heterostructures investigated in this study include crystalline and amorphous $LaAlO_3/SrTiO_3$, γ-$Al_2O_3/SrTiO_3$ and $LaGaO_3/SrTiO_3$.

The photoresponse of different samples under light illumination with wavelength in the range 365-625 nm and at variable intensities was investigated. A double-exponential function with a fast and a slow component was used to fit the long photoresponse transient. The full photoresponse ($\sigma_\infty/\sigma_o I$), representing the quantum photogeneration efficiency, was found to increase exponentially as a function of photon energy for all samples. The fast and slow components of the full photoresponse also showed an exponential growth with energy. It was further found that the fast component shows very similar overall behavior in all samples, while the slow component has a large spread. This suggests that the fast component depends on intrinsic properties of the interfaces, while the slow component may be mainly due to defects. A model based on the energy band diagrams of crystalline and amorphous structures was presented to interpret the results.

The dependence of the 2DEG resistance upon the gate voltage is non-trivial. In particular, the sheet resistance vs. gate voltage plots of data collected at low temperature show a hysteretic behavior and demonstrate the peculiar phenomenon of first positive polarization. Furthermore, the hysteresis plots allow one to determine the mobility of the 2DEG. By this tool it was possible to demonstrate that at least two bands with different mobility concur to the electrical transport at the interface.

By studying the combined effect of electric field and light at room temperature, it was found that the response to the gate modulation can be enhanced by the light depending on photons energy. Interestingly, the samples showed no variation in resistance to the gate modulation in the

presence of UV photons (3.4 eV). A similar experiment was performed on amorphous samples resulting in the same light-improved gating effects at low photon energies. This finding suggests a universal nature of this phenomenon.

The low temperature field effect measurements showed that the virgin state of the samples is persistently changed after the first positive gate polarization. In this regard, the effect on three samples with different initial sheet carrier density was discussed. It was shown that, also according to the initial sheet carrier density, the samples can be brought by a positive polarization pulse into a persistent insulating state. Such phenomenon is due to the formation of a "retention state" that is similar, under many aspects, to the analogous state obtained in floating-gate MOSFET devices.

In low sheet carrier-density samples, a non-volatile four-order-of-magnitude resistive switching to the insulating state was obtained. We argue that the obtained electrostatic configuration mimicks the charging of the floating gate in a MOSFET-type device. The floating gate states are given, in our oxide interfaces, by trap states that are present in the $SrTiO_3$ bulk. The recovery of the pristine metallic state can be either obtained by a long room-temperature field annealing, or, instantaneously, by a relatively modest dose of visible-range photons. Illumination caused in fact a sudden collapse of the electron system back to the metallic ground state, with a resistivity drop exceeding four orders of magnitude.

The possibility to stabilize intermediate resistance states, to be employed for the implementation of a multilevel, optically controlled, resistive memory system was also investigated. It was found that intermediate resistive states can be accessed by employing lower gate voltages and light pulses for shorter duration. If the system is left unperturbed after first positive polarization, i.e. under zero gate bias and in dark condition, the high resistive state is sustained for hours.

The scaling of the residual resistive ratio, which represents the mobility of the system, was investigated against the sheet carrier density at room temperature. For the as-grown samples, the sheet carrier density varied inversely to the residual resistive ratio. Instead, when the carrier numbers are changed by light or by electric field, the inverse law breaks. In such a case, we conclude that the carriers are added/subtracted from the system without creating further scattering centers.

References

[1] Ohtomo A, Hwang H. A high-mobility electron gas at the LaAlO3/SrTiO3 heterointerface. Nature. 2004;427:423-6.

[2] Tebano A, Fabbri E, Pergolesi D, Balestrino G, Traversa E. Room-temperature giant persistent photoconductivity in SrTiO3/LaAlO3 heterostructures. ACS nano. 2012;6:1278-83.

[3] Biscaras J, Hurand S, Feuillet-Palma C, Rastogi A, Budhani R, Reyren N, et al. Limit of the electrostatic doping in two-dimensional electron gases of LaXO3 (X= Al, Ti)/SrTiO3. Scientific reports. 2014;4.

[4] Thiel S, Hammerl G, Schmehl A, Schneider C, Mannhart J. Tunable quasi-two-dimensional electron gases in oxide heterostructures. Science. 2006;313:1942-5.

[5] Davies JH. The physics of low-dimensional semiconductors: an introduction: Cambridge university press; 1997.

[6] Bastard G. Wave mechanics applied to semiconductors. Les editions de Physique CNRS, Paris. 1988.

[7] Beenakker C, van Houten H. Quantum transport in semiconductor nanostructures. Solid state physics. 1991;44:228.

[8] Ando T, Matsumoto Y, Uemura Y. Theory of Hall effect in a two-dimensional electron system. Journal of the Physical Society of Japan. 1975;39:279-88.

[9] Faist J, Capasso F, Sivco DL, Sirtori C, Hutchinson AL, Cho AY. Quantum cascade laser. Science. 1994;264:553-6.

[10] Morosan E, Natelson D, Nevidomskyy AH, Si Q. Strongly correlated materials. Advanced Materials. 2012;24:4896-923.

[11] Antonov V, Bekenov L, Yaresko A. Electronic structure of strongly correlated systems. Advances in Condensed Matter Physics. 2011;2011.

[12] Pergament A, Stefanovich G, Velichko A. Oxide electronics and vanadium dioxide perspective: a review. Journal on Selected Topics in Nano Electronics and Computing. 2013;1:24-43.

[13] Maekawa S, Tohyama T, Barnes SE, Ishihara S, Koshibae W, Khaliullin G. Physics of transition metal oxides: Springer Science & Business Media; 2013.

[14] Zubko P, Gariglio S, Gabay M, Ghosez P, Triscone J-M. Interface physics in complex oxide heterostructures. Annu Rev Condens Matter Phys. 2011;2:141-65.

[15] Schlom DG, Chen LQ, Pan X, Schmehl A, Zurbuchen MA. A thin film approach to engineering functionality into oxides. Journal of the American Ceramic Society. 2008;91:2429-54.

[16] Chaudhari P, Koch R, Laibowitz R, McGuire T, Gambino R. Critical-current measurements in epitaxial films of YBa 2 Cu 3 O 7− x compound. Physical review letters. 1987;58:2684.

[17] Kawasaki M, Takahashi K, Maeda T, Tsuchiya R. Atomic control of the SrTiO (3) crystal surface. Science. 1994;266:1540.

[18] Koster G, Rijnders G, Blank DH, Rogalla H. Surface morphology determined by (001) single-crystal SrTiO 3 termination. Physica C: Superconductivity. 2000;339:215-30.

[19] Müller K, Berlinger W, Waldner F. Characteristic structural phase transition in perovskite-type compounds. Physical review letters. 1968;21:814.

[20] Jaffe HW. Introduction to Crystal Chemistry: Student Edition: CUP Archive; 1988.

[21] Salluzzo M, Cezar J, Brookes N, Bisogni V, De Luca G, Richter C, et al. Orbital reconstruction and the two-dimensional electron gas at the LaAlO 3/SrTiO 3 interface. Physical review letters. 2009;102:166804.

[22] Cardona M. Optical Properties and Band Structure of SrTi O 3 and BaTi O 3. Physical Review. 1965;140:A651.

[23] Van Benthem K, Elsässer C, French R. Bulk electronic structure of SrTiO3: Experiment and theory. Journal of Applied Physics. 2001;90:6156-64.

[24] Cooper VR, Seo SSA, Lee S, Kim JS, Choi WS, Okamoto S, et al. Transparent conducting oxides: A d-doped superlattice approach. Nature materials. 2014;4.

[25] Fleury P, Worlock J. Electric-Field-Induced Raman Scattering in SrTi O 3 and KTa O 3. Physical Review. 1968;174:613.

[26] Vogt H. Refined treatment of the model of linearly coupled anharmonic oscillators and its application to the temperature dependence of the zone-center soft-mode frequencies of KTaO 3 and SrTiO 3. Physical Review B. 1995;51:8046.

[27] Müller KA, Burkard H. SrTi O 3: An intrinsic quantum paraelectric below 4 K. Physical Review B. 1979;19:3593.

[28] Hirose S, Okushi H, Ueda S, Yoshikawa H, Adachi Y, Ando A, et al. Electric field and temperature dependence of dielectric permittivity in strontium titanate investigated by a photoemission study on Pt/SrTiO3: Nb junctions. Applied Physics Letters. 2015;106:191602.

[29] Viana R, Lunkenheimer P, Hemberger J, Böhmer R, Loidl A. Dielectric spectroscopy in SrTiO 3. Physical Review B. 1994;50:601.

[30] Bednorz J, Müller K. Sr 1− x Ca x Ti O 3: An XY Quantum Ferroelectric with Transition to Randomness. Physical review letters. 1984;52:2289.

[31] Haeni J, Irvin P, Chang W, Uecker R, Reiche P, Li Y, et al. Room-temperature ferroelectricity in strained SrTiO3. Nature. 2004;430:758-61.

[32] Fuchs D, Schneider C, Schneider R, Rietschel H. High dielectric constant and tunability of epitaxial SrTiO3 thin film capacitors. Journal of Applied Physics. 1999;85:7362-9.

[33] Schooley J, Hosler W, Cohen ML. Superconductivity in Semiconducting SrTi O 3. Physical review letters. 1964;12:474.

[34] Ueno K, Nakamura S, Shimotani H, Ohtomo A, Kimura N, Nojima T, et al. Electric-field-induced superconductivity in an insulator. Nature materials. 2008;7:855-8.

[35] Fix T, Bali R, Stelmashenko N, Blamire M. Influence of the dopant concentration in In-doped SrTiO 3 on the structural and transport properties. Solid State Communications. 2008;146:428-30.

[36] Lee C, Destry J, Brebner J. Optical absorption and transport in semiconducting SrTi O 3. Physical Review B. 1975;11:2299.

[37] Kleemann W, Dec J, Wang Y, Lehnen P, Prosandeev S. Phase transitions and relaxor properties of doped quantum paraelectrics. Journal of Physics and Chemistry of Solids. 2000;61:167-76.

[38] Herranz G, Basletić M, Bibes M, Carrétéro C, Tafra E, Jacquet E, et al. High mobility in LaAlO 3/SrTiO 3 heterostructures: origin, dimensionality, and perspectives. Physical review letters. 2007;98:216803.

[39] Kan D, Terashima T, Kanda R, Masuno A, Tanaka K, Chu S, et al. Blue-light emission at room temperature from Ar+-irradiated SrTiO3. Nature materials. 2005;4:816-9.

[40] Janotti A, Varley JB, Choi M, Van de Walle CG. Vacancies and small polarons in SrTiO 3. Physical Review B. 2014;90:085202.

[41] Frederikse H, Thurber W, Hosler W. Electronic transport in strontium titanate. Physical Review. 1964;134:A442.

[42] Tufte O, Chapman P. Electron mobility in semiconducting strontium titanate. Physical Review. 1967;155:796.

[43] Santander-Syro A, Copie O, Kondo T, Fortuna F, Pailhes S, Weht R, et al. Two-dimensional electron gas with universal subbands at the surface of SrTiO3. Nature. 2011;469:189-93.

[44] Di Capua R, Radovic M, De Luca G, Maggio-Aprile I, Granozio FM, Plumb N, et al. Observation of a two-dimensional electron gas at the surface of annealed SrTiO 3 single crystals by scanning tunneling spectroscopy. Physical Review B. 2012;86:155425.

[45] Pentcheva R, Huijben M, Otte K, Pickett WE, Kleibeuker JE, Huijben J, et al. Parallel electron-hole bilayer conductivity from electronic interface reconstruction. Physical review letters. 2010;104:166804.

[46] Annadi A, Zhang Q, Wang XR, Tuzla N, Gopinadhan K, Lü W, et al. Anisotropic two-dimensional electron gas at the LaAlO3/SrTiO3 (110) interface. Nature communications. 2013;4:1838.

[47] Chen Y, Pryds N, Kleibeuker JE, Koster G, Sun J, Stamate E, et al. Metallic and insulating interfaces of amorphous SrTiO3-based oxide heterostructures. Nano letters. 2011;11:3774-8.

[48] Di Gennaro E, di Uccio US, Aruta C, Cantoni C, Gadaleta A, Lupini AR, et al. Persistent photoconductivity in 2d electron gases at different oxide interfaces. Advanced Optical Materials. 2013;1:834-43.

[49] Chen Y, Bovet N, Trier F, Christensen D, Qu F, Andersen NH, et al. A high-mobility two-dimensional electron gas at the spinel/perovskite interface of γ-Al2O3/SrTiO3. Nature communications. 2013;4:1371.

[50] Ealet B, Elyakhloufi M, Gillet E, Ricci M. Electronic and crystallographic structure of γ-alumina thin films. Thin Solid Films. 1994;250:92-100.

[51] Caviglia A, Gariglio S, Reyren N, Jaccard D, Schneider T, Gabay M, et al. Electric field control of the LaAlO3/SrTiO3 interface ground state. Nature. 2008;456:624-7.

[52] Brinkman A, Huijben M, Van Zalk M, Huijben J, Zeitler U, Maan J, et al. Magnetic effects at the interface between non-magnetic oxides. Nature materials. 2007;6:493-6.

[53] Huijben M, Brinkman A, Koster G, Rijnders G, Hilgenkamp H, Blank DH. Structure–property relation of SrTiO3/LaAlO3 interfaces. Advanced Materials. 2009;21:1665-77.

[54] De Luca G, Rubano A, di Gennaro E, Khare A, Granozio FM, di Uccio US, et al. Potential-well depth at amorphous-LaAlO3/crystalline-SrTiO3 interfaces measured by optical second harmonic generation. Applied Physics Letters. 2014;104:261603.

[55] Banerjee S, Erten O, Randeria M. Ferromagnetic exchange, spin-orbit coupling and spiral magnetism at the LaAlO3/SrTiO3 interface. Nature physics. 2013;9:626-30.

[56] Berner G, Glawion S, Walde J, Pfaff F, Hollmark H, Duda L-C, et al. LaAlO 3/SrTiO 3 oxide heterostructures studied by resonant inelastic x-ray scattering. Physical Review B. 2010;82:241405.

[57] Nakagawa N, Hwang HY, Muller DA. Why some interfaces cannot be sharp. Nature materials. 2006;5:204-9.

[58] Huijben M, Rijnders G, Blank DH, Bals S, Van Aert S, Verbeeck J, et al. Electronically coupled complementary interfaces between perovskite band insulators. Nature materials. 2006;5:556-60.

[59] Chen Y, Trier F, Wijnands T, Green R, Gauquelin N, Egoavil R, et al. Extreme mobility enhancement of two-dimensional electron gases at oxide interfaces by charge-transfer-induced modulation doping. Nature materials. 2015;14:801-6.

[60] Liu Z, Li C, Lü W, Huang X, Huang Z, Zeng S, et al. Origin of the two-dimensional electron gas at LaAlO 3/SrTiO 3 interfaces: the role of oxygen vacancies and electronic reconstruction. Physical Review X. 2013;3:021010.

[61] Huijben M, Koster G, Kruize MK, Wenderich S, Verbeeck J, Bals S, et al. Defect engineering in oxide heterostructures by enhanced oxygen surface exchange. Advanced Functional Materials. 2013;23:5240-8.

[62] Siemons W, Koster G, Yamamoto H, Geballe TH, Blank DH, Beasley MR. Experimental investigation of electronic properties of buried heterointerfaces of La Al O 3 on Sr Ti O 3. Physical Review B. 2007;76:155111.

[63] Hüfner S. Photoelectron spectroscopy: principles and applications: Springer Science & Business Media; 2013.

[64] Di Gennaro E, Coscia U, Ambrosone G, Khare A, Granozio FM, di Uccio US. Photoresponse dynamics in amorphous-LaAlO3/SrTiO3 interfaces. Scientific reports. 2015;5.

[65] Chen H, Kolpak AM, Ismail-Beigi S. Electronic and magnetic properties of SrTiO3/LaAlO3 interfaces from first principles. Advanced Materials. 2010;22:2881-99.

[66] Popović ZS, Satpathy S, Martin RM. Origin of the two-dimensional electron gas carrier density at the LaAlO 3 on SrTiO 3 interface. Physical review letters. 2008;101:256801.

[67] Sing M, Berner G, Goß K, Müller A, Ruff A, Wetscherek A, et al. Profiling the interface electron gas of LaAlO 3/SrTiO 3 heterostructures with hard X-ray photoelectron spectroscopy. Physical review letters. 2009;102:176805.

[68] Siemons W, Koster G, Yamamoto H, Harrison WA, Lucovsky G, Geballe TH, et al. Origin of charge density at LaAlO 3 on SrTiO 3 heterointerfaces: possibility of intrinsic doping. Physical review letters. 2007;98:196802.

[69] Kalabukhov A, Gunnarsson R, Börjesson J, Olsson E, Claeson T, Winkler D. Effect of oxygen vacancies in the SrTiO 3 substrate on the electrical properties of the LaAlO 3⁄ SrTiO 3 interface. Physical Review B. 2007;75:121404.

[70] Maurice J-L, Devos I, Casanove M-J, Carrétéro C, Gachet G, Herranz G, et al. Charge imbalance at oxide interfaces: How nature deals with it. Materials Science and Engineering: B. 2007;144:1-6.

[71] Basletic M, Maurice J-L, Carrétéro C, Herranz G, Copie O, Bibes M, et al. Mapping the spatial distribution of charge carriers in LaAlO3/SrTiO3 heterostructures. Nature materials. 2008;7:621-5.

[72] van Heeringen L, de Wijs G, McCollam A, Maan J, Fasolino A. k· p subband structure of the LaAlO 3/SrTiO 3 interface. Physical Review B. 2013;88:205140.

[73] Ihn T. Semiconductor nanostructures. Quantum states and electronic transport (OUP Oxford,□□□□). 2010.

[74] Sze S, Ng KK. Physics of semiconductor devices 3rd Edition. Wiley Online Library; 2007.

[75] Yu PY, Cardona M. Fundamentals of semiconductors: Springer; 2005.

[76] Blase X, Bustarret E, Chapelier C, Klein T, Marcenat C. Superconducting group-IV semiconductors. Nature materials. 2009;8:375-82.

[77] Goldman AM, Markovic N. Superconductor-insulator transitions in the two-dimensional limit. Physics Today. 1998;51:39-44.

[78] Tokura Y. Photoinduced phase transition: A tool for generating a hidden state of matter. Journal of the Physical Society of Japan. 2006;75:011001.

[79] Irvin P, Ma Y, Bogorin DF, Cen C, Bark CW, Folkman CM, et al. Rewritable nanoscale oxide photodetector. Nature Photonics. 2010;4:849-52.

[80] Chan NY, Zhao M, Wang N, Au K, Wang J, Chan LWH, et al. Palladium nanoparticle enhanced giant photoresponse at LaAlO3/SrTiO3 two-dimensional electron gas heterostructures. ACS nano. 2013;7:8673-9.

[81] Lu H-L, Liao Z-M, Zhang L, Yuan W-T, Wang Y, Ma X-M, et al. Reversible insulator-metal transition of LaAlO3/SrTiO3 interface for nonvolatile memory. Scientific reports. 2013;3.

[82] Caviglia A, Gabay M, Gariglio S, Reyren N, Cancellieri C, Triscone J-M. Tunable Rashba spin-orbit interaction at oxide interfaces. Physical review letters. 2010;104:126803.

[83] Hosoda M, Hikita Y, Hwang HY, Bell C. Transistor operation and mobility enhancement in top-gated LaAlO 3/SrTiO 3 heterostructures. Applied Physics Letters. 2013;103:103507.

[84] Bell C, Harashima S, Kozuka Y, Kim M, Kim B, Hikita Y, et al. Dominant mobility modulation by the electric field effect at the LaAlO 3/SrTiO 3 interface. Physical review letters. 2009;103:226802.

[85] Lei Y, Li Y, Chen Y, Xie Y, Chen Y, Wang S, et al. Visible-light-enhanced gating effect at the LaAlO3/SrTiO3 interface. Nature communications. 2014;5.

[86] Sambri A. Pulsed laser deposition of complex transition metal oxides: plume expansion and film growth: Università degli Studi di Napoli Federico II; 2008.

[87] Riaz M. Transport Properties of Transition Metal Oxide Thin Films and Interfaces under Light Irradiation. 2011.

[88] Geohegan DB. Physics and diagnostics of laser ablation plume propagation for high-T c superconductor film growth. Thin Solid Films. 1992;220:138-45.

[89] Kools J, Baller T, De Zwart S, Dieleman J. Gas flow dynamics in laser ablation deposition. Journal of Applied Physics. 1992;71:4547-56.

[90] Wicklein S. Defect Engineering of SrTiO3 thin films for resistive switching applications: Christian-Albrechts Universität Kiel; 2013.

[91] van der PAUYV L. A method of measuring specific resistivity and Hall effect of discs of arbitrary shape. Philips Res Rep. 1958;13:1-9.

[92] Hall EH. On a new action of the magnet on electric currents. American Journal of Mathematics. 1879;2:287-92.

[93] Banerjee N, Huijben M, Koster G, Rijnders G. Direct patterning of functional interfaces in oxide heterostructures. Applied Physics Letters. 2012;100:041601.

[94] 酸化物ヘテロ構造における低次元電子物性. Low-Dimensional Electronic Properties of Oxide Heterostructures: The University of Tokyo; 2010.

[95] Rastogi A, Budhani R. Solar blind photoconductivity in three-terminal devices of LaAlO 3/SrTiO 3 heterostructures. Optics letters. 2012;37:317-9.

[96] Treske U, Heming N, Knupfer M, Büchner B, Di Gennaro E, Khare A, et al. Universal electronic structure of polar oxide hetero-interfaces. Scientific reports. 2015;5.

[97] Verma A, Raghavan S, Stemmer S, Jena D. Au-gated SrTiO3 field-effect transistors with large electron concentration and current modulation. Applied Physics Letters. 2014;105:113512.

[98] Thiel SP. Study of interface properties in LaAlO3/SrTiO3 heterostructures. Doctoral, der mathematisch-naturwissenschaftlichen Fakultat, der Universitat Augsburg. 2009.

[99] Christensen D, Trier F, Chen Y, Smith A, Nygård J, Pryds N. Controlling interfacial states in amorphous/crystalline LaAlO3/SrTiO3 heterostructures by electric fields. Applied Physics Letters. 2013;102:021602.

[100] Leisegang T, Stöcker H, Levin A, Weißbach T, Zschornak M, Gutmann E, et al. Switching Ti valence in SrTiO 3 by a dc electric field. Physical review letters. 2009;102:087601.

[101] Tian H, Zhao Y, Jiang X, Shi J, Zhang H, Sun J. Resistance switching effect in LaAlO3/Nb-doped SrTiO3 heterostructure. Applied Physics A. 2011;102:939-42.

[102] Delugas P, Filippetti A, Fiorentini V, Bilc DI, Fontaine D, Ghosez P. Spontaneous 2-dimensional carrier confinement at the n-type SrTiO 3/LaAlO 3 interface. Physical review letters. 2011;106:166807.

[103] Hasler P, Lande TS. Overview of floating-gate devices, circuits, and systems. Circuits and Systems II: Analog and Digital Signal Processing, IEEE Transactions on. 2001;48:1-3.

[104] Makwana JJ, Schroder DDK. A nonvolatile memory overview. 2004.

[105] Seri S, Schultz M, Klein L. Thermally activated recovery of electrical conductivity in LaAlO 3/SrTiO 3. Physical Review B. 2013;87:125110.

[106] Yang Z, Ko C, Ramanathan S. Oxide electronics utilizing ultrafast metal-insulator transitions. Annual Review of Materials Research. 2011;41:337-67.

[107] Wesche R. High-temperature superconductors: materials, properties, and applications: Springer Science & Business Media; 2013.

[108] Xie Y, Bell C, Hikita Y, Harashima S, Hwang HY. Enhancing electron mobility at the LaAlO3/SrTiO3 interface by surface control. Advanced Materials. 2013;25:4735-8.